RICE UNIVERSITY

Structural Sorting and Oxygen Doping of Semiconducting Single-Walled Carbon Nanotubes

by

Saunab Ghosh

A THESIS SUBMITTED
IN PARTIAL FULFILLMENT OF THE
REQUIREMENTS FOR THE DEGREE

Doctor of Philosophy

APPROVED, THESIS COMMITTEE:

R. Bruce Weisman

R. Bruce Weisman, Chair,
Professor of Chemistry

Jason H. Hafner,
Associate Professor of Physics and Astronomy
Associate Professor of Chemistry

Robert H. Hauge,
Distinguished Faculty Fellow in Chemistry

HOUSTON, TEXAS

September 2011

ABSTRACT

Structural Sorting and Oxygen Doping of Semiconducting Single-walled Carbon Nanotubes

by

Saunab Ghosh

Existing growth methods produce single-walled carbon nanotubes (SWCNTs) with a range of structures and electronic properties, but many potential applications require pure nanotube samples. Density gradient ultracentrifugation (DGU) has recently emerged as a technique for sorting as-grown mixtures of single-walled nanotubes into their distinct (*n*,*m*) structural forms, but this approach has been limited to samples containing only a small number of nanotube structures, and has often required repeated DGU processing. For the first time, it has been shown that the use of tailored nonlinear density gradient ultracentrifugation (NDGU) can significantly improve DGU separations. This new sorting process readily separated highly polydisperse samples of SWCNTs grown by the HiPco method in a single step to give fractions enriched in any of ten different (*n*,*m*) species. In addition, minor variants of the method allowed separation of the mirror-image isomers (enantiomers) of seven (*n*,*m*) species. Optimization of this new approach was aided by the development of instrumentation that spectroscopically mapped nanotube contents inside undisturbed centrifuge tubes. Besides, sorted nanotube samples enabled the discovery of novel oxygen-doped SWCNTs with remarkable photophysical properties. Modified nanotube samples were produced using mild oxidation of SWCNTs with ozone followed by a photochemical conversion step that induced well-defined

changes in emissive properties. As demonstrated for a set of ten separated SWCNT (*n,m*) structures, chemically altered nanotubes possess slightly lower band gap energies with correspondingly longer photoluminescence wavelengths. Treated samples showed distinct, structure-specific near-infrared fluorescence at wavelengths 10 to 15% longer than the pristine semiconducting SWCNTs. Quantum chemical modeling suggests that dopant sites harvest light energy absorbed in undoped nanotube regions by trapping mobile excitons. The oxygen-doped SWCNTs are much easier to detect and image in biological specimen than pristine SWCNTs because they give stronger near-IR emission and do not absorb at the shifted emission wavelength. This novel modification of SWCNT properties may lead to new optical and electronic applications, as it provides a way to change optical band gaps in whole nanotubes or in selected sections.

ACKNOWLEDGEMENTS

There are many people that I would like to thank for their help and support during my studies at Rice University leading to this thesis. First of all, I wish to express my highest gratitude to my graduate research advisor Professor R. Bruce Weisman. I greatly appreciate his support and guidance given to me throughout my studies at Rice. His compassion and kindness make me realize how lucky I am to have him as my advisor. Besides, I am highly grateful to our favorite research scientist Dr. Sergei M. Bachilo for his immense contribution toward my overall research progress including performing the quantum chemical calculations. I am also deeply indebted to my parents for their patience and continual supports through the years. In addition, I wish to thank Professor Kathleen M. Beckingham and her research group, specifically Mrs. Rebecca A. Simonette, for preparing biological specimens with O-doped SWCNTs. I would like to thank all faculties of the department of Chemistry, Rice University, and the funding organizations for financial support. My special appreciations are extended to all of my friends, and Weisman lab group members for providing me with endless motivations.

This thesis is dedicated to my research advisor Professor R. Bruce Weisman and Dr. Sergei M. Bachilo, without whom this work would have been impossible to accomplish.

TABLE OF CONTENTS

LIST OF FIGURES

LIST OF TABLES

CHAPTER 1

INTRODUCTION

The study of single-walled carbon nanotubes (SWCNTs) began from its initial discovery in 1991 by Iijima *et al.*[1] For twenty years, researchers have focused on studying their unique electrical, mechanical, thermal, and optical properties.[2-7] SWCNTs are thermodynamically stable hollow cylinders of covalently-bonded carbon atoms with diameters on the order of nanometers and lengths ranging from tens of nanometers to centimeters. Their extremely high aspect ratios with one atom wall thickness give SWCNT remarkable quasi-one dimensional properties.[3] High aspect ratios also suggest the need for multidisciplinary approaches in SWCNT research: when viewed in cross-section, these nanotubes resemble organic molecules that can be described using concepts and methods of molecular physics; but as viewed along the tube axis, they are extended periodic structures suitable for treatment within condensed matter physics.[7]

The goal of this chapter is to provide a brief background on the structure of SWCNTs, followed by optical properties, and the prior methods for sorting as-produced SWCNTs.

1.1. SWCNT structures

Each SWCNT is composed of covalently bonded carbon atoms forming an ordered tubular structure with a specific diameter and a roll-up angle. Approximately two-thirds of SWCNT structures are semiconducting and the rest are metallic or semi-metallic. Semiconducting nanotubes demonstrate versatile optical properties, such as photoluminescence and absorbance due to their intrinsic band gaps directly related to their physical structures.

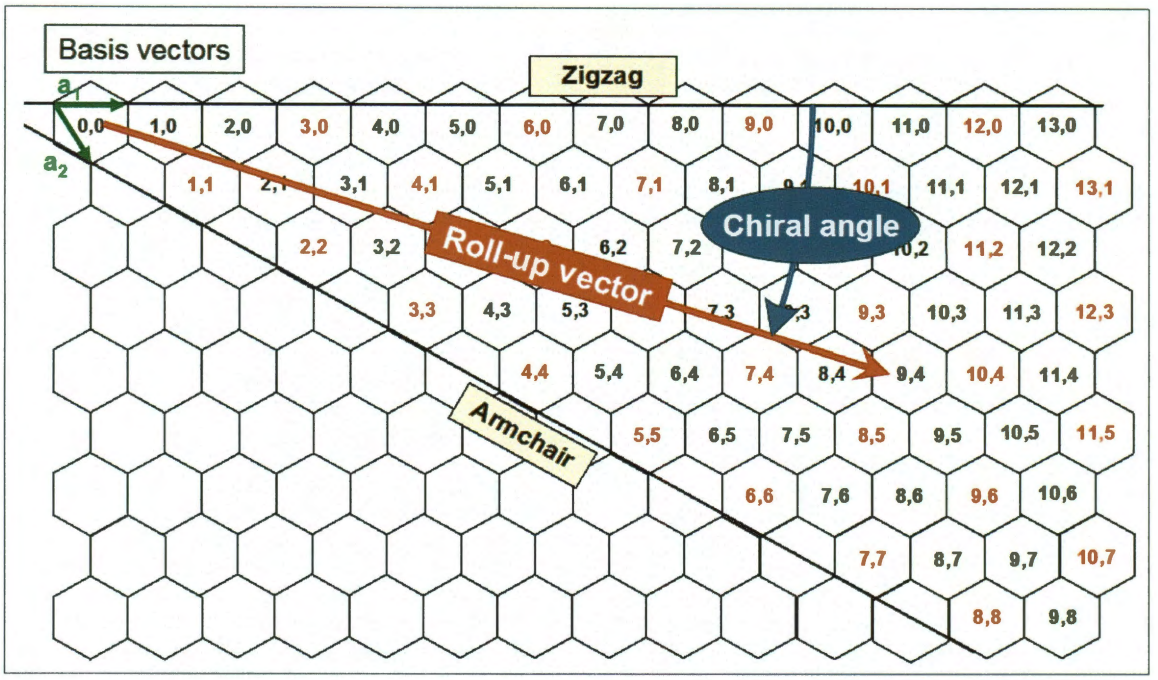

Figure 1.1 A graphene sheet map illustrating possible structures of SWCNT that can be generated by wrapping the sheet to form a seamless cylindrical tube. The resulting nanotube is labeled by a pair of integers in the cell that becomes overlapped with the origin cell. The tube diameter is the length of the roll-up vector divided by π, and the chiral angle can have value between 0° (zigzag) and 30° (armchair). (From ref. 7)

Although SWCNTs are not produced directly from graphite, nanotubes can be considered as sections of single graphene sheet that have been rolled up to form seamless cylinders capped at the ends with hemi-fullerenes.[8,9] This rolling up process generates a large number of possible structures with various tube diameters and chiral angles. As illustrated in Fig. 1.1, each of these distinct structures can be described and labeled by the relative position of hexagonal cells in the graphene sheet (often called a "honeycomb" lattice) that become superimposed after rolling-up. Any arbitrary cell in this honeycomb lattice is chosen as the origin, and then any other cell can be uniquely identified by a pair of integers, denoted by (n,m) indices, relating its displacement in primitive lattice vectors

from the origin cell.[9] These two lattice vectors are defined by a_1 and a_2 in Figs. 1.1 and 1.2. The length of the "roll-up" vector (C_h) connecting two cells in the graphene sheet equals the circumference of the resulting nanotube, where $C_h = na_1 + ma_2$. The angle between the "roll-up" vector and the "zigzag" axis noted in Fig. 1.1 defines nanotube's chiral angle (θ). The tube axis lies perpendicular to the roll-up vector. Chiral angles may have values between 0 and 30° for all unique SWCNT structures.

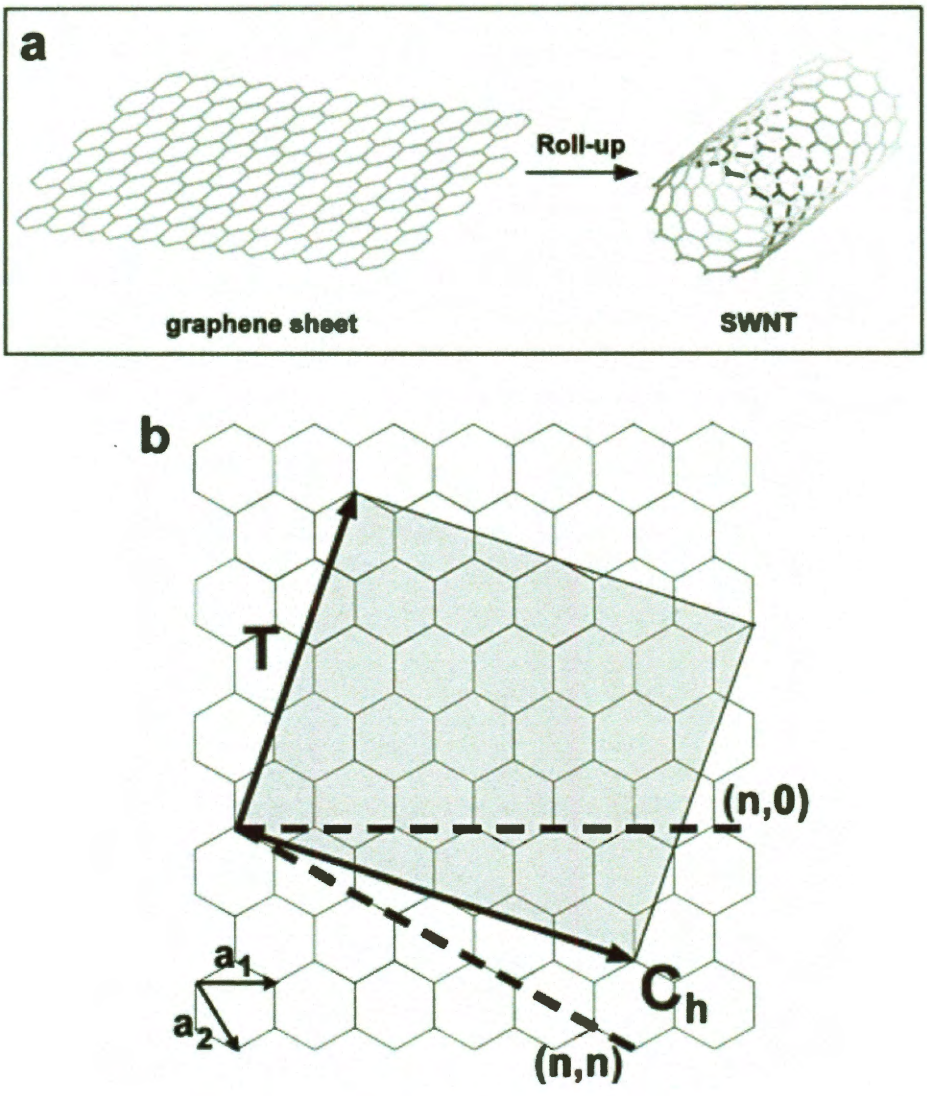

Figure 1.2 Construction of a (4,2) SWCNT from a graphene sheet. (From ref. 9)

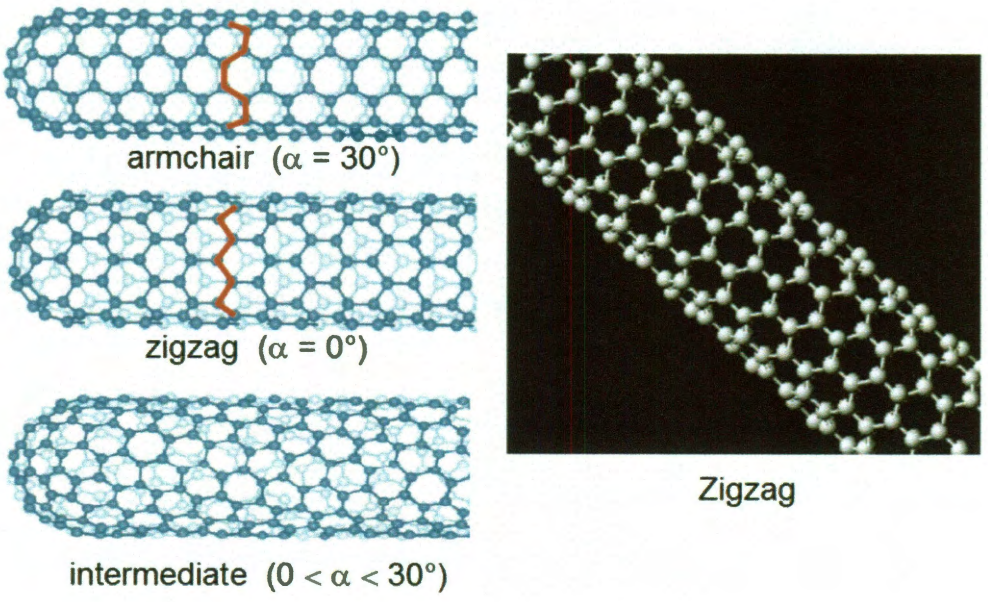

Figure 1.3 SWCNT structures differ in diameter and angle.

A SWCNT with C_h along the "zigzag" direction, dashed line labeled (*n*,*0*) in Fig. 1.2, is termed as a "zigzag" tube. SWCNT in which chiral angle equals to 30° and C_h points along the dashed line labeled (*n*,*n*) is termed an "armchair" nanotube. The rest of the structures with nonzero *n* and *m*, and $0° < \theta < 30°$ are termed "chiral". In Fig. 1.2 the shaded, boxed area represents the unrolled unit cell that constructs a (4,2) SWCNT.

The "armchair" SWCNTs for which $n = m$ have a finite density of electronic states at the Fermi energy level and display metallic electronic behavior. Other nanotube structures for which the quantity $n - m$ is evenly divisible by 3 are semi-metallic, with band gaps smaller than k_BT at room temperature. The remaining SWCNT structures, in which $n - m$ is not evenly divisible by 3, behave as semiconductors. The band gaps of these semiconducting SWCNTs vary approximately inversely with tube diameter.[10] In addition, the quasi-one dimensionality of nanotubes has an important electronic

consequence for all (n,m) structures: it introduces sharp spikes, called van Hove singularities, into the densities of electronic states.

1.2. Origin of band gap photoluminescence in semiconducting SWCNTs

The density of states as a function of band gap energy for a semiconducting SWCNT is shown schematically in Fig. 1.4. Each van Hove singularity (sharp spike) belongs to a different sub-band, labeled with an integer representing the magnitude of those states' angular momentum projection along the nanotube axis.[7]

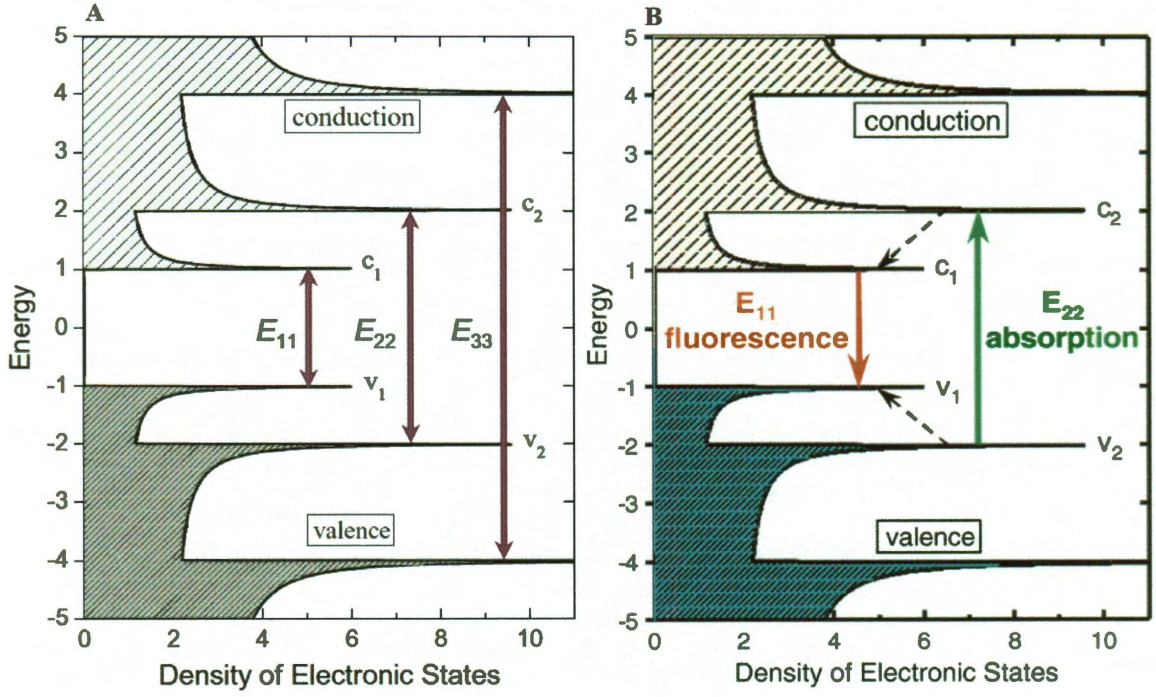

Figure 1.4 (a) Schematic density of states diagram for a semiconducting SWCNT, in a simple band theory model. Allowed optical transitions are illustrated as vertical arrows. **(b)** Solid arrows depict the optical excitation and emission transitions of interest; dashed arrows denote nonradiative relaxation of the electron (in the conduction band) and hole (in the valence band) before emission. (From refs. 7 and 13)

According to a 1D model, optical absorption and emission are dominated by dipole-allowed transitions in which light with matched energy and polarized with its electric vector parallel to the tube axis promotes an electron from a valence sub-band to the corresponding conduction sub-band, conserving the angular momentum projection. In a one-electron model, these transitions are predicted to be most intense when the photon energy matches the energy difference between corresponding van Hove singularities. The absorption and emission spectra of a particular (n,m) species are therefore expected to demonstrate a series of sharp features at energies E_{ii}, where i may have values 1, 2, 3,... relating to the associated sub-bands. These possible transitions are illustrated in Fig. 1.4. For semiconducting SWCNTs with diameters near 1 nm, the first three of these transitions appear in the near-IR, visible, and near-ultraviolet regions.[7]

A breakthrough in spectrofluorimetric study of SWCNTs occurred with the discovery of band gap fluorescence from individualized SWCNTs in 2002.[11] Raw pristine nanotubes grown by the HiPco process[12] were first dispersed into an aqueous solution in presence of SDS (sodium dodecylsulfate) as surfactant. O'Connell and co-workers obtained disaggregated nanotubes, each encased in a cylindrical micelle, by ultrasonically agitating an aqueous dispersion of raw SWCNTs in SDS and then ultracentrifuging to remove tube bundles, ropes, and residual catalyst. Later, Bachilo *et al.* performed spectrofluorimetric measurements on SWCNTs isolated in aqueous surfactant suspensions which revealed distinct electronic absorption and emission transitions for more than 30 different semiconducting nanotube species.[13] By combining fluorimetric results with resonance Raman data, each optical transition was assigned to a specific (n,m) structure. They also demonstrated that fluorescence spectroscopy could be a

standalone tool to rapidly determine the detailed composition of bulk SWCNT samples, providing distributions in both tube diameter and chiral angle. Figure 1.5 shows the fluorescence intensity as a function of emission and excitation wavelengths for a disaggregated bulk SWCNT sample grown by HiPco method.[12] Each bright contour peak in emission (for $c_1 - v_1$ transition) and excitation (for $c_2 - v_2$ transition) corresponds to optical transitions of a particular semiconducting (n,m) species.

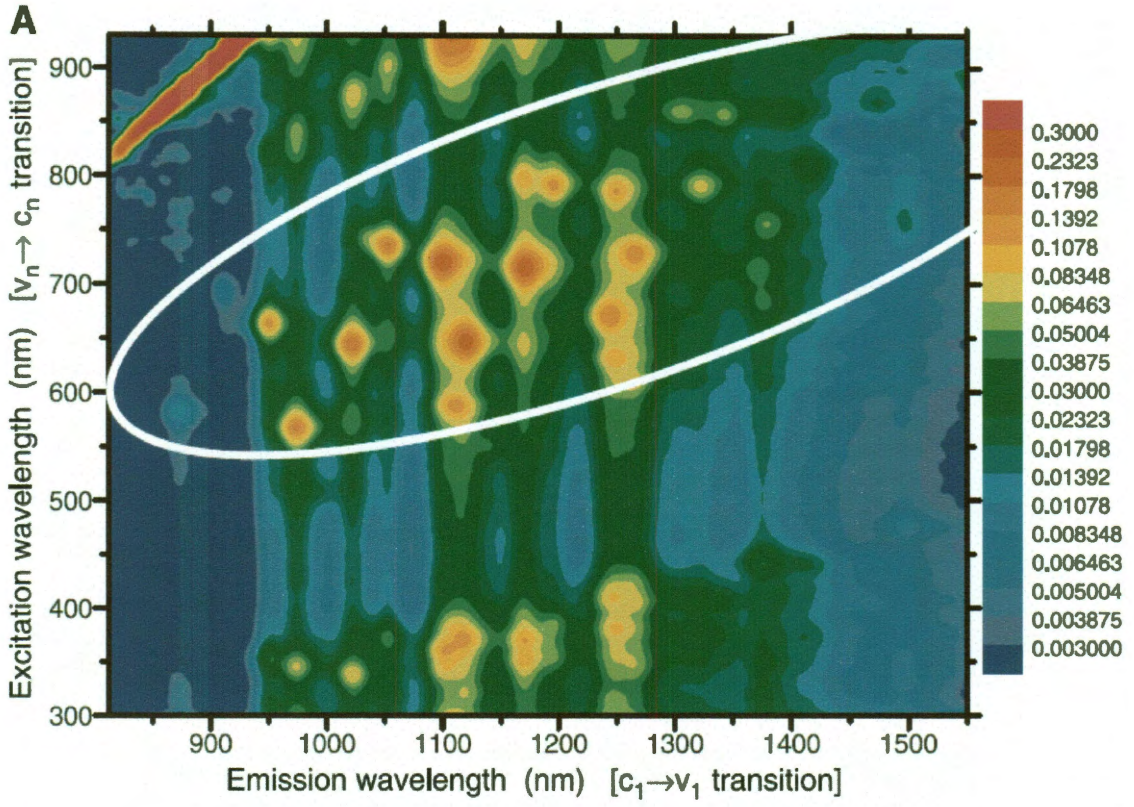

Figure 1.5 Contour plot of fluorescence intensity versus emission and excitation wavelength for surfactant-coated SWCNTs in aqueous suspension. (From ref. 13)

This diagram leads to another important plot (Fig. 1.6) showing resonant excitation wavelength of semiconducting SWCNTs as a function of emission wavelength. This plot is quite helpful in selecting excitation lasers suitable for nanotube near-IR spectroscopy.

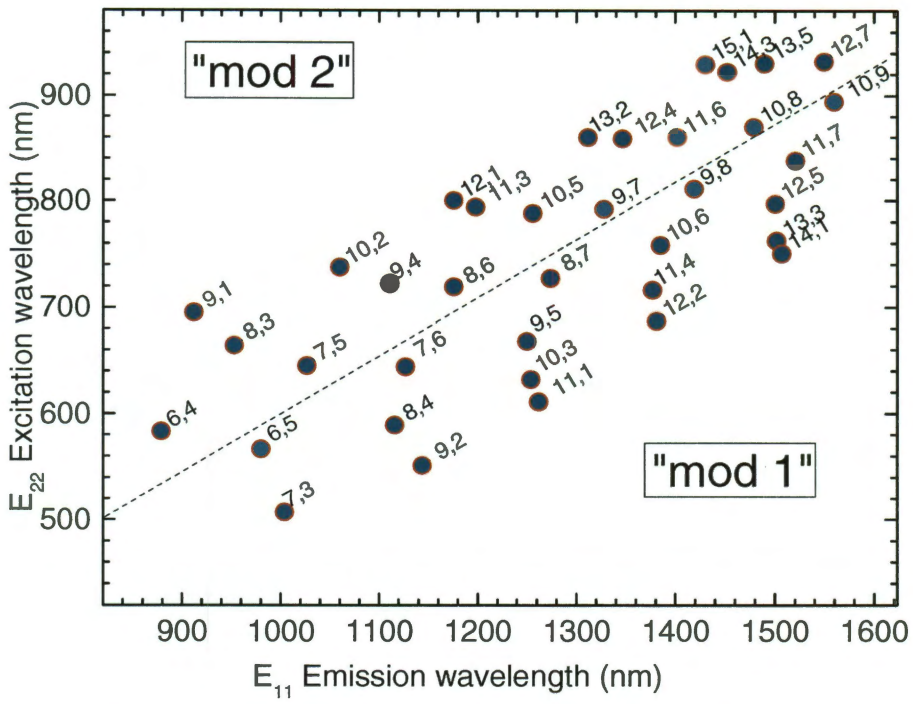

Figure 1.6 Resonant excitation *vs.* emission wavelengths of HiPco SWCNTs dispersed in aqueous SDBS suspension. (From ref. 7)

1.3. Sorting of SWCNTs

Many potential applications require pure nanotube samples. To achieve optimal performance in various fundamental studies and technological applications, populations of SWCNTs should be monodisperse with respect to diameter and electronic types. A number of advanced applications including field-effect transistors,[14] nano-scale sensors,[15] conductive films,[16,17] and optimized near-IR fluorophores[7]-therefore require samples with little or no structural variation. The current processes for SWCNT growth generally produce complex mixtures that contain many chiralities. Consequently, there have been intense efforts to develop post-growth techniques for sorting SWCNTs by diameter, electronic type, and length.

Besides achieving the highest possible purity, the SWCNT sorting strategies need to be: (a) nondestructive; the fundamental properties of SWCNT should not degrade due to sample processing. (b) Compatible with the wide range of SWCNT lengths and diameters that are present in as-synthesized SWCNT material, specifically in HiPco-grown tubes. (c) Easily reproducible and repeatable to achieve improved purity levels. (d) Scalable. (e) Affordable, thus enabling economical incorporation into target applications. Overall, SWCNT sorting strategy should be aimed to meet these additional criteria to support commercial applications. In general, nondestructive sorting methods for pristine SWCNTs include dielectrophoresis to separate metallic from semiconducting species,[18] ion exchange chromatography to isolate single (*n,m*) species,[19-21] and density gradient ultracentrifugation (DGU); a method used in biology for separating subcellular components with differing buoyant densities.[22,23]

1.3.1. Electrophoretic separation of SWCNTs

Electrophoresis sorting of SWCNTs is performed according to their relative mobility through a gel medium, capillary or solution in response to a direct current (d.c.) electric field. In gel electrophoresis, nanotubes with shorter length (smaller molecular weight) travel faster, thus leading to sorting by length. Furthermore, the diameter-dependence of SWCNT cutting during the ultrasonication process allow the length sorting of gel electrophoresis with diameter sorting to some extent.[24] In the same way, capillary electrophoresis leads to length sorting of SWCNTs.[25] This technique can be further utilized to separate individually encapsulated SWCNTs from bundles.[26] Krupke *et al.* demonstrated a method to separate metallic from semiconducting SWCNTs in suspension using alternating current (a.c.) dielectrophoresis.[18] Effective electronic type

sorting was achieved by utilizing the dielectric constant difference between metallic and semiconducting SWCNTs. Fig. 1.7 depicts an illustration of the experimental setup used to sort SWCNTs by electronic type. A drop of nanotubes suspended in solution was placed on a microelectrode array. Upon application of an a.c. electric field, the more polarizable species (metallic SWCNTs) are selectively deposited onto the substrate between the microelectrodes. The electric field also induces nanotube alignment. Subsequent work has confirmed that sorting by electronic type improves with increasing frequency of the electric field.[27,28]

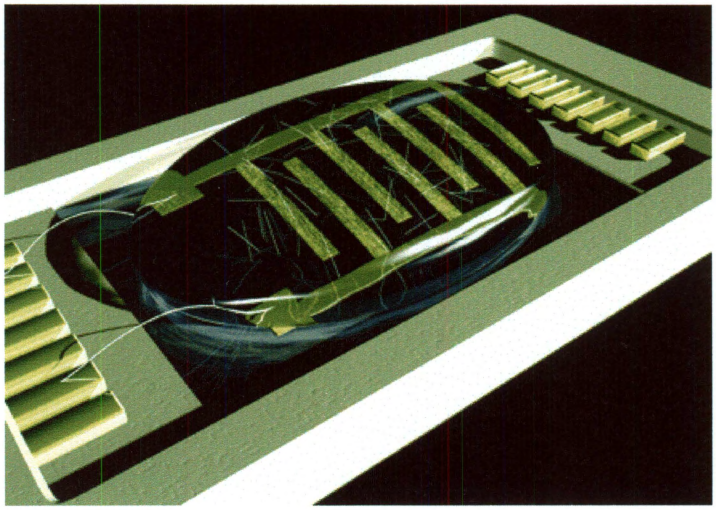

Figure 1.7 Illustration of the experimental setup for (a.c.) dielectrophoresis showing microelectrodes wired to a chip carrier. The metallic nanotubes (black) are deposited from a drop of nanotube suspension onto the electrodes by ac dielectrophoresis, leaving the semiconducting tubes in suspension. (From ref.18)

In addition, the concurrent use of cationic and anionic surfactants improved electronic type separation by neutralizing surface charges on the semiconducting SWCNTs. The obvious disadvantage of dielectrophoretic sorting with microelectrode arrays is limited output (for example, the original experiments isolated 100 picograms of metallic SWNCTs). Consequently, recent work has focused on attempts to scale-up

yields using larger electrodes or dielectrophoretic field-flow fractionation (FFF). The latter approach also has shown evidence for diameter sorting among semiconducting SWCNTs.

1.3.2. Sorting of SWCNTs by ion-exchange chromatography

Several chromatographic approaches have been investigated to sort SWCNTs by diameter and electronic type. Sorting of single-stranded DNA-wrapped SWCNTs using

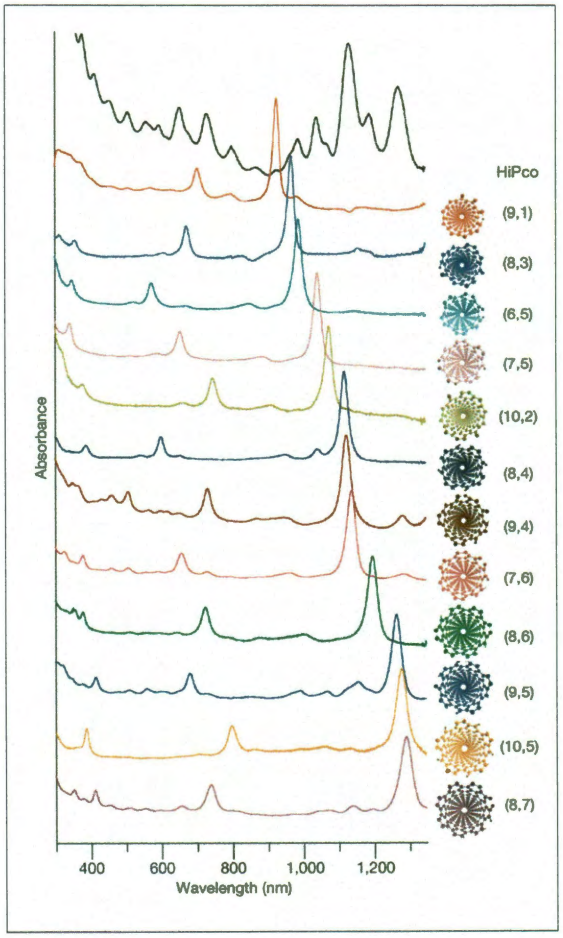

Figure 1.8 Ultraviolet–visible–near-infrared absorption spectra of 12 purified semiconducting SWCNTs (ranked according to the measured E_{11} absorption wavelength) and the starting HiPco mixture. The structure of each purified SWCNT species (viewed along the tube axis) and its (*n*,*m*) notation are given at the right side of the corresponding spectrum. (From ref. 21)

ion-exchange chromatography (IEX) has shown the most promise. In this approach, nanotubes were first individually encapsulated with single-stranded DNA in aqueous solution.[29] The purity of sorted fractions was confirmed by optical absorbance measurements. The optical property differences in the resulting IEX samples were remarkably high. Fluorescence and Raman spectroscopy also confirmed successful SWCNT sorting. Subsequent research showed that the sorting quality depends on DNA sequence, with a sequence of $(GT)_n$ where, G stands for guanine and T for Thymine, and n is 10 to 45.[19]

Theoretical work has concluded that the effective charge density of the DNA–SWCNT hybrid, primarily governed by the DNA helical pitch, is the dominant factor for the IEX sorting process.[30] In a recent report, the DNA sequences identified by Tu *et al.* showed higher selectivity for semiconducting SWCNTs than for those that have metal-like conductivities, and sorted twelve different semiconducting species with significantly higher purity (Fig. 1.8).[21] However, this approach is also relatively expensive (because of the high cost of DNA), which is an obstacle to the large-scale separation.

1.3.3. Sorting of SWCNTs by gel chromatography

In order to separate metallic and semiconducting SWCNTs with high purities researcher have explored a variety of agarose gel materials with different pore sizes.[31,32] When SWCNTs in SDS-dispersion were applied to a column containing agarose gel beads, semiconducting SWCNTs were trapped by the beads, while metallic SWCNTs passed through the column. To extract semiconducting SWCNTs adsorbed by the beads, the columns were eluted with sodium deoxycholate solution and used for repeated separation.[31,33] Recently, Liu *et al.* reported a simple multi-step method for the large-

scale semiconducting chirality separation of SWCNTs using single-surfactant multicolumn gel chromatography with a series of vertically connected columns.[34] This method was based on the structure-dependent interaction strength of SWCNTs with an allyl dextran-based gel. The overloading of SWCNT suspension on the top column resulted in the adsorption sites of the column becoming fully occupied by the nanotubes. The unbound SWCNTs flowed through to the next column, and the nanotubes with the second strongest interaction with the gel were adsorbed in this stage. However reproducibility of this method is still in question.

1.3.4. Sorting of SWCNTs by density gradient ultracentrifugation

Density gradient ultracentrifugation (DGU) has recently emerged as a technique for sorting as-grown mixtures of single-walled nanotubes into their distinct (*n*,*m*) structural forms. In 2005, Arnold *et al.* described the first sorting of SWCNTs by linear DGU,[35] a method used in biology for separating subcellular components with differing buoyant densities.[22,23] Samples were added to centrifuge tubes containing liquid mixtures arranged to form a spatially varying density profile. Under strong centrifugation, sample components separated by migrating to regions matching their individual densities.

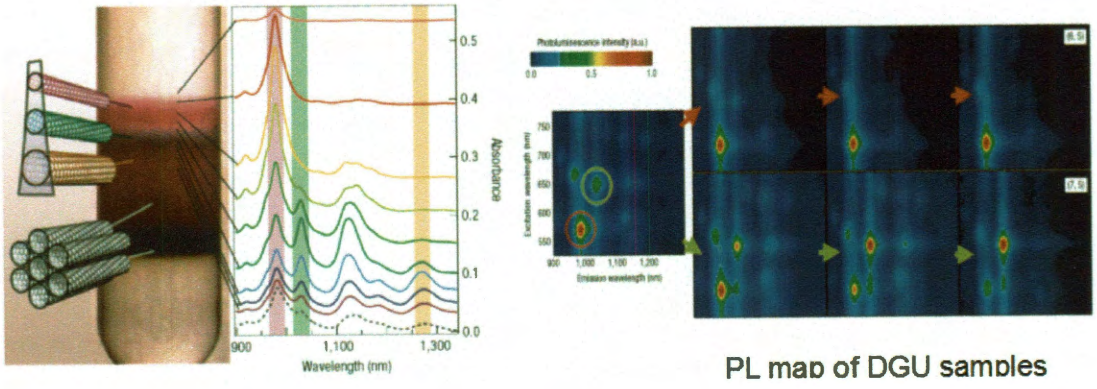

Figure 1.8 *(n,m)* sorted samples were obtained from surfactant-coated SWCNTs. Repeated linear DGU showed significant enrichment of (6,5) and (7,5). (From ref. 36)

Hersam and co-workers demonstrated that DGU can separate metallic from semiconducting SWCNTs and provide fractions strongly enriched in the (6,5) and (7,5) species.[36] Iodixanol was the dense component of their linear density gradients, and sodium cholate (SC) or SDS were coating agents used to individually suspend nanotubes. However, this approach has been limited to samples containing only a small number of nanotube structures, and has often required repeated DGU processing.

1.3.5. New approach: nonlinear DGU for sorting of HiPco SWCNTs

Researchers applying DGU for (*n*,*m*) sorting have focused their efforts on samples grown by the CoMoCAT or similar processes.[37,38] These contain a limited range of (*n*,*m*) species,[38,39] which may simplify separations but limits the number of isolable structures. HiPco-grown[12] SWCNT samples offer a much wider range of (*n*,*m*) enrichment targets (more than 30 semiconducting plus many metallic species).[13] However, reported DGU-based HiPco separation efforts, employing covalent functionalization[40] or novel surfactants,[41,42] have not enriched species other than (6,5), (8,3) and (7,5). The major challenge in (*n*,*m*) sorting of pristine HiPco samples by DGU is discriminating multiple species that differ only slightly in diameter and have nearly equal buoyant densities. In conventional linear density gradients, layers containing nearby species overlap and (*n*,*m*) resolution is essentially lost. We have instead introduced tailored nonlinear DGU (termed as "NDGU") designed to resolve targeted SWCNT species, allowing their extraction as (*n*,*m*)-enriched fractions from HiPco samples. The use of tailored NDGU significantly improved (*n*,*m*) separations.[43] We found that highly polydisperse samples of SWCNTs grown by the HiPco method are readily sorted in a single step to give fractions enriched

in any of ten different (*n,m*) species. Furthermore, minor variants of the method allow separation of the mirror-image isomers (enantiomers) of seven (*n,m*) species.

CHAPTER 2

SORTING OF SWCNTs BY NONLINEAR DENSITY GRADIENT ULTRACENTRIFUGATION

2.1. Introduction

The effectiveness of our new sorting approach is demonstrated by extracting fractions substantially enriched in ten different (*n*,*m*) species through a single step of NDGU processing. To illustrate how the enriched fractions can elucidate spectral transitions obscured in mixed samples, we have shown the first spectroscopic signatures of (10,0) and (11,0), two zigzag species previously undetected in HiPco samples.[10] Our improved NDGU method is also adapted to separate left-handed from right-handed nanotubes by exploiting the preferential affinity of the chiral surfactant (SC) for one enantiomeric form of each (*n*,*m*) structure. Using NDGU with mixed surfactants, we achieved superior resolution and separated several enantiomers, for a total of seven resolved pairs. Experimental parameters were tuned for effective separation with a vertically scanned near-IR spectrofluorometer that quickly maped locations of semiconducting SWCNT species inside unperturbed post-NDGU centrifuge tubes.

In this extensive study on developing a new approach for efficient sorting of SWCNTs we mainly focused on the following factors: (a) the shape of density profile and how it influenced the overall sorting process. (b) The role of surfactant(s) in DGU medium. (c) Optimization of surfactant concentration in unsorted HiPco material and in the DGU medium. (d) Nanotube sample preparation prior to DGU runs. (e) The amount of unsorted SWCNT material required to balance between quality and quantity of final yield.

2.2. Centrifugation basics

Centrifugation is a technique designed to utilize centrifugal forces to speed up the sedimentation rate of particles. This is achieved by spinning centrifuge tubes containing the mixture of fluid and polydisperse particles about an axis of rotation so that the particles experience a force moving them away from the rotational axis. During centrifugation, particles suspended in a fluid move towards the bottom of a centrifuge tube at a rate depending upon their size and density. In addition, sedimentation of particles only occurs if density of the fluid is lower than the density of the particles. The machine that spins sample filled tubes is called a centrifuge and the device that holds centrifuge tubes as they rotate about the axis is called a rotor. The relative centrifugal force (r.c.f.) produced by rotor is dependent on two factors: the speed of the rotor defined by revolutions per minute (RPM) and the radius of rotation, which is the distance from rotational axis of the rotor. Therefore, particles further from the rotor axis will experience a greater sedimentation force than those nearer to the axis.[23]

The rate of sedimentation of particles in a centrifuge tube is governed by the Stokes equation describing the movement of a sphere through a liquid in a gravitational field. When velocity of the sphere reaches a constant value, the centrifugal force on the sphere is equal in magnitude to the frictional force resisting its motion through the liquid.[23] The relationship between the particle velocity, medium, and centrifugal field is shown in the following equation:

$$\frac{1}{6}\pi d^3(\rho_p - \rho_l)g = 3\pi d\mu v \qquad (2.1)$$

Where, v = sedimentation velocity of the particle; d = diameter of the particle; ρ_p = density of the particle; ρ_l = density of the liquid; g = centrifugal acceleration; μ = viscosity of the liquid. Equation 2.1 can be rearranged to the form:

$$v = \frac{d^2(\rho_p - \rho_l)g}{18\mu} \qquad (2.2)$$

From above equation it can be seen that sedimentation rate of a particle is proportional to its size, and to the difference between the density of the particle and the density of surrounding medium. So there will be three conditions. The particle will (a) sediment if $\rho_p > \rho_l$, (b) float on the liquid if $\rho_p < \rho_l$; (c) not move if the particle density is equal to that of the medium ($\rho_p = \rho_l$). Condition (c) in principle, governs the equilibrium buoyant density separation.

2.2.1. Isopycnic separation of particles

Isopycnic separation method separates particles on the basis of their buoyant density differences. This is achieved by loading sample in the middle of a preformed density gradient. When centrifugation is carried out for a sufficient time at a right temperature to allow all the particles to reach the region of gradient where density of the medium matches that of particles (where $\rho_p = \rho_l$ and $v = 0$), the system is said to be isopycnic. Thus, particles with comparable density are sorted into different isopycnic bands.

2.3. Density gradient ultracentrifugation (DGU)

Density gradient ultracentrifugation (DGU) has emerged to be one of the most widely used techniques for the routine purification of biological particles in order to

achieve higher degree of resolution during separation.[23,44] A density gradient consists of a solution that increases in density from the top to the bottom of the centrifuge tube. According to initial layering techniques, gradients can be continuous, in which density of the medium increases gradually throughout the length of the centrifuge tube, or discontinuous, where density increases in discrete steps. In general, a density profile graph plots the density of the medium as a function of depth in the centrifuge tube. The final shape of a density profile can be linear or nonlinear depending on the manner in which the gradient is prepared and on the viscosity medium used for formation of the gradient.

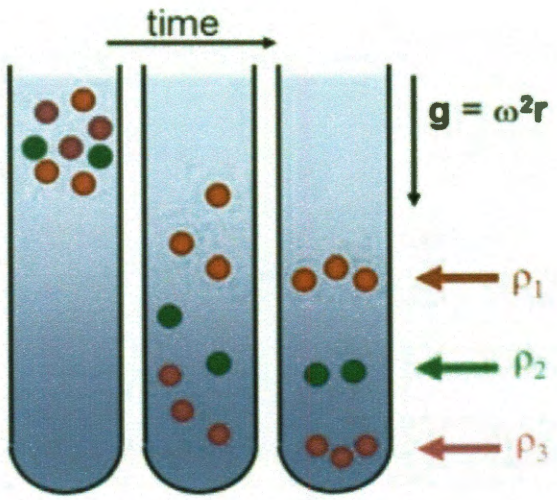

Figure 2.1 Redistribution of particles along a centrifuge tube after DGU. (From ref. 23)

The final density profile of a gradient (after centrifugation) is an important factor which determines the degrees of separation. The density profile depends on sedimentation path-length of the rotor, centrifugation speed, time of centrifugation, and temperature. Therefore, in our study we tried to tune these factors to optimize purity and yield of (*n,m*) sorted SWCNT species.

2.3.1. Density gradient medium

The principal ingredient for any DGU-based separation is the density gradient medium, which should be capable of forming solutions over a wide range of densities. In addition, viscosity of the medium is a major factor in determining sedimentation rate of particles passing through the fluid. In our study, density gradients are created by mixing a density modifier, iodixanol, purchased from Sigma-Aldrich as "OptiPrep". Optiprep is a sterilized stock solution of 60% (w/v) iodixanol in water, produced by dissolving solid iodixanol power in distilled water. Additionally, iodixanol solution does not interfere with surfactant-coated SWCNTs and stable over wide range of temperatures.

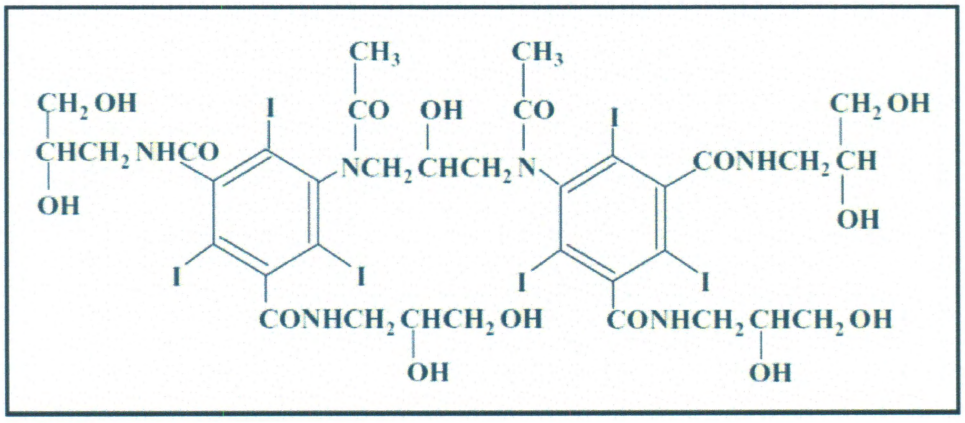

Figure 2.2 Molecular structure of iodixanol (density gradient medium). (From ref. 23)

2.3.2. Layering technique for preformed gradients

Before centrifugation, gradient layers are formed by carefully inserting iodixanol solutions of decreasing density into a centrifuge tube, so that sharp interfaces are formed between different density regions.[23,44] This is achieved by adding a series of discrete layers with specific densities and volumes using a glass Pasteur pipette attached to a pipette pump and then letting them mix by diffusion.

2.3.3. Nonlinear density gradient ultracentrifugation (NDGU)

In order to achieve more resolved separation of similar density particles it is often worthwhile to use nonlinear DGU (termed as "NDGU") instead of linear DGU. If density of medium is not a linear function of depth in centrifuge tube, it is described as nonlinear. A nonlinear gradient can be concave, convex, s-shaped or complex by nature. A shallow nonlinear density gradient may be effective in separating particles of similar density, such as surfactant coated SWCNTs, where buoyant density varies slowly with nanotube diameter.

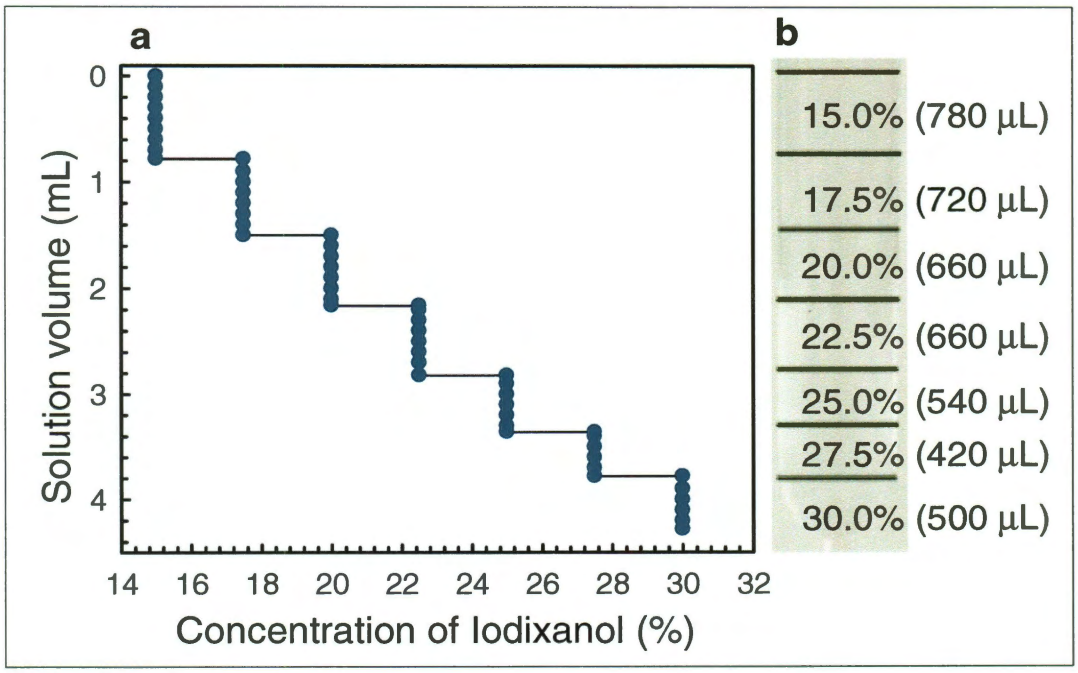

Figure 2.3 Layering of nonlinear density gradients. **(a)** Solution volume as a function of iodixanol concentration. **(b)** A centrifuge tube showing concentration and volume of iodixanol layers required to form nonlinear gradient for sorting of SWCNTs (discussed later).

In contrast, after ultracentrifugation linear density gradient creates a steep density profile, thus the resolution is not sufficient enough to sort particles with similar buoyant

densities. In our study, we found that an s-shaped density profile with slowly varying density (discussed later) remarkably improved the quality of nanotubes sorting in a single NDGU step. To form a nonlinear gradient a set of layers with densities that are nonlinear to the depth in the centrifuge tube are added and then allowed to diffuse by keeping the centrifuge tube at a small angle from the horizontal. By gradually increasing the volume of each layer we prepare a gradient with a curved form. After diffusion of layers, the unsorted SWCNT sample is loaded in a predefined region with matched density by mixing with excess stock iodixanol solution.

2.3.4. Surfactants for sorting SWCNTs

For efficient dispersion of SWCNTs in aqueous suspension we use sodium cholate (SC) purchased from Acros Organics (99% pure, cholic acid sodium salt). SC is a cholic acid derivative and a kind of bile salt. It is a molecularly rigid planar amphiphile suited for dispersing SWCNTs.[45] SC-coated nanotubes are rather stable under strong centrifugal force. We explored different concentrations of SC (0.7% - 1%) to optimize nanotube sorting by diameter. In addition, low concentrations of anionic alkyl amphiphiles, such as sodium dodecylsulfate (SDS) purchased from Acros Organics (99% pure) were introduced for sorting of nanotube enantiomers.

2.3.5. Buoyant density model of a surfactant coated nanotube

To understand how density of a micelle-enclosed nanotube varies with the nanotube internal diameter we used a simple model for the density of a hydrated and surfactant coated nanotube (Fig. 2.4). When coated by a mono-layer of surfactant, the effective density ρ_{SWCNT} of a nanotube of diameter d can be determined from the following equation,[35]

$$\rho_{SWCNT} = \frac{\rho_s \pi d h + \rho_{ext} \pi \left[\left[\frac{d}{2} + t \right]^2 - \frac{d^2}{4} \right] h}{\pi \left[\frac{d}{2} + t \right]^2 h} \qquad (2.3)$$

Here, ρ_s = average surface density of a SWCNT; ρ_{ext} = density of surfactant layer; t = thickness of surfactant layer; h = length of the tube. The van der Waals diameter of carbon = 0.34 nm. For a SWCNT in vacuum, t = 0 and ρ_{ext} = 0, the above expression becomes: $\rho_{SWCNT} = \frac{4\rho_s}{d}$ and the buoyant density inversely varies with tube diameter.

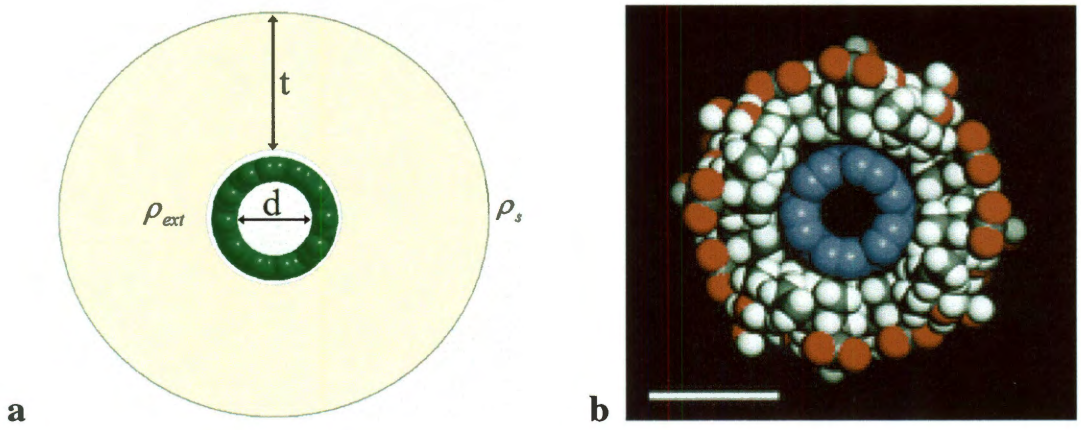

Figure 2.4 (a) Simple model for determining the density of a hydrated and surfactant coated SWCNT micelle. Here, d is the diameter of the nanotube, t is the thickness of the surfactant layer, ρ_{ext} is the density of the surfactant layer, and ρ_s is the sheet density of one graphene layer (the surface of the SWCNT). **(b)** Cross-sectional model of an individual (6,5) SWCNT in a cylindrical sodium cholate micelle (without water). Red, white, and blue atoms represent O, C (as part of cholate), C (as part of nanotube) respectively. (From refs. 35 and 45)

However, experimental measurements for DGU sorted SWCNTs suggest that ρ_{SWCNT} increases with increasing tube diameter.

To find out the limiting values of ρ_{SWCNT}, equation 2.3 is differentiated with respect to nanotube diameter:

$$\frac{\partial \rho_{SWCNT}}{\partial d} = -\frac{4[d\rho_s - 2\rho_s t + \rho_{ext} dt]}{[d+2t]^2} \qquad (2.4)$$

Thus, density of the suspended nanotube increases with increasing diameter up to a critical value, d_{max}. To estimate the value of d_{max}, we set $\frac{\partial \rho_{SWCNT}}{\partial d} = 0$. Thus d_{max} becomes $\frac{2\rho_s t}{\rho_s + \rho_{ext} t}$. For $\rho_s = 7.4\text{x}10^{-8}$ g cm^{-2}, $\rho_{ext} = 1.02$ g cm^{-3}, and $t = 2$ nm, we obtain a value of d_{max} as 1.06 nm. So, in principle, DGU is capable of sorting SWCNTs of diameter up to ~1.06 nm, which primarily agrees with the experimental data shown in Fig. 2.14.

2.4. Experimental details

2.4.1. Determination of the density (ρ) of aqueous iodixanol solution

Once gradients have been fractionated, it is often important to measure the density of each fraction accurately. The most direct method is to weigh a known volume of fractionated sample using a microbalance and calibrated pipette setup; however, this procedure requires very precise weight measurement. A more convenient way is to determine the density of a fraction by measuring the refractive index, which has the added advantage of requiring as little as 10-20 µl of sample.

Concentration of iodixanol (c) (%)	Refractive index (η)	Density (ρ) (g/mL)
0.0	1.3348	0.9982
2.5	1.3388	1.0119
5.0	1.3422	1.0235
7.5	1.3466	1.0387
10.0	1.3501	1.0508
12.5	1.3539	1.0635
15.0	1.3580	1.0777
17.5	1.3623	1.0925
20.0	1.3654	1.1029
22.5	1.3700	1.1188
25.0	1.3740	1.1323
27.5	1.3773	1.1439
30.0	1.3821	1.1602

Table 2.1 Concentration, refractive index and density of aqueous iodixanol with 0.7% SC

The simple linear relation between optical refractive index (η) and density (ρ) is defined by, $\rho = A\eta - B$; where A and B are two constants. The refractive index of a solution increases with the amount of solute present in solution. A calibration plot relating refractive index to the concentration of iodixanol (with 0.7% SC) is shown in Fig. 2.5. This calibration plot is quite linear. Its slope and intercept were used to deduce the concentration of iodixanol in NDGU fractions. Additionally, density measurements for fractions collected from different heights of a centrifuge tube before and after a NDGU run allowed us to optimize NDGU protocols.

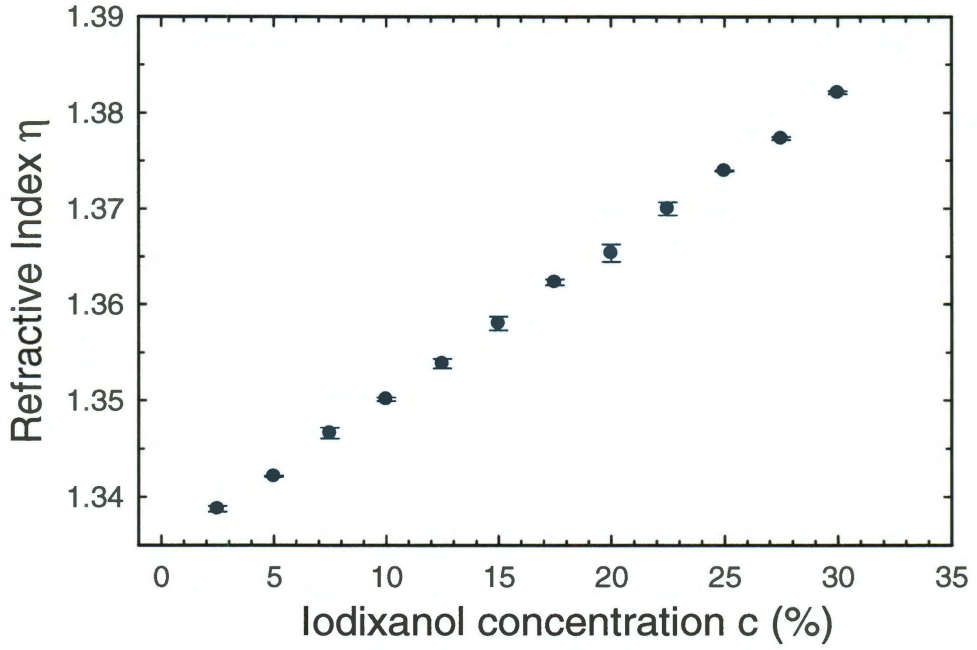

Figure 2.5 Calibration plot for calculation of iodixanol densities from optical refractive indices. Here, refractive indices are plotted as a function of known iodixanol concentration, with 0.7% (w/v) SC added to iodixanol before measurement.

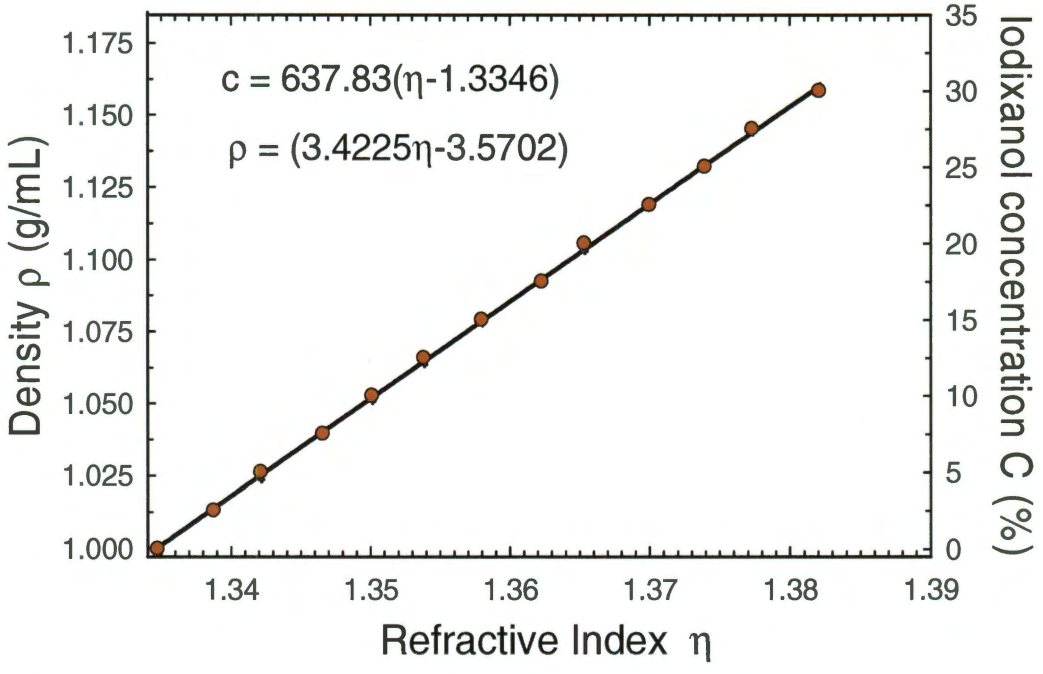

Figure 2.6 Density and corresponding iodixanol concentration as a function of refractive index.

2.4.2. Polydispersity of SWCNTs grown by HiPco process

HiPco SWNCT samples may contain more than 30 semiconducting (*n,m*) species with diameters between ~0.69 and 1.2 nm.[13] They are therefore thought to be more difficult to sort into pure single (*n,m*) species than nanotube samples containing relatively few species, such as CoMoCAT (SWeNT, Norman, OK).[37]

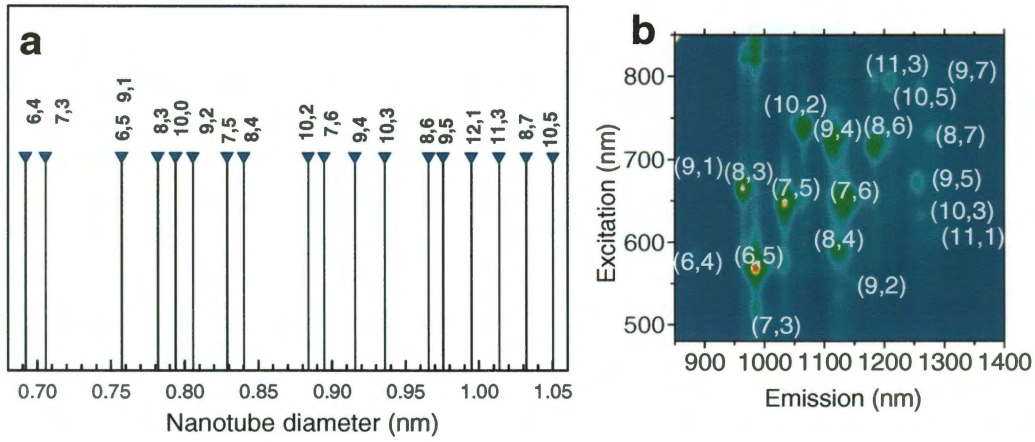

Figure 2.7 Unsorted HiPco SWCNTs. **(a)** Semiconducting (*n,m*) species common in HiPco SWCNTs. **(b)** Photoluminescence emission intensities shown as a function of excitation and emission wavelengths for raw pristine HiPco (batch HPR 188.4) dispersed in 1% (w/v) SC-water solution. Unsorted sample shows signature of ~20 semiconducting (*n,m*) species.

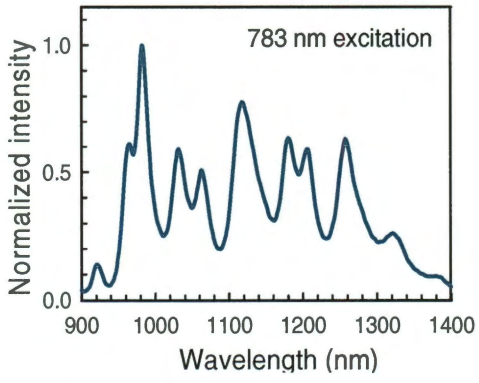

Figure 2.8 Fluorescence emission spectrum of an unsorted HiPco SWCNT sample dispersed in aqueous SC solution.

(n,m)	d (nm)	α(deg)	λ_{11} (nm)	λ_{22} (nm)
6,4	0.69212	23.41322	888	583
9,1	0.75735	5.20872	924	695
8,3	0.78191	15.29534	962	667
6,5	0.75735	26.99551	986	570
7,3	0.70565	16.99609	1005	507
7,5	0.82887	24.50363	1035	647
11,0	0.873	0	1049	746
10,2	0.88406	8.94828	1065	739
9,4	0.91559	17.48017	1117	726
8,4	0.8402	19.10661	1125	591
7,6	0.8947	27.45708	1135	650
9,2	0.80573	9.82643	1150	555
10,0	0.794	0	1175	539
12,1	0.99477	3.96323	1182	802
8,6	0.96584	25.285	1187	720
11,3	1.0136	11.74153	1213	796
9,5	0.97558	20.633	1267	674
10,3	0.93601	12.73053	1272	638
10,5	1.05025	19.10661	1270	792
8,7	1.03209	27.79577	1277	729

Table 2.2 Structures and first and second van Hove optical transition peak wavelengths for twenty semiconducting SWCNT species dispersed in aqueous SC solution. Peak positions are red-shifted compared to those in SDS suspensions. Overall, ten semiconducting SWCNT species (highlighted in yellow) were enriched by NDGU. Note that two zigzag structures, (10,0) and (11,0), are included in the list.

Spectral congestion due to overlapping of emissions from nearby species complicates the spectral analysis.[46] Therefore, in most cases it is difficult to extract the contribution from a particular (*n,m*) species. However, this problem could be solved to some extent by providing Voigt fits with necessary basis functions (Fig. 2.9). In contrast, nearly monodisperse SWCNTs sorted by NDGU enable more detailed fundamental studies due to reduced spectral overlap.

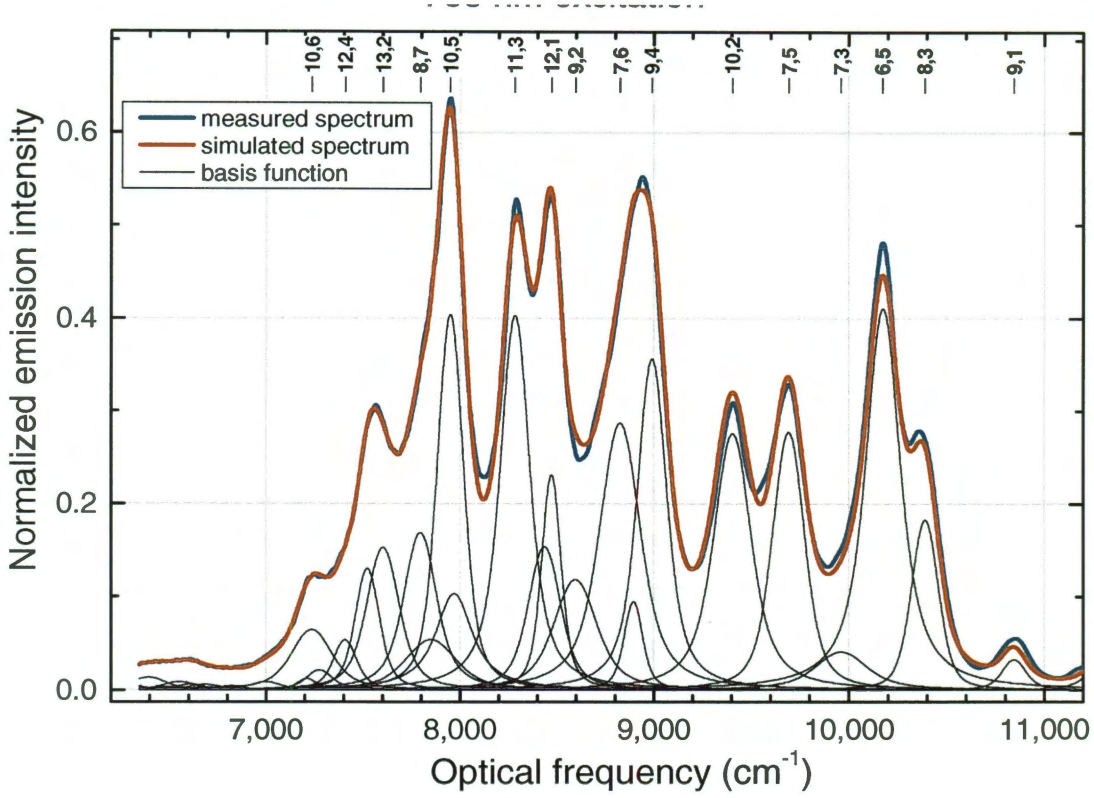

Figure 2.9 Measured fluorescence emission from unsorted HiPco-SWCNTs (blue), and simulated emission spectra (red) with necessary basis function. (From ref. 46)

2.4.3. Sample preparation

2.4.3.1. Raw HiPco SWCNTs

Raw as-synthesized SWCNTs used in this study were produced in the Rice University HiPco reactor (batches HPR 161.2, 188.1, 188.4 and 166.12). We obtained similar results for all batches. Starting with the unsorted raw SWCNTs, we prepared DGU fractions enriched in almost all smaller diameter semiconducting species from (6,4) (0.692 Å) to (7,6) (0.895 Å). In some instances, batch HPR 188.4 was utilized to achieve a higher yield of optically active enantiomers of (6,5), (8,3), (6,4), and (7,3) since that batch had more smaller diameter species than others.

2.4.3.2. Dispersion of raw SWCNTs in aqueous SC solution

As-synthesized raw HiPco SWCNTs were dispersed in water using sodium cholate (SC) as surfactant. An aqueous dispersion of SWCNTs (0.5 mg/mL) in 2% (w/v) SC was prepared by 1 h bath sonication (Sharpertek, Stamina XP) at 25 °C followed by 30 min tip sonication (Microson XL ultrasonic cell disrupter) at an average output power of 7 W with a 3 mm tip. To avoid overheating of the sample during tip sonication the glass bottle containing nanotube sample was immersed in ice water. After tip sonication, an 8 mL sample was split into four 2 mL eppendorf tubes and centrifuged at 13 krpm (~13,000 x g) for 1 h in a benchtop centrifuge (Baxter Scientific, Biofuge-13) to remove residue of catalytic metal particles, bundles and impurities. To achieve optimum separation during nonlinear DGU the average optical density (at 984 nm) of the resultant supernatant was adjusted to ~10 (1 cm optical path), or in some cases, ~7, and used as the starting material for NDGU run. From our study it was clear that too high SWCNT concentration in the starting material deteriorated the sorting resolution due to overlapping of bands.

2.4.4. Formation of nonlinear density gradients – general protocol

Our density gradient medium was an aqueous solution of 60 % (w/v) iodixanol. Gradients were prepared in 13 mm inner diameter, 5.0 mL capacity ultracentrifuge tubes (Seton Scientific, part no. 7022 and 5022) by adding a series of discrete layers with specific densities and volumes and then letting them mix by diffusion. For efficient (*n*,*m*) sorting of HiPco SWCNTs, we manually formed step gradients varying from 30.0% (w/v) iodixanol at the bottom to 15.0% (w/v) iodixanol to the top using a glass Pasteur pipette attached to a pipette pump. The SC concentration in this gradient was fixed at

0.7%. For enantiomeric separation of (6,5) and (7,3) species, a mixed surfactant of 0.7% (w/v) SC and 0.175% SDS (w/v) was used instead.

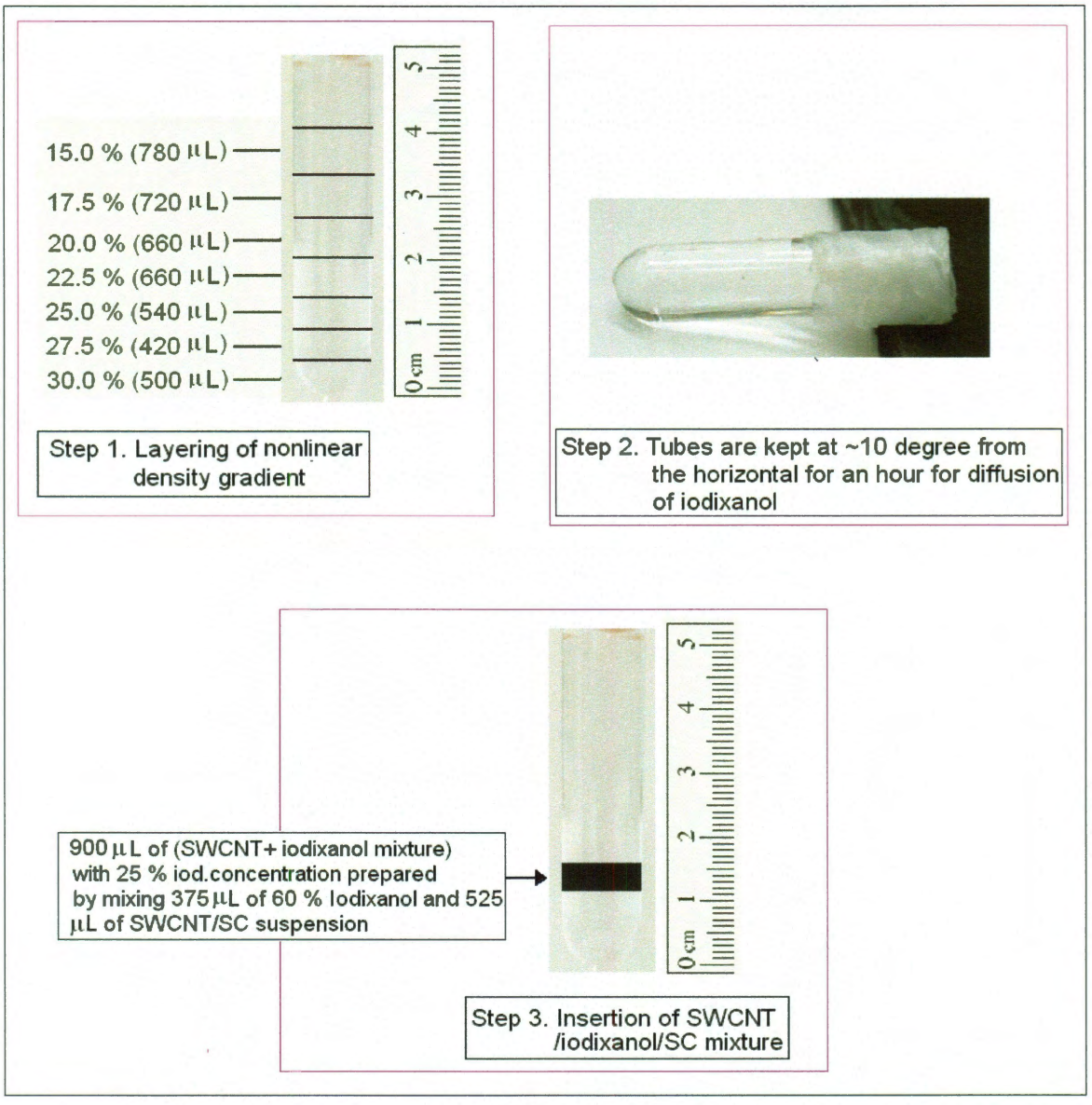

Figure 2.10 Layering steps for nonlinear density gradients in a centrifuge tube.

Table 2.3 Layering protocols for NDGU.

Nonlinear DGU parameters used for racemic and enantiomeric separation of SWCNTs						
Parameter	Racemic (*n,m*) sep'n of (6,4), (7,3), (6,5), (8,3), (7,5), and (7,6)	Enantiomer sep'n of (7,5) and (8,3)	Enantiomer sep'n of (6,5) and racemic sep'n of (6,4), (7,3), and (8,3) [high yield]	Enantiomer sep'n of (8,3) and (9,1)	Enantiomer sep'n of (8,4) and racemic sep'n of (9,2), and (10,2)	Enantiomer sep'n of (6,4), and (7,3)
SC concentration in DGU medium (%)	0.7	0.6	0.7 (*or 0.9*)	0.7	0.9	0.75
SDS concentration in DGU medium (%)	0	0	0.175 (*or 0.225*)	0.175	0.225	0.187
Layer 1 % iodixanol (lowest from the bottom)	30.0	30.0	30.0	27.5	27.5	27.5
Layer 1 volume (microliter)	500	500	500	420	420	420
Layer 2 % iodixanol	27.5	27.5	27.5	25.0	25.0	25.0
Layer 2 volume (microliter)	420	420	420	550	550	545
Layer 3 % iodixanol	25.0	25.0	25.0	22.5	22.5	22.5
Layer 3 volume (microliter)	540	540	540	670	650	660
Layer 4 % iodixanol	22.5	22.5	22.5	20.0	20.0	20.0
Layer 4 volume (microliter)	660	660	660	670	660	660
Layer 5 % iodixanol	20.0	20.0	20.0	17.5	17.5	17.5
Layer 5 volume (microliter)	660	660	660	720	720	720
Layer 6 % iodixanol	17.5	17.5	17.5	16.0	15.5	15.0
Layer 6 volume (microliter)	720	720	725	795	780	780
Layer 7 % iodixanol	15.0	15.0	15.0	0.0	0.0	0.0
Layer 7 volume (microliter)	780	780	785	0	0	0
Diffusional mixing time (min) (tube kept at 10 deg)	60	60	50	60	45	50
Inserted SWCNT sample volume (microliter)	900	900	1000	1200	1000	1200
Iodixanol concentration in inserted SWCNT (%)	25.0	27.5	25.0	25.0	25.0	25.0
Inserted SWCNT surfactant conc. (%SC)	2.00	1.00	2.00	2.00	2.00	2.00
Centrifugation time (h)	18	18	18	20	18	20
Centrifugation RPM (MLS-50 rotor)	50,000	50,000	50,000	50,000	50,000	50,000
Centrifugation temperature	22.0	22.0	20.0	23.0	20.0	22.0
Centrifuge tube part no. (Seton Scientific)	7022	7022	7022 or 5022	5022	7022	5022

For general (*n,m*) sorting of SWCNTs (with single surfactant SC), our nonlinear gradients were prepared from successive layers with the following iodixanol concentrations and volumes: 30% (500 μL), 27.5% (420 μL), 25.0% (540 μL), 22.5% (660 μL), 20.0% (660 μL), 17.5% (720 μL), and 15.0% (780 μL). (Other separations required somewhat different preparations, table 2.3). After layering, the capped centrifuge tube was held at an angle of ~10 degrees from horizontal for 1.0 h to allow diffusional formation of a nonlinear density gradient. Nanotubes were slowly pipetted into the density-matched region of the pre-made gradient in a 900 μL volume containing 375 μL of 60% iodixanol mixed with 525 μL of pre-dispersed SWCNTs in 2% SC solution. The SWCNT concentration before insertion was set to give an average absorbance of ~10.0 per cm at 984 nm (as for E_{11} peak of 6,5 tube). The centrifuge tube was filled to within ~2 mm of its top rim with an aqueous solution of 0.7% SC and centrifuged (with three other tubes) for 18 h at 50,000 rpm (268,000 x g max) and 22 ^{o}C in the MLS-50 swing-bucket rotor of a Beckman Optima^{TM} Max (model MAX -130k) ultracentrifuge. Table 2.3 lists the full set of specific parameters used for the NDGU separations discussed here.

2.4.5. Fractionation of sorted SWCNT samples

Before fractionating the contents of a processed centrifuge tube, we measured fluorescence spectral map of the centrifuge tube using a model NS1 NanoSpectralyzer [46] with vertical scanning option (discussed later). From this map we determined the precise locations (depths) of the layer containing targeted species. We then used a 100 μL syringe (HPLC grade, Hamilton Inc, gas tight fixed needle), or in some cases a 50 μL syringe, attached to a vertically mounted translational stage to access the desired layer.

For (*n*,*m*)-selective separations, 25 μL fractions were collected and then diluted to 100 μL by adding enough 1% SC (w/v) solution for optical absorption, photoluminescence, circular dichroism (CD), and Raman measurements. For enantiomeric separations, we collected 50 μL fractions, instead. The photograph in Fig. 2.11 illustrates the fractionation procedures. To avoid cross contamination, extraction syringe was washed with de-ionized water after a cycle of fractionation.

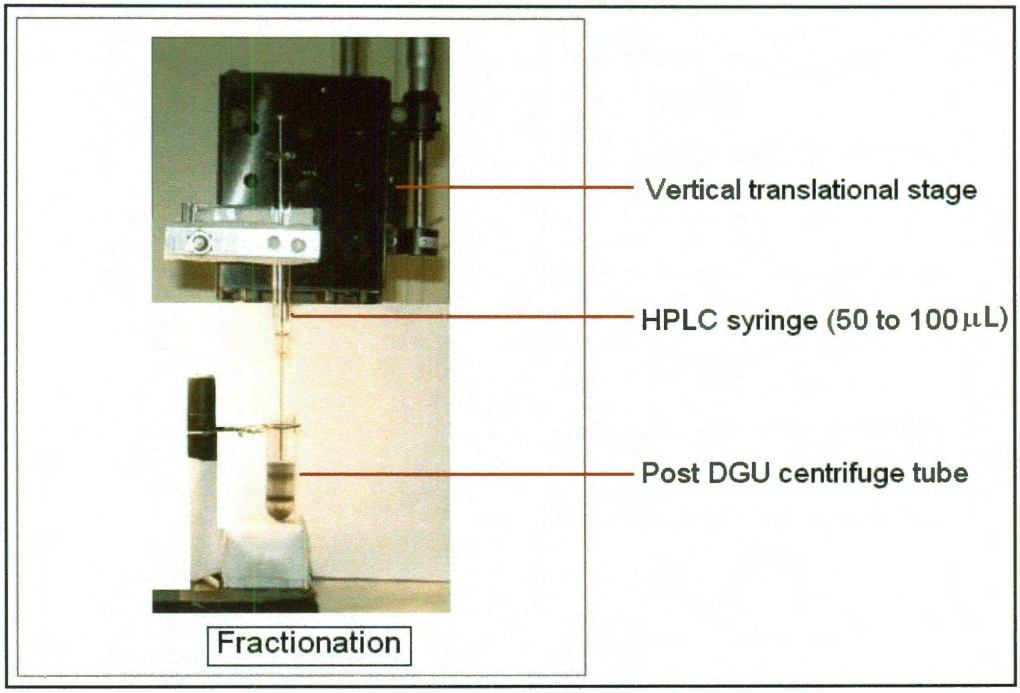

Figure 2.11 Fractionation of sorted SWCNTs from a nonlinear DGU sorted centrifuge tube.

2.4.6. Formation of linear density gradient for comparison with NDGU

Linear density gradients were formed in a MLS-50 sized centrifuge tube by layering 580 μL volumes of premixed aqueous (iodixanol / 0.7% SC) solutions having iodixanol contents ranging from 30.0 to 15.0% by 2.5% steps. The tube was then held at an angle of ~10 degrees from horizontal for 1.0 h to allow diffusional formation of a

linear density gradient. Before centrifugation, 900 μL of SWCNT-iodixanol solution (25% iodixanol content) with 2% (w/v) SC was loaded in the matched region. Centrifugation was carried out in a MLS-50 rotor, at 50 krpm for 18 h at a temperature of 22 °C. Separated samples were fractionated as described above.

2.4.7. Density profile measurements of aqueous iodixanol after NDGU

To sort HiPco samples, we prepared centrifuge tubes with nonlinear, S-shaped gradients designed to have very small variations of density with depth at densities typical of suspended nanotubes. In order to obtain density profiles as a function of depth in the centrifuge tube, we measured optical refractive indices of extracted fractions. A 5 mL centrifuge tube was prepared and run under the specified conditions, but without addition of SWCNTs. After centrifugation, 10 μL fractions were collected starting from the upper meniscus of the solution (5mm from the tube top) at 1 mm intervals using a 10 μL HPLC syringe mounted to a vertical translational stage. The optical refractive index of each collected fraction was then measured using a standard refractometer (WAY Abbe refractometer). A calibration plot relating index of refraction to concentrations of aqueous iodixanol (with 0.7% SC) was constructed (Figs. 2.5 and 2.6). To convert from iodixanol concentrations to mass densities, we performed gravimetric calibrations of 100 μL portions of standard solutions using calibrated micropipettes and a microbalance (CAHN model C-31). These calibration curves relating refractive index to iodixanol concentration and iodixanol concentration to mass density allowed us to determine density profiles in centrifuge tubes before and after NDGU runs. By measuring refractive indices of the DGU layers (before and after centrifugation) and applying the relation between density and refractive index in iodixanol solutions, we precisely mapped the density profile in the

centrifuge tube. In the density profile before ultracentrifugation (Fig. 2.12a) near 25 to 35 mm depth, relatively flatter central sections (density plateau) are obvious.

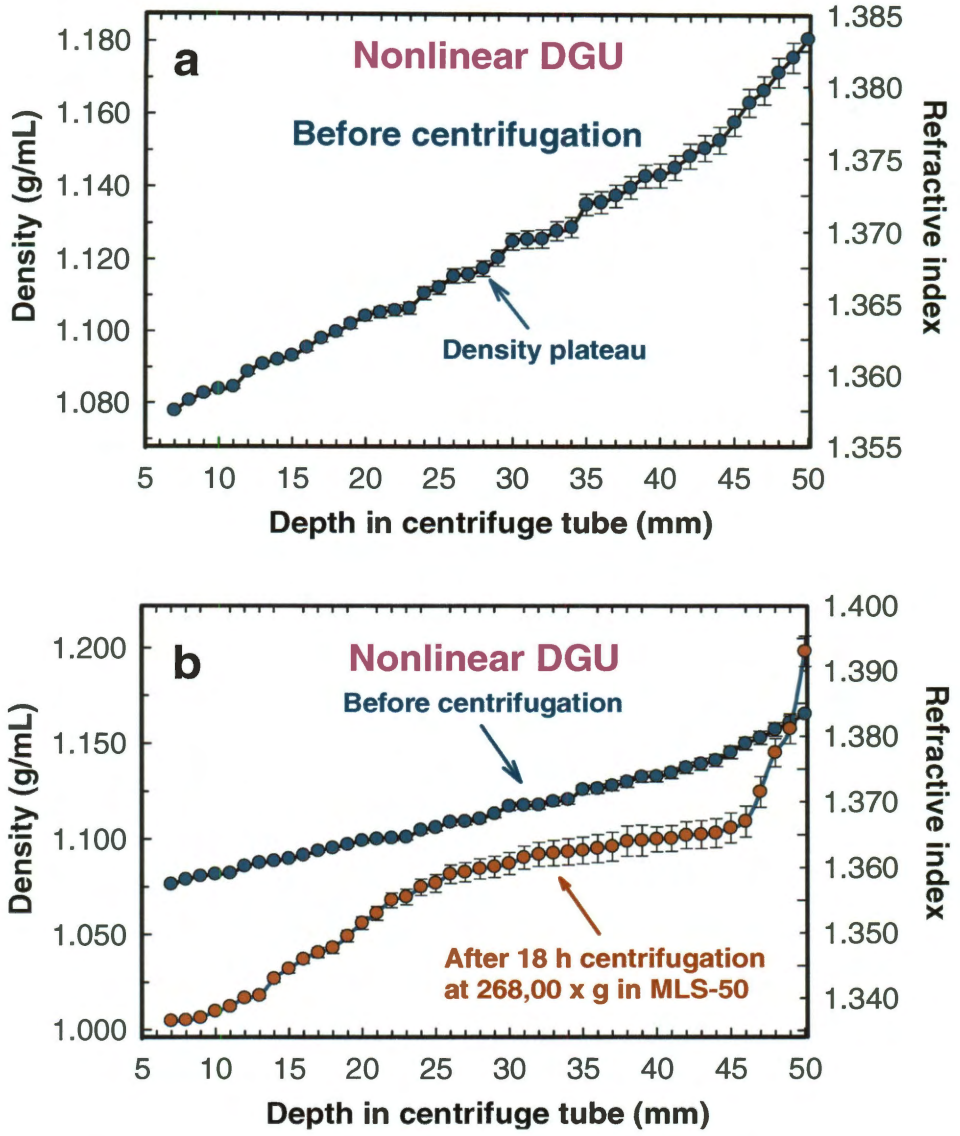

Figure 2.12 Plots of the density profile before and after NDGU. **(a)** Density and refractive index of the medium as a function of depth in centrifuge tube before NDGU. **(b)** Density profile before and after NDGU. The ultracentrifugation was carried out for 18 h at a maximum centripetal acceleration of 268,000 x g (50 krpm) at an ambient temperature of 22 °C. The lower (red) plot shows the nonlinear density profile induced by redistribution of iodixanol inside the centrifuge tube during centrifugation.

The shallow density gradient near 30 mm depth generated in the nonlinear profile after 18 h of centrifugation (Fig. 2.13) is the key to spatially resolving several (*n*,*m*) species having very similar buoyant densities. Two density profile plots show these results for our nonlinear gradient medium and, for comparison, the profile from a conventional linearly prepared gradient. By contrast, those species overlap within a narrow spatial region and are not separable in the steeper density gradient formed after linear preparation.

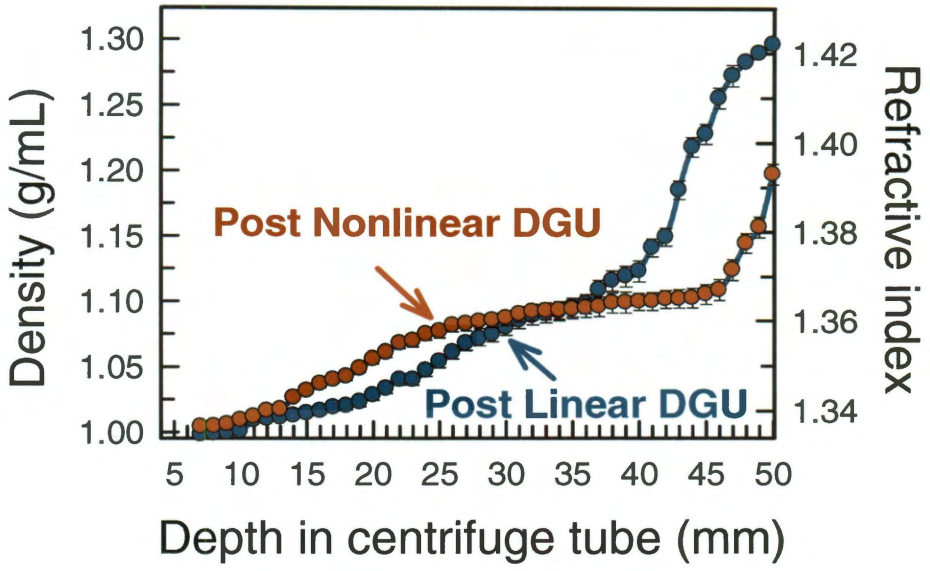

Figure 2.13 Density profiles of the DGU medium (after 18 h of centrifugation at 268,000 x g using an MLS-50 rotor) for linear (blue) and nonlinear (red) initial gradients. Densities were deduced from refractive index measurements.

2.4.8. Experimental buoyant density of SC-suspended SWCNTs

We combine knowledge of the positions and identities of the separated bands with the density profile to deduce effective buoyant densities for different (*n*,*m*) species. This result is shown in Fig. 2.14 as a plot of density vs. nanotube diameter. The buoyant density of SC-suspended nanotubes varies much more steeply for diameters between ~0.7

and 0.8 nm (including species (6,4) to (8,3)) than for diameters between ~0.8 nm and 1.05 nm ((7,5) to (8,7)). The density values shown in Fig. 2.14 agree with previously reported model calculations.[47]

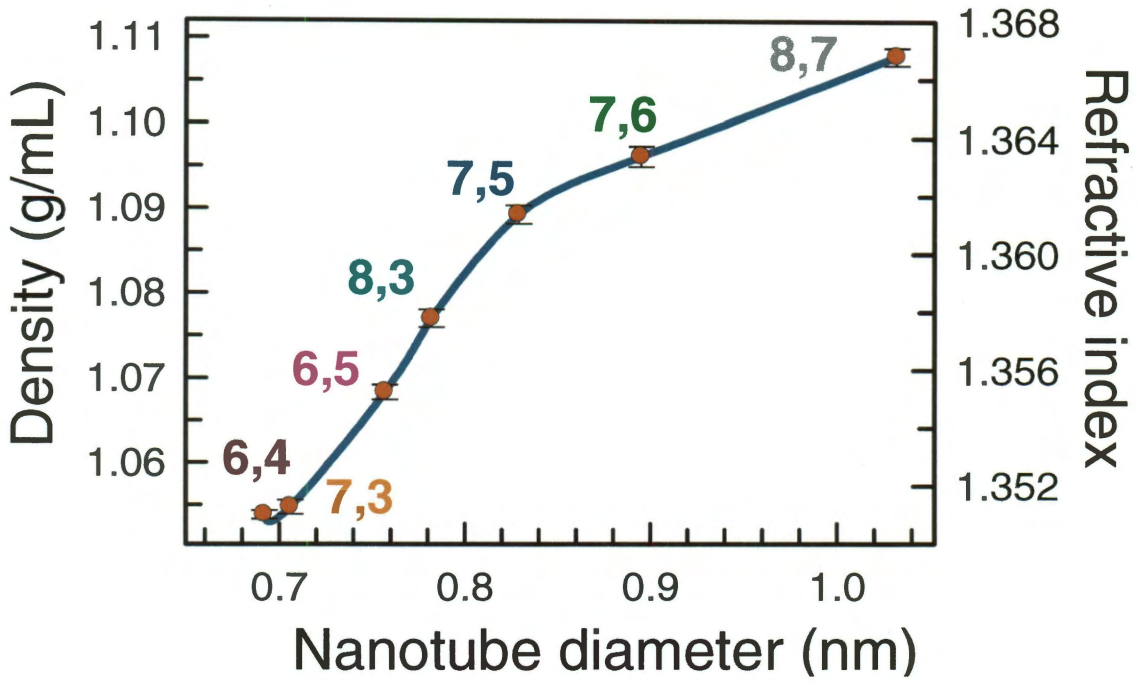

Figure 2.14 Densities of the SC-suspended SWCNT species as a function of SWCNT diameter. The solid line is drawn as a guide to the eye. The SC concentration is 0.7% .

2.4.9. Visual comparison between NDGU and linear DGU sorted centrifuge tubes

Figures 2.15a and b demonstrate results of single surfactant (SC) induced sorting while Figs 2.15c and d show dual-surfactant (SC/SDS) based sorting. The second approach is more effective for the sorting of nanotube enantiomers. Comparing these photographs it is obvious that our new NDGU approach is more effective for the enrichment of different (*n,m*) species. Furthermore, in presence of an anionic surfactant, SDS in the NDGU medium allowed significant enrichment of left- and right-handed enantiomers of (6,5) SWCNT (two identical purple colored bands in Fig. 2.15c).

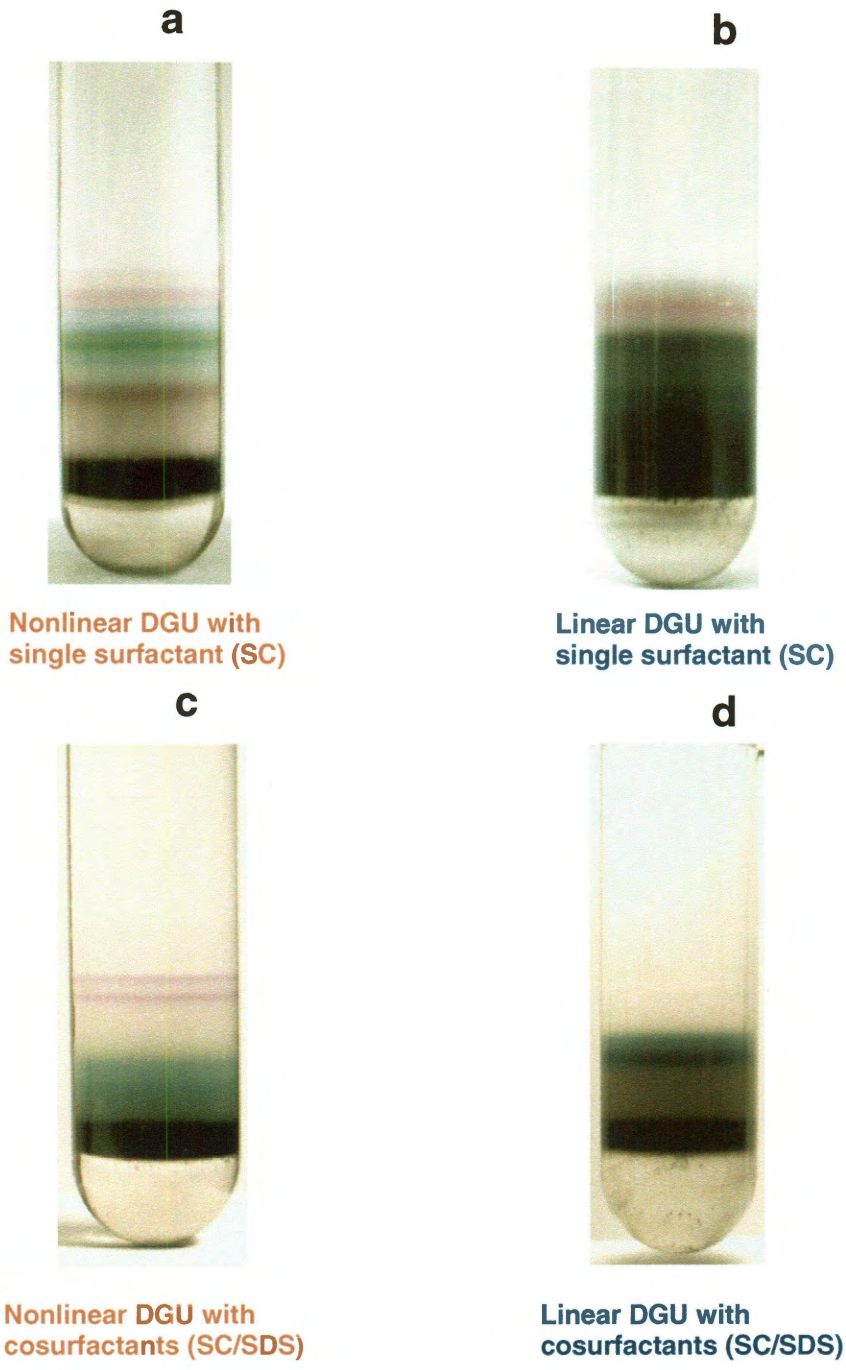

Figure 2.15 Photos of ultracentrifuge tubes sorted by NDGU and linear DGU using HiPco as starting material. **(a)** NDGU utilizing single surfactant (SC). **(b)** Linear DGU with one surfactant (SC) under identical centrifugation conditions. **(c)** NDGU with tuned amounts of SC and SDS to sort (6,5) enantiomers. **(d)** Linear DGU with similar amounts of SC and SDS under identical centrifugation conditions.

2.5. Characterization of sorted SWCNT samples

2.5.1. In situ spectral mapping of a NDGU centrifuge tubes

A key factor in our sorting effort was a new scanning technique introduced by Professor R. Bruce Weisman and Dr. Sergei M. Bachilo, that quickly measured *in situ* fluorescence spectra vs. depth in undisturbed NDGU-processed centrifuge tubes. We obtained spatially resolved fluorescence spectra of the undisturbed contents of NDGU centrifuge tubes using an accessory to the model NS1 NanoSpectralyzer (Applied NanoFluorescence LLC, Houston)[46] that vertically translated the tube in steps of 100-200 μm under computer control. At each vertical position, a sub-millimeter sample region was probed by excitation lasers (at 638, 687, and 783 nm) focused through the centrifuge tube wall. The resulting fluorescence spectra were captured and recorded. By compiling sets of fluorescence spectra as a function of vertical position, we obtained vertical spectral maps that revealed the identities and locations of semiconducting (*n*,*m*) layers in an undisturbed NDGU-processed sample tube. Figure 2.16b illustrates such a vertical spectral map of a centrifuge tube. The (*n*,*m*) composition of each layer in the tube is deduced from the spectral slice at its depth on this map, whereas the spatial distribution of any (*n*,*m*) species is obtained from the vertical profile passing through its spectral peak. Figure 2.16c shows spatial profiles for four species, whose positions of highest concentrations are plotted vs. SWCNT diameter in Fig. 2.16d. The slope of this curve represents the nanotube diameter dispersion. Here, a maximum value of 5.6 mm spatial separation per 0.1 nm diameter difference was attained. Figure 2.16b is even more valuable in quantitatively showing the spatial overlaps between nanotube species.

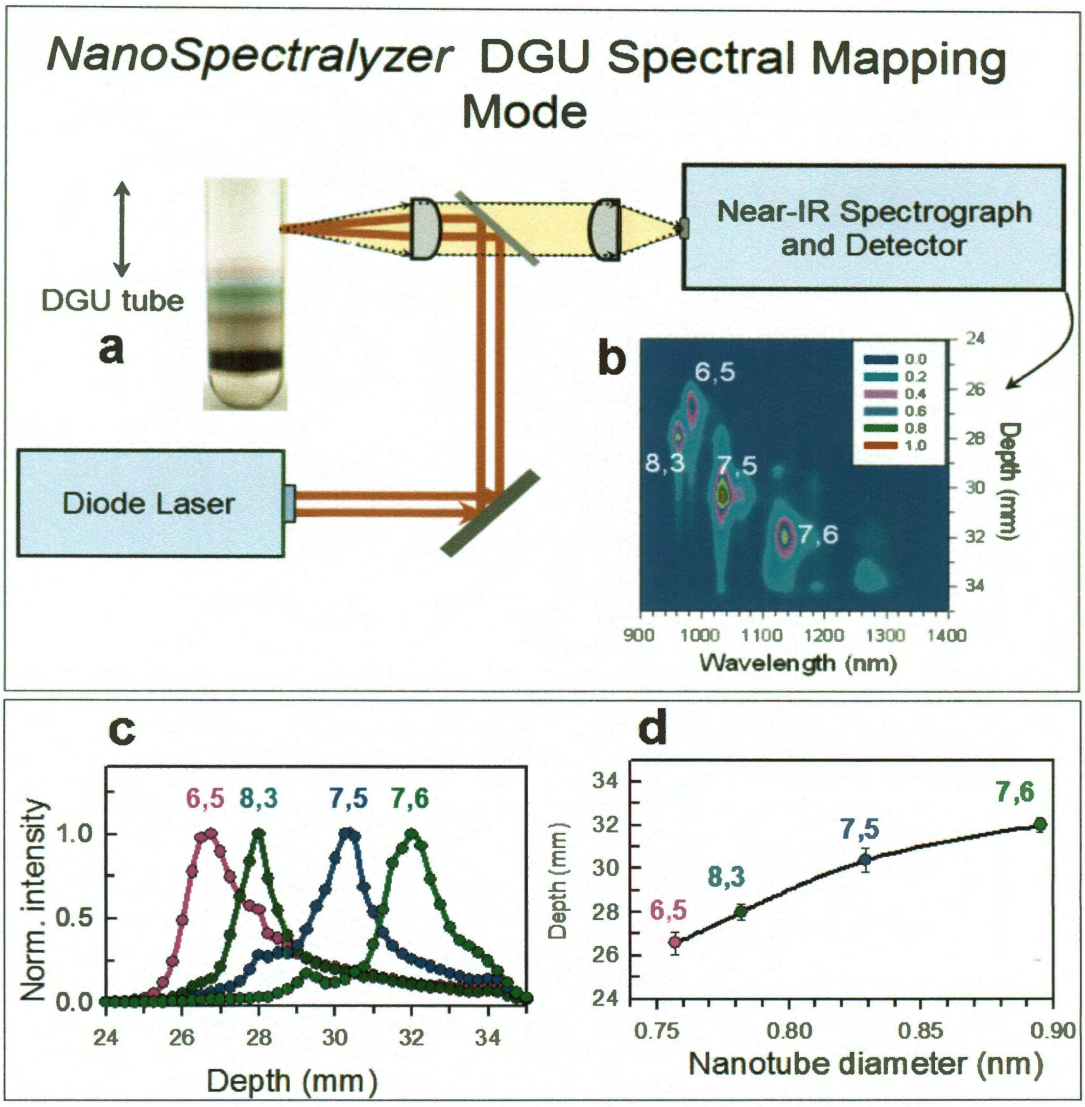

Figure 2.16 *in situ* vertical spectral mapping of a centrifuge tube after NDGU. **(a)** Schematic diagram of the vertical scanning fluorescence spectrometer. The centrifuge tube was vertically translated inside the NS1 instrument to obtain fluorescence and absorption spectra of the undisturbed centrifuge tube. **(b)** The near-IR fluorescence spectra, excited at 638 nm, were collected through the centrifuge tube wall are plotted vs. depth to generate a vertical spectral map. **(c)** Normalized emission intensity as a function of depth for four (*n*,*m*) species. These plots show (*n*,*m*)-resolved concentration profiles inside the centrifuge tube after nonlinear DGU. **(d)** The dependence found for (*n*,*m*) peak concentration position on SWCNT diameter. Larger diameter species appear in higher density regions (lower) in the centrifuge tube.

This detailed feedback about NDGU performance allows one to identify and optimize relevant separation parameters to be identified and optimized.

2.5.2. Photoluminescence spectra of (n,m) sorted SWCNT samples

Near-IR fluorescence emission intensity was measured as a function of excitation and emission wavelengths for unsorted and sorted HiPco samples in aqueous SC.

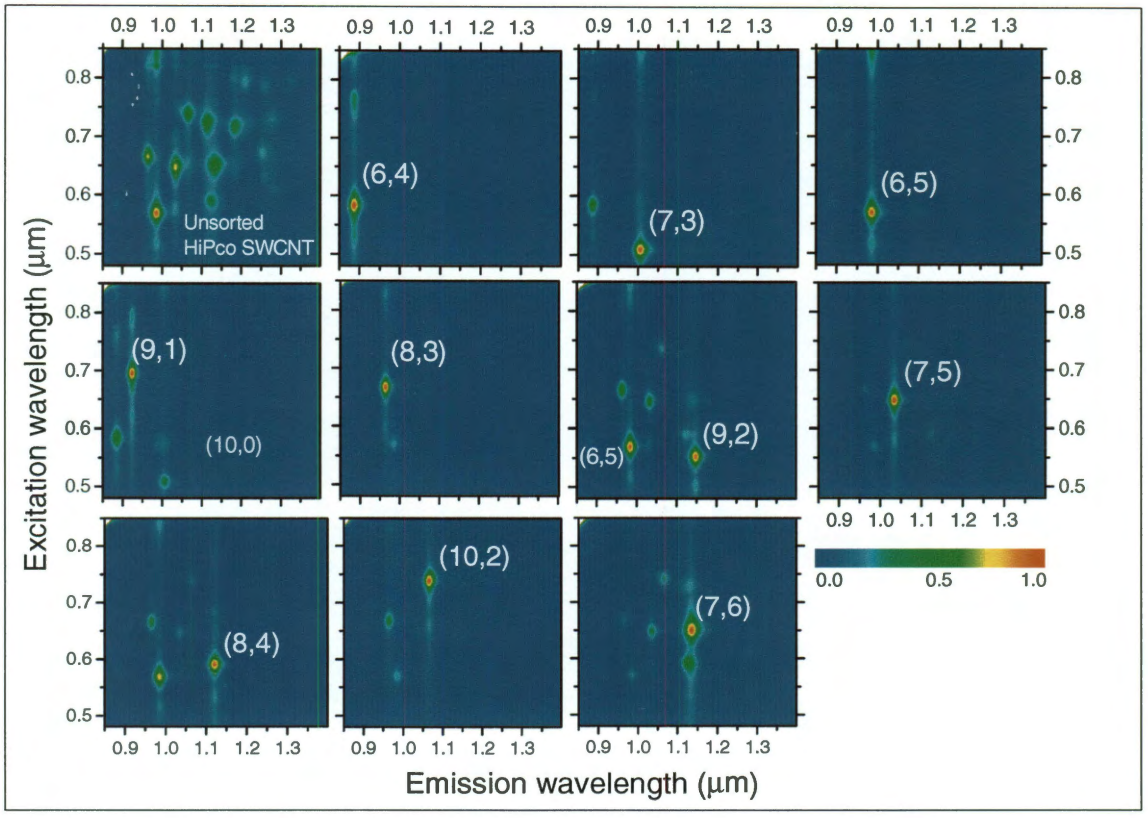

Figure 2.17 Optical characterization of extracted SWCNT fractions by fluorescence spectroscopy. Nanotube photoluminescence emission intensities are plotted as a function of excitation and emission wavelengths.

The instrument used for this study was a Spex Fluorolog 3-21 spectrofluorometer equipped with a liquid nitrogen cooled single-channel InGaAs detector. The excitation wavelength was varied from 480 to 850 nm in 5 nm steps while emission wavelength was

varied from 850 to 1402 nm in 3 nm steps. Both spectral slit widths were 7 nm. Measured intensity was corrected for excitation lamp power and emission system sensitivity. One RG-830 (3 mm) glass filter was used to block scattering from the excitation monochromator. These fluorescence contour plots confirm dramatic enrichment of individual species, which range in diameter from 0.692 to 0.895 nm ((6,4) to (7,6)). The unsorted sample shows numerous semiconducting species whereas each of the 10 sorted fractions shows significant enrichment of an individual semiconducting species. There is even substantial (although incomplete) separation of (6,5) from (9,1), despite their exactly equal diameters.

2.5.3. Optical absorption spectra of (n,m) sorted samples

Optical absorption spectra (Fig. 2.18) were measured in a model NS1 NanoSpectralyzer from 400 to 1400 nm relative to a matched reference containing surfactant solution and iodixanol at the same concentrations. Path lengths were 1.0 cm and the spectral resolution was 1 nm in the visible and 4 nm in the near-IR. Absorption spectra are displayed without background subtraction or vertical offset. Except where noted, there was also no vertical scaling applied. As illustrated in Fig. 2.18, individual species enriched fractions obtained through single-pass NDGU had dramatically reduced absorption backgrounds compared to unsorted SWCNT suspensions. In addition, a close analysis of fluorescence and absorbance data for the ten (*n,m*) sorted samples revealed some important relations. Each (*n,m*)-enriched fraction contained contaminating species with indices (*n+1, m-1*) or (*n-1,m+1*). For example, (7,3) enriched fraction contained some trace of (6,4) species (which is *7-1,3+1*) or (7,5) enriched fraction showed clear evidence of contamination from (8,4) (which is *7+1,5-1*).

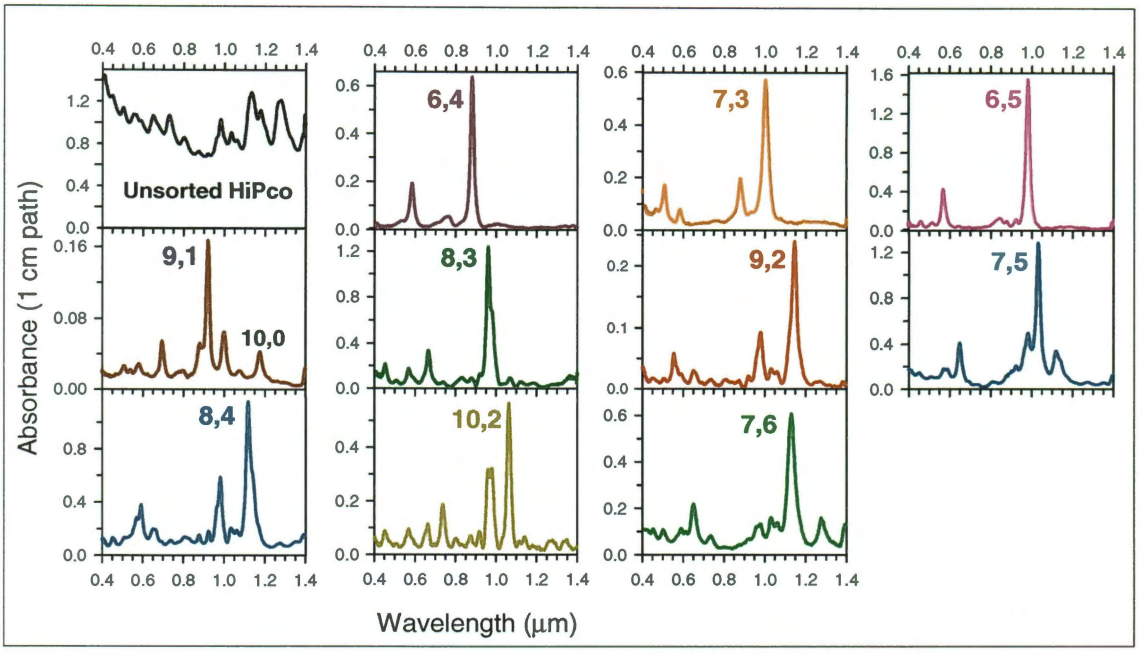

Figure 2.18 Visible/near-IR absorption spectra (1 cm optical path) of the unsorted HiPco sample (diluted 10X) and ten sorted fractions. Each extracted fraction was diluted to 100 μL for absorption measurement. Aqueous solutions of similar iodixanol and SC contents were used as references.

2.5.4. Identification of sorted bands by absorption and fluoresce spectroscopy

A photograph of a centrifuge tube after NDGU showed extensive color banding (Fig. 2.19). Absorption spectra of the separated fractions (Fig. 2.19b) clearly indicate that different (*n*,*m*) species had been sorted into distinct layers. From top to bottom, the bands were identified as (6,4), (7,3), (6,5), (8,3), (7,5), and (7,6). The (6,5) band is purple in color; (8,3) and (7,6) are green; and (7,5) is blue. Additional evidence of effective sorting is displayed in Fig. 2.19c, which shows normalized emission spectra of ten fractions separated from DGU-processed samples containing single or co-surfactants, each excited at the E_{22} transition of its dominant species.

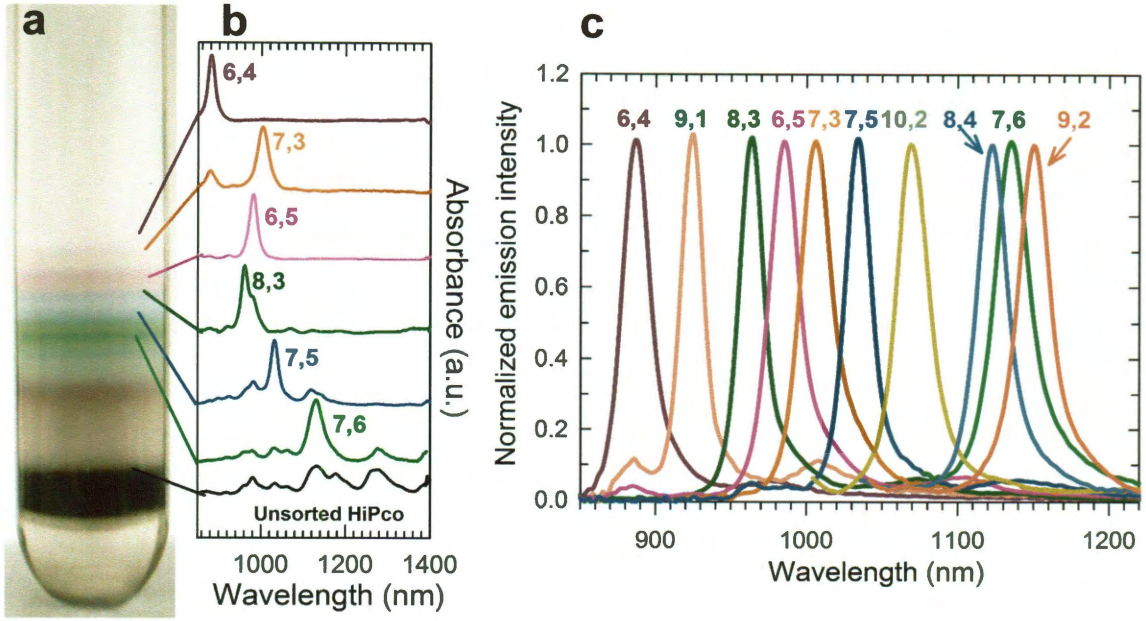

Figure 2.19 (a) Photo of a centrifuge tube containing HiPco SWCNTs sorted by one 18 h NDGU run at 268000 x g (max). Distinct colored bands are layers enriched in different SWCNT species. **(b)** Near-IR absorbance spectra of marked colored layers, labeled with the main (*n*,*m*) component. Spectra are normalized and offset for clarity. The unsorted HiPco spectrum is scaled down by a factor of 10. **(c)** Photoluminescence spectra of ten separated fractions excited at the E_{22} peak of each one's main (*n*,*m*) component.

2.5.5. Results from conventional linear DGU sorting of HiPco SWCNTs

Figure 2.20 shows results of the (*n*,*m*) sorted samples obtained by multiple linear DGU processings. The persistence of multiple SWCNT (*n*,*m*) species was obvious even after the 2nd stage of linear DGU. These results clearly demonstrated the advantage of using single-step NDGU over linear DGU. Firstly, for linear DGU, even after two-step purification (Figs. 2.20b and e) the nanotube sample contained significant cross contamination from other species. Secondly, two cycles of DGU processing took about ~36 h of ultracentrifugation.

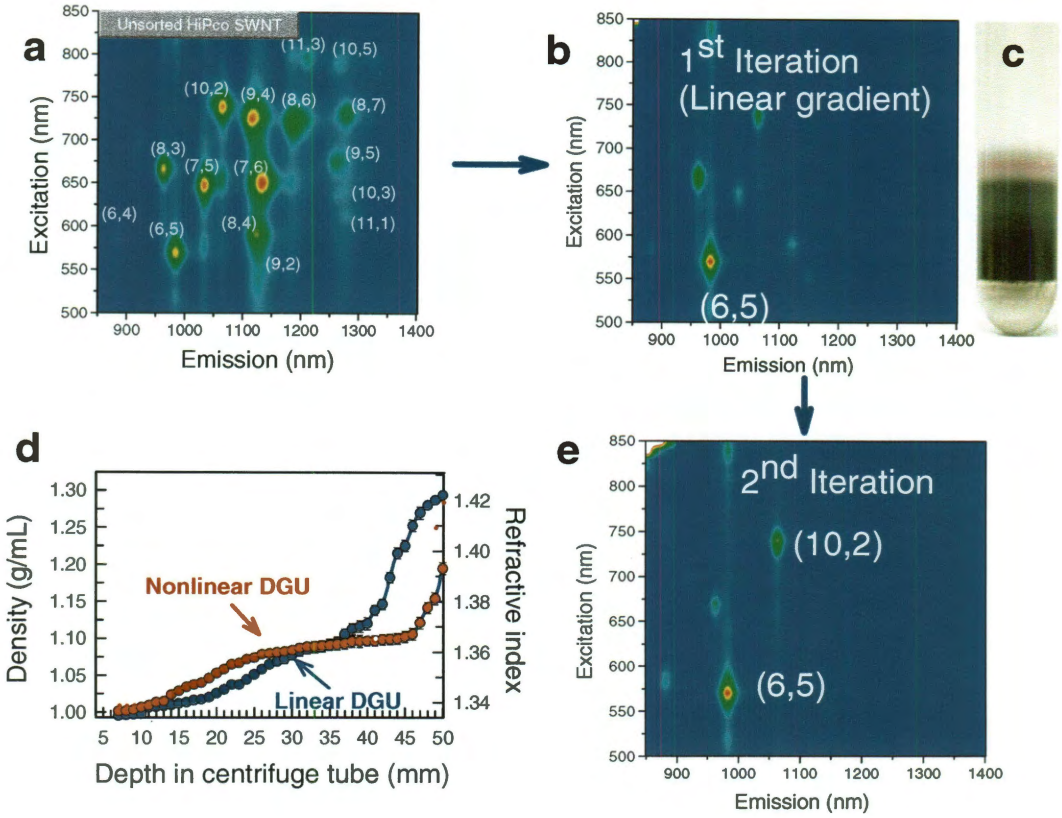

Figure 2.20 Results from conventional linear DGU sorting of HiPco SWCNTs. **(a)** PL excitation-emission map of the unsorted sample dispersed in 2% (w/v) SC solution. **(b)** Equivalent map for the (6,5)-enriched fraction sorted by linear DGU after the 1st iteration. **(c)** Photo of the centrifuge tube after 1st iteration processing. Colored bands are not clearly resolved. **(d)** Comparison between nonlinear and linear DGU density profiles after centrifugation. **(e)** PL excitation-emission map of the (6,5)-enriched fraction sorted by linear DGU after the 2nd iteration.

2.5.6. Generality of the NDGU protocols

In order to demonstrate the generality of our new sorting approach, we carried out NDGU on various batches of as-produced HiPco SWCNTs. Similar results were obtained in each case. However, the intensity of band color varied from HiPco batch to batch depending on the relative (*n,m*) abundance of SWCNTs in the unsorted material.

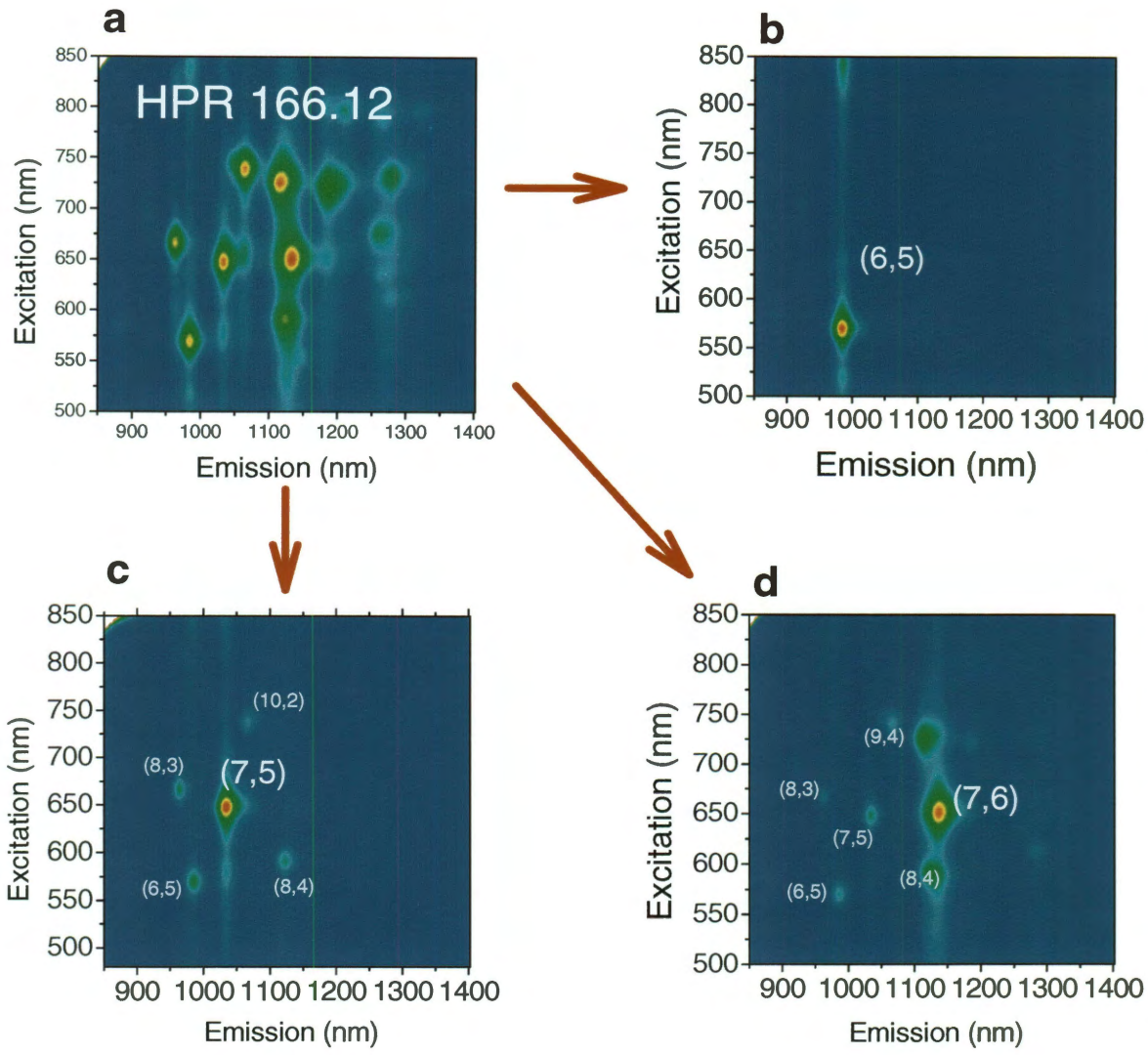

Figure 2.21 Generality of the NDGU protocols: sorting of a different HiPco batch (HPR 166.12). **(a)** Photoluminescence excitation-emission map of the unsorted HPR 166.12 sample dispersed in 2% (w/v) SC solution. **(b)** Equivalent map for (6,5)-enriched fractions after sorting by one-step nonlinear DGU. **(c-d)** Equivalent maps for (7,5)-enriched and (7,6)-enriched fractions after one-step NDGU.

2.5.7. Relative yield calculation of sorted SWCNT samples using peak fit

For the estimating of relative yields of ten different semiconducting SWCNT species in sorted fractions, PeakFit software was used to simulate the near-IR absorption

spectra as sums of Voigt functions representing individual (*n*,*m*) species having peaks between 800 and 1300 nm. The relative yield was determined as the area in the peak representing that species divided by the sum of peak areas for all species in the simulation.

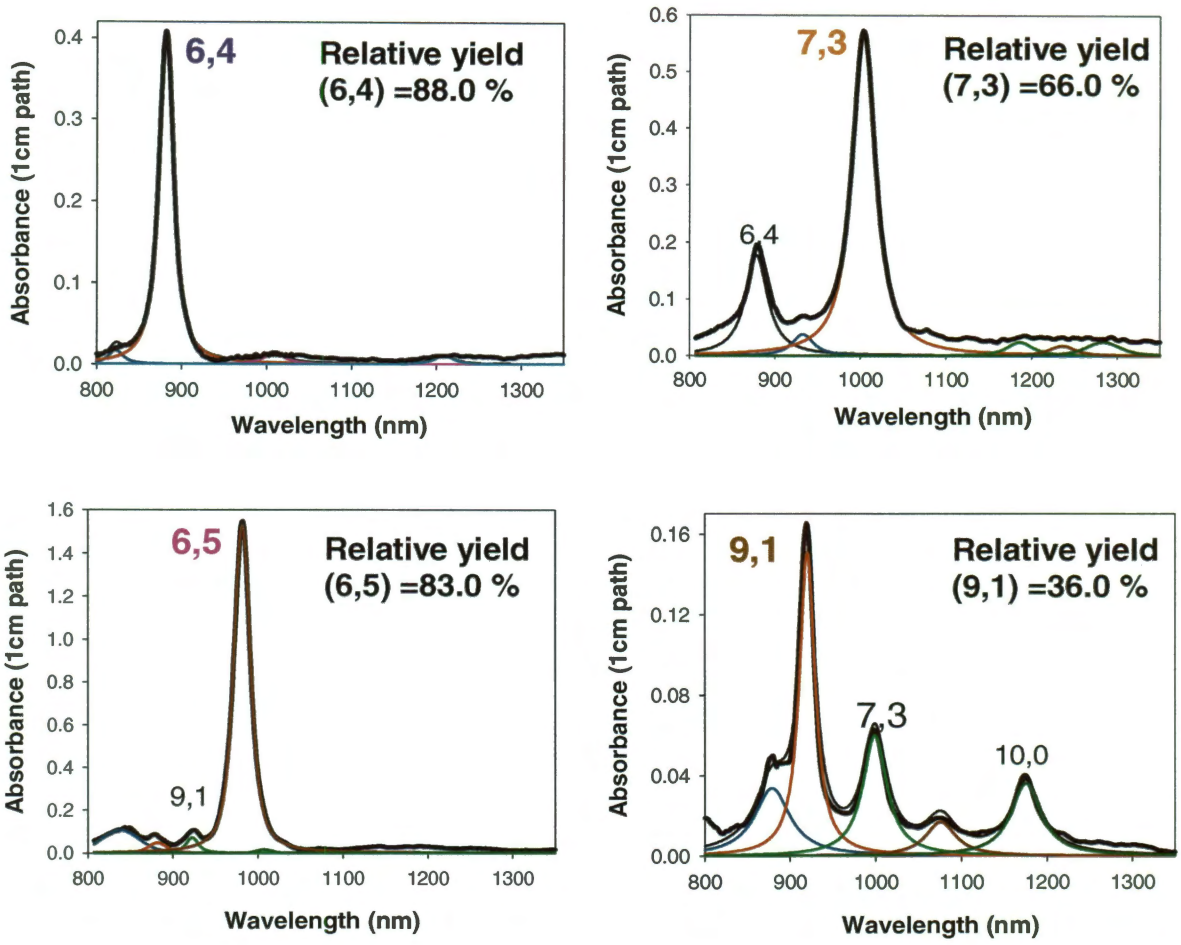

Figure 2.22 Estimation of relative concentration (yield) of sorted HiPco SWCNT species using near-IR absorption spectra and spectral simulations. PeakFit software was used to simulate each spectrum as a sum of Voigt functions representing distinct (*n*,*m*) absorption components.

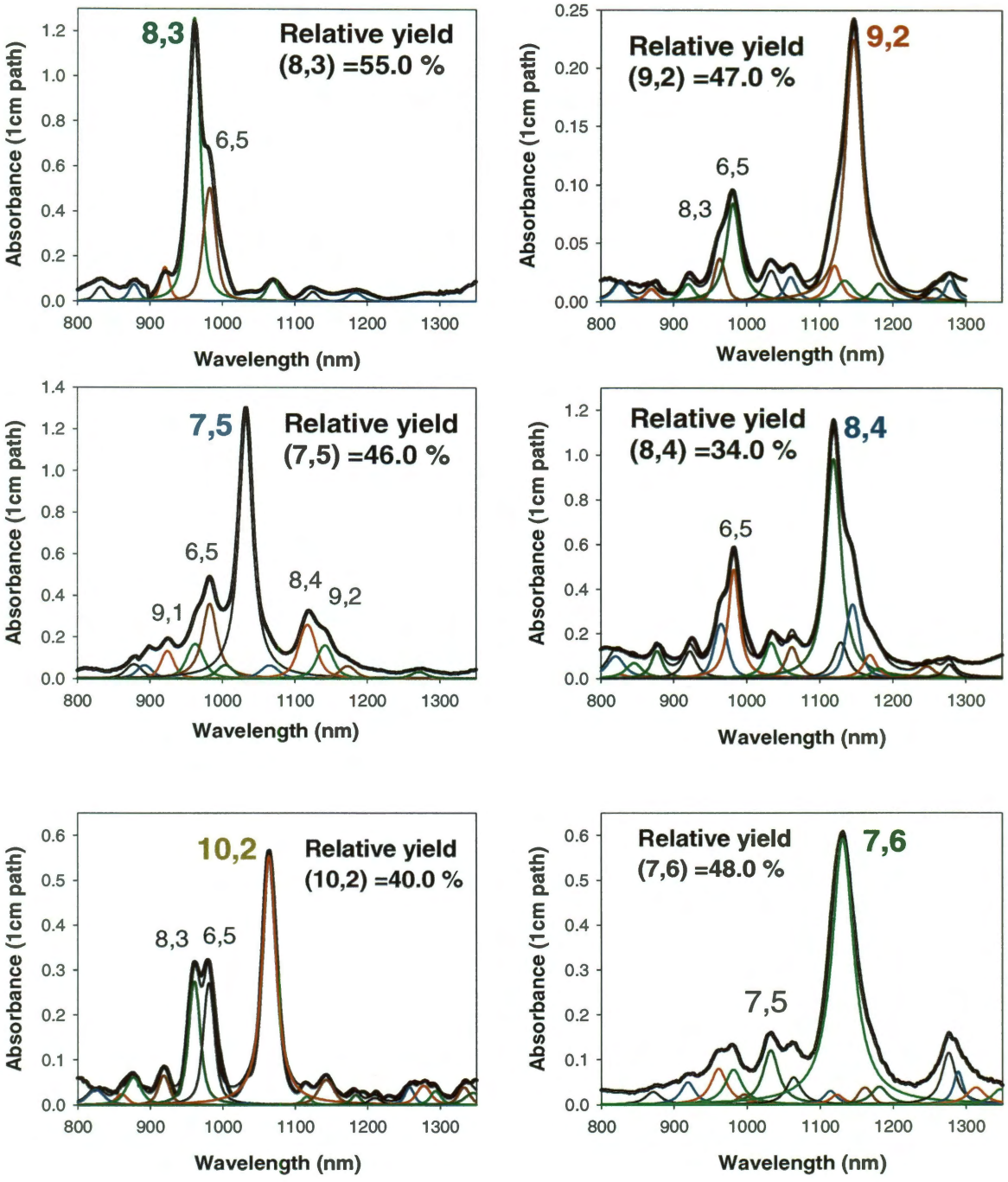

Figure 2.23 Estimation of relative concentration (yield) of sorted HiPco SWCNT species using near-IR absorption spectra and spectral simulations.

A set of near-IR absorption spectra is shown in Figs. 2.22 and 2.23. To estimate the enrichment performance of our nonlinear gradient separation, we fit the near-IR absorption spectra of ten separated fractions shown in Fig. 2.18 by superpositions of Voigt functions centered at the E_{11} peaks of specific (*n*,*m*) species. Assuming equal oscillator strengths for these transitions, and neglecting the possible presence of metallic species, the (*n*,*m*) purity of each fraction was computed as the ratio of the dominant peak's area to the sum of peak areas. This gave purities of 88% for the (6,4) fraction, 66% for (7,3); 83% for (6,5); 36% for (9,1); 55% for (8,3); 47% for (9,2); 46% for (7,5); 34% for (8,4); 40% for (10,2); and 48% for (7,6).

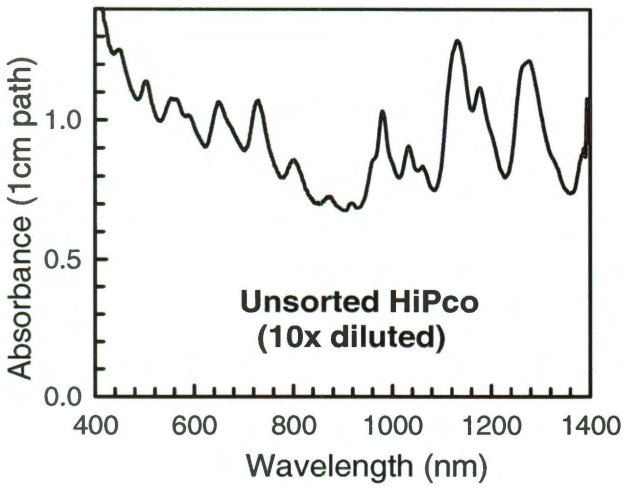

SWCNT (*n*,*m*)	Rel. yield after sorting by single-step NDGU
(6,4)	88.0 %
(7,3)	66.0 %
(6,5)	83.0 %
(9,1)	36.0 %
(8,3)	55.0 %
(9,2)	47.0 %
(7,5)	46.0 %
(8,4)	34.0 %
(10,2)	40.0 %
(7,6)	48.0%

Figure 2.24 Estimation of relative concentration (yield) of sorted HiPco SWCNT species using near-IR absorption spectra and spectral simulations. The graph shows the absorption spectrum of the unsorted sample. The large visible and near-IR backgrounds prevent the use of spectral simulation to deduce a reliable (*n*,*m*) composition of the sample. The table lists the purities of the ten enriched fractions, obtained through NDGU, as the ratio of the concentration of the most abundant (*n*,*m*) species relative to the summed concentrations of all semiconducting (*n*,*m*) species in that fraction (assuming equal E_{11} molar absorptivities).

These (*n*,*m*) purities are lower than the samples recently obtained by Zheng and co-workers using ion exchange chromatography and customized ssDNA oligonucleotides.[21] Nevertheless, relative abundances of the enriched species are much greater in the NDGU-processed fractions than in the unsorted HiPco sample, and NDGU based purification process costs much lower than IEX. Figure 2.25 draws a conclusive picture of our overall success in sorting various (*n*,*m*) species from raw HiPco SWCNTs using NDGU. Green hexagons represent species which are already sorted while red hexagons highlight tubes that could be partially enriched by single or multi-step NDGU in future.

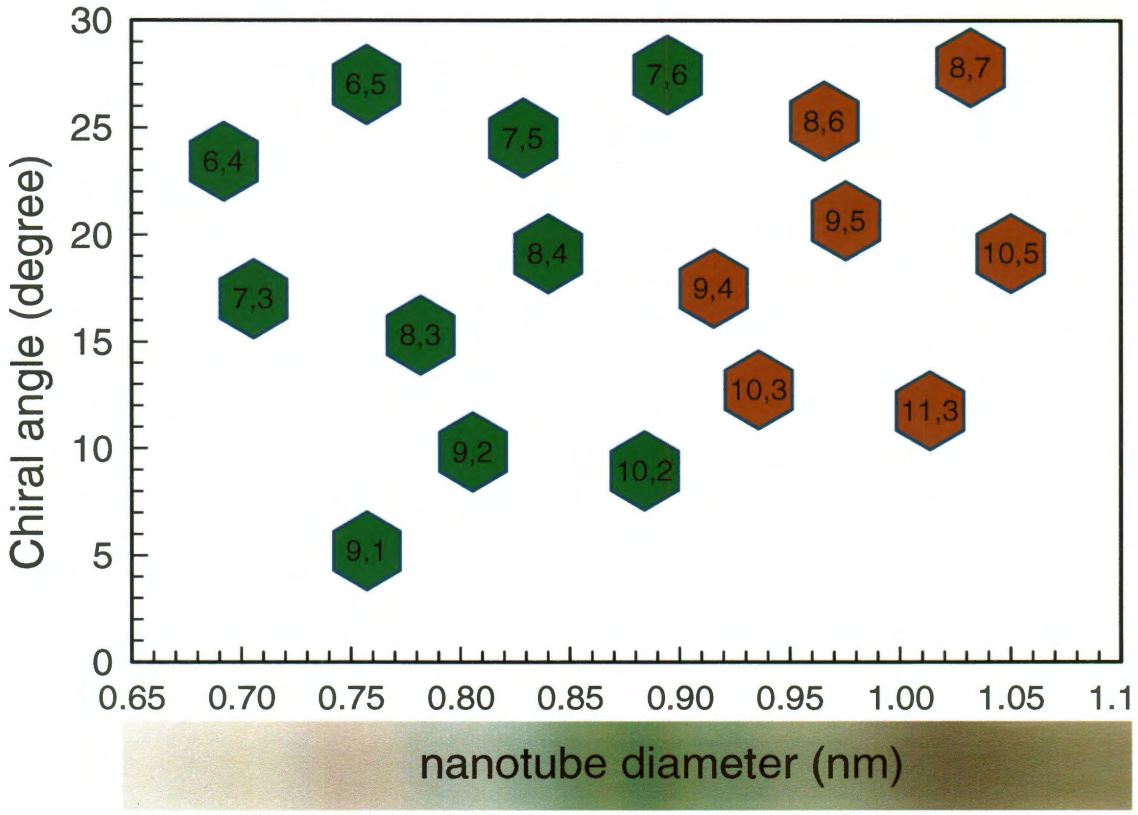

Figure 2.25 The distribution of (*n*,*m*)s sorted (green hexagons) and likely to be sorted (red hexagons) by NDGU from unsorted HiPco SWCNTs.

2.5.8. Raman spectroscopy of (n,m) sorted samples

Additional evidence of effective sorting is provided by Raman spectra, as measured using a 633 nm excitation laser (Figs. 2.26 and 2.27). The dominant radial breathing mode peak from each fraction arises from same (*n*,*m*) species that dominates the absorption and fluorescence spectra. However, strong resonance selection effects make Raman less suitable than absorption or emission spectroscopy for assessing the purity of fractions. The very low relative intensities of Raman D bands (near 1300 cm^{-1}) suggests minimal derivatization or defects in these DGU-sorted nanotubes.

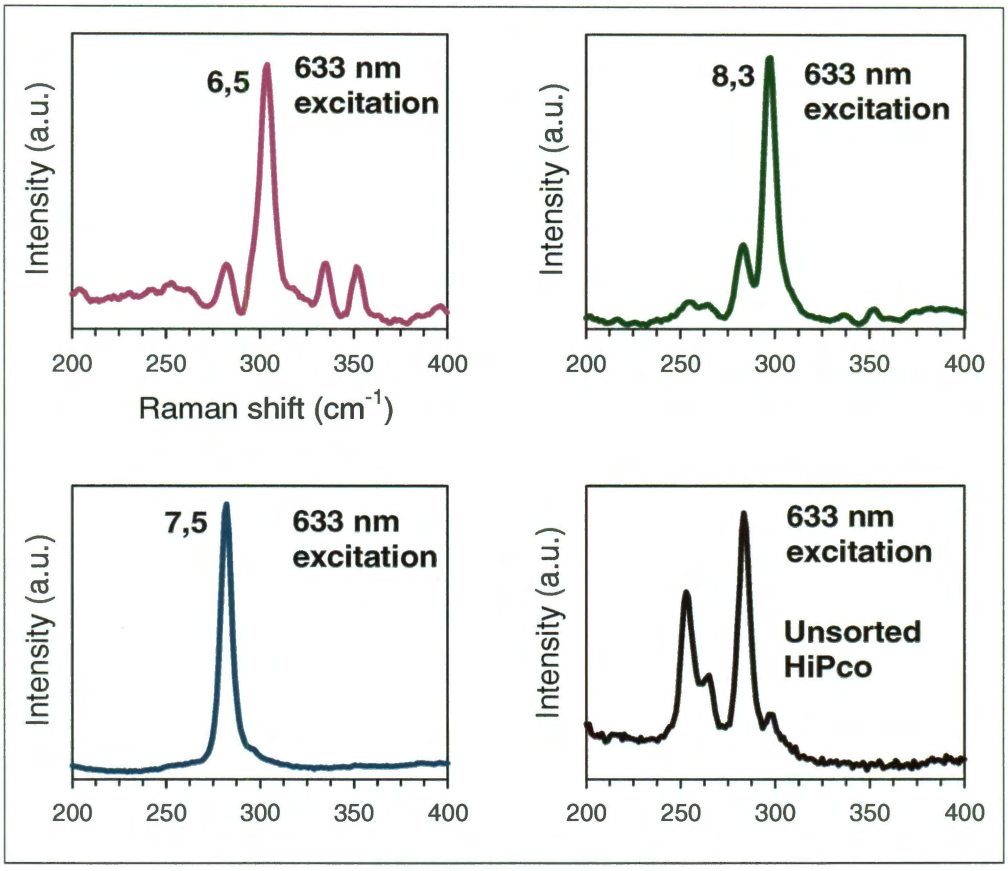

Figure 2.26 Radial breathing mode (RBM) spectra of the sorted and unsorted sample. Scaled spectral data are shown for the unsorted HiPco sample and for sorted fractions enriched in the (6,5), (8,3), and (7,5) species. All spectra were measured with 633 nm excitation.

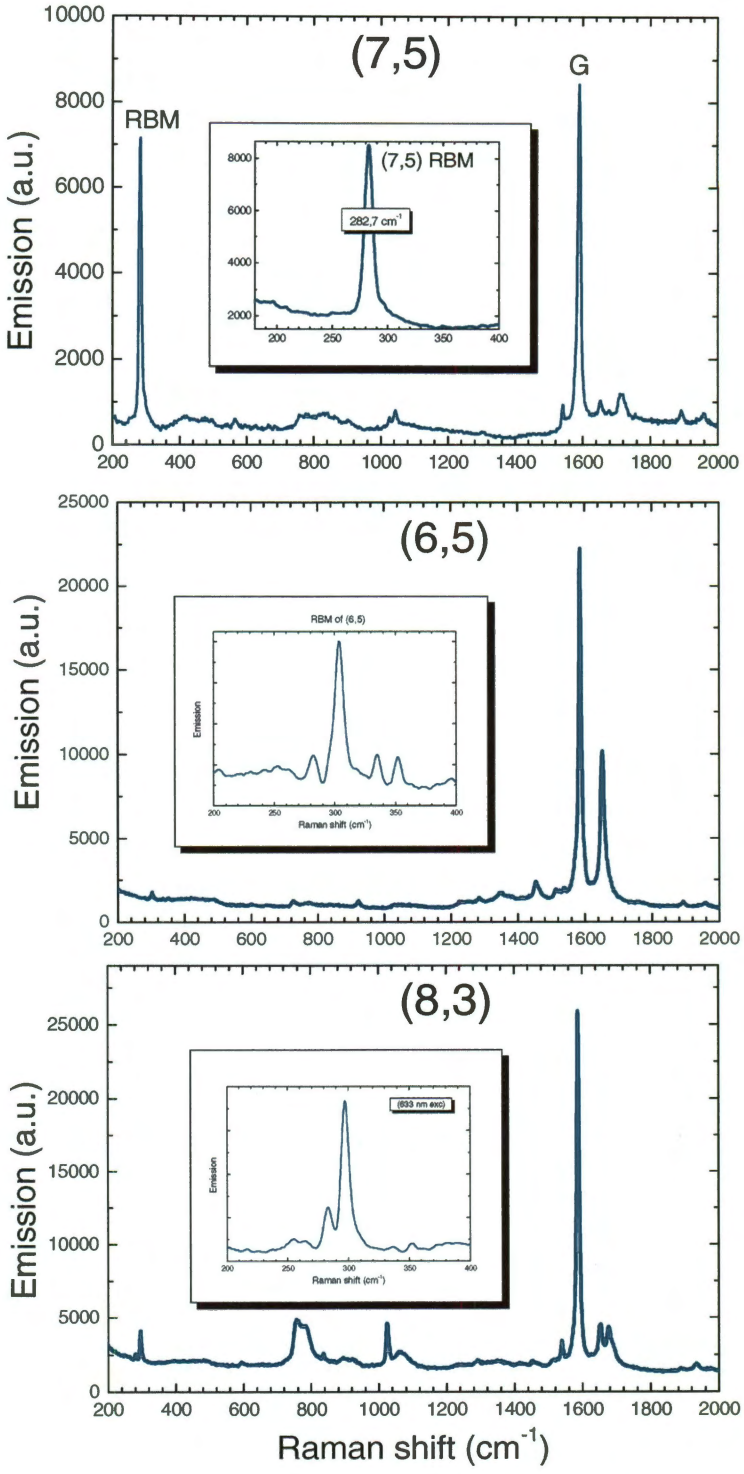

Figure 2.27 Wider-range Raman spectra of three sorted SWCNT enriched fractions. All spectra were measured with 633 nm excitation.

2.5.9. Demonstration of intactness of NDGU sorted SWCNTs by near-IR microscopy

Near-IR fluorescence microscopy can be a valuable tool to investigate the intactness of NDGU sorted samples. Figure 2.28 shows a set of spectroscopic results for individual sorted SWCNTs. The instrumentation details for near-IR microscopy are discussed in chapter 3. These results suggest that the sorted nanotubes do not lose any intrinsic photophysical property. Emission spectra from bulk samples and single tube display similar profiles.

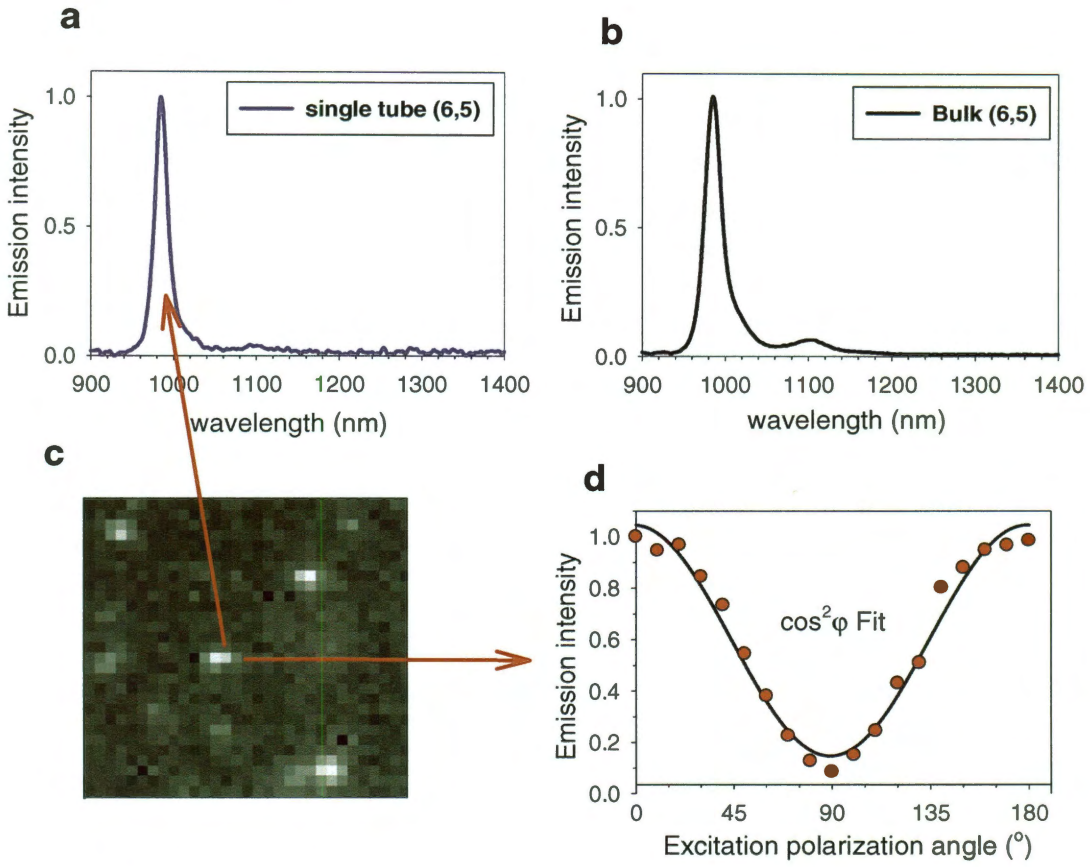

Figure 2.28 Demonstration of intactness of NDGU sorted SWCNTs through single tube and bulk near-IR fluorescence study. (**a**) PL emission from a single (6,5) tube excited by a 785 nm diode laser. (**b**) PL emission from bulk (6,5) with 570 nm excitation. (**c**) Bright pixels represent single tube fluorescence images of (6,5) tubes. (**d**) Emission intensity of a single (6,5) tube is drawn as a function of polarization angle of the excitation beam.

2.6. Enantiomeric separations of SWCNTs by NDGU using co-surfactants

As reported by Hersam and co-workers,[48] DGU can separate right- from left-handed enantiomeric forms of individual (*n,m*) species. We have significantly improved enantiomeric sorting by applying NDGU gradients and mixed surfactants.

2.6.1. Sorting of (6,5) enantiomers

By adding an anionic co-surfactant to SC in our NDGU method, we achieved effective and highly reproducible single-step enantiomeric sorting of several (*n,m*) species abundant in HiPco samples. We found optimal enantiomer separation with a surfactant mixture of 0.7% SC plus 0.175% SDS in a slight variant of the nonlinear gradient described earlier (see table 2.3 for detailed protocols). Ultracentrifugation gave two distinct purple bands near the top of the colored layers in the tube, as illustrated in Fig. 2.29b. In addition, Fig. 2.29a shows the *in situ* spatial fluorescence map of this section of the tube. Both bands are identified as (6,5) SWCNTs. The 984 nm intensity profile as plotted on the right edge of Fig. 2.29a shows that the two emission peaks are spatially separated by ~2 mm. Remarkably, the absorption spectra of the separated (6,5) fractions are distinguishable from each other, as shown by the *in situ* data of Fig. 2.29c. The upper (6,5) fraction's band is red-shifted by ~4 nm from the lower fraction's, and also slightly narrower. These spectral differences reflect inequivalent local environments for the two (6,5) populations resulting from compositional differences of their surfactant coatings. If the two (6,5) populations are enantiomers, then they must show circular dichroism (CD) signals of opposite sign at appropriate transition wavelengths. This is confirmed by CD spectra of the separated fractions (Fig. 2.29d).

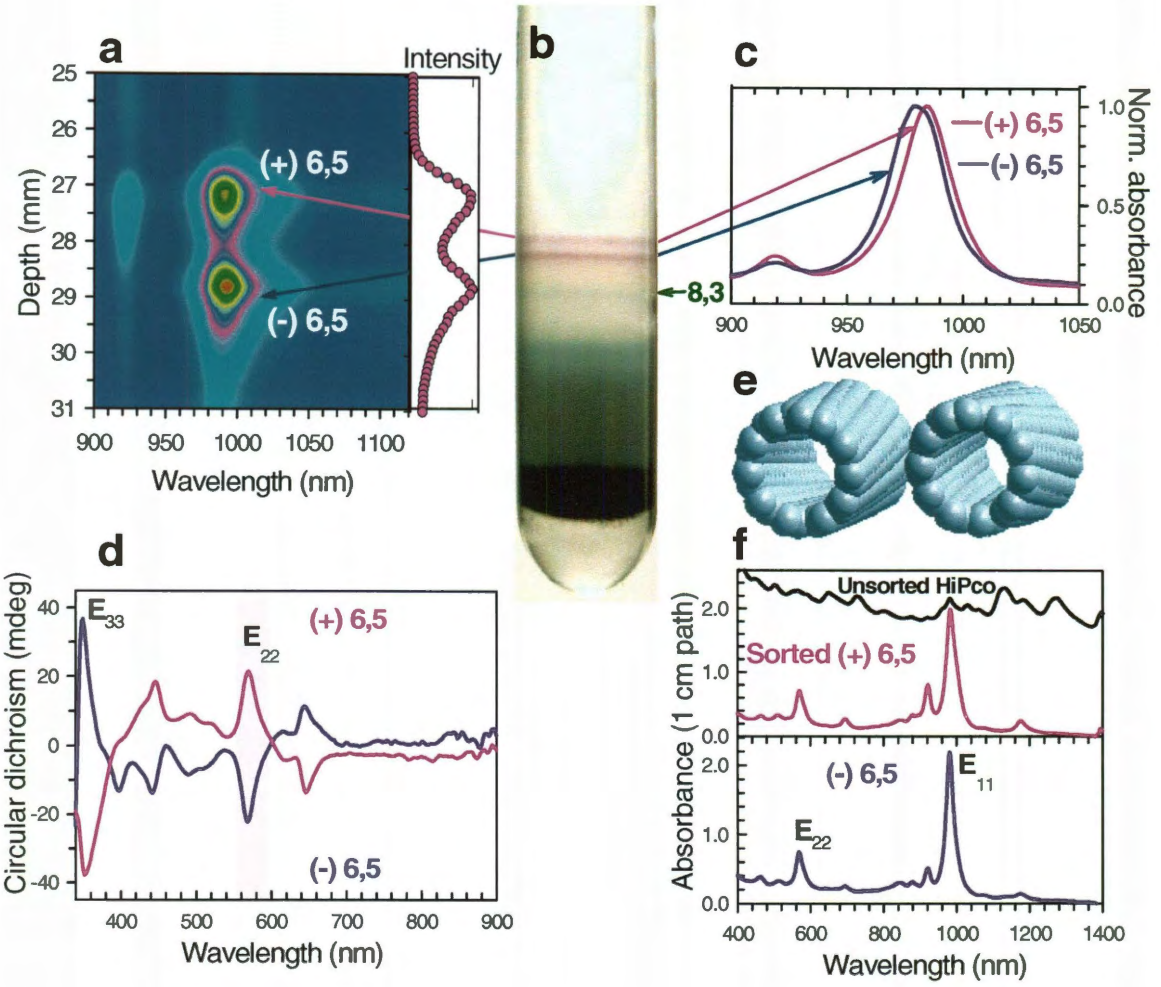

Figure 2.29 NDGU separation of optically active enantiomers of (6,5). **(a)** Vertical fluorescence spectral map (with 783 nm excitation) showing spatially resolved (6,5) enantiomers. The trace on the right edge shows intensity at 984 nm. **(b)** Photo of the corresponding centrifuge tube with distinct (6,5) enantiomer bands. **(c)** *In situ* near-IR absorbance spectra of the two bands showing a red shift of the upper one. **(d)** CD spectra of the separated (6,5) enantiomer fractions. Peaks corresponding to E_{22} and E_{33} transitions are labeled. The reference sample contained an aqueous solution with similar surfactant and iodixanol contents. **(e)** Models of the two (6,5) enantiomeric structures. **(f)** Unscaled optical absorbance spectra (1 cm optical path) of the two (6,5) enantiomeric fractions and the unsorted sample (after 5X dilution).

The CD spectra of enantiomer separated samples were measured using a Jasco model J-815 circular dichroism spectrometer equipped with a visible detector covering 200 to 900 nm. Our CD spectra were typically measured from 340 to 800 nm in 2 nm steps with 4 scans averaged.

Although our CD spectrometer cannot probe the near-IR (6,5) E_{11} transition, it reveals strong and convincing opposite-signed CD peaks at the E_{22} and E_{33} transitions (570 and 348 nm; see Fig. 2.30). Throughout our study, we will label the isomers as (+) or (-) according to whether their CD signals at the E_{22} peak are positive or negative. As a control, we found no optical activity in SC suspensions of unsorted HiPco SWCNTs, which should contain a racemic mixture of the enantiomers. Fig. 2.29f shows the absorption spectra of the (6,5) fractions used for CD spectroscopy and the spectrum of the sample before NDGU processing. These demonstrate that the (6,5) enantiomeric fractions are also highly (*n*,*m*) purified.

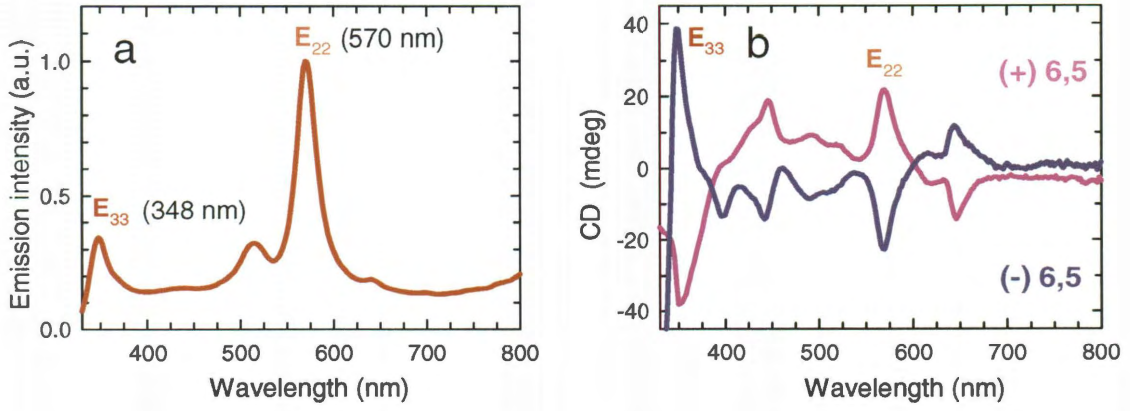

Figure 2.30 Photoluminescence excitation and CD spectra of enantiomer-sorted (6,5)-enriched fractions. **(a)** PL excitation spectrum, with detection at 984 nm. **(b)** CD spectra of optically-active left- and right-handed (6,5) enantiomer fractions. The strong peaks visible at 348 and 570 nm correspond to the E_{33} and E_{22} parallel-polarized optical transitions of (6,5). These two features are seen in both the PL excitation and CD spectra.

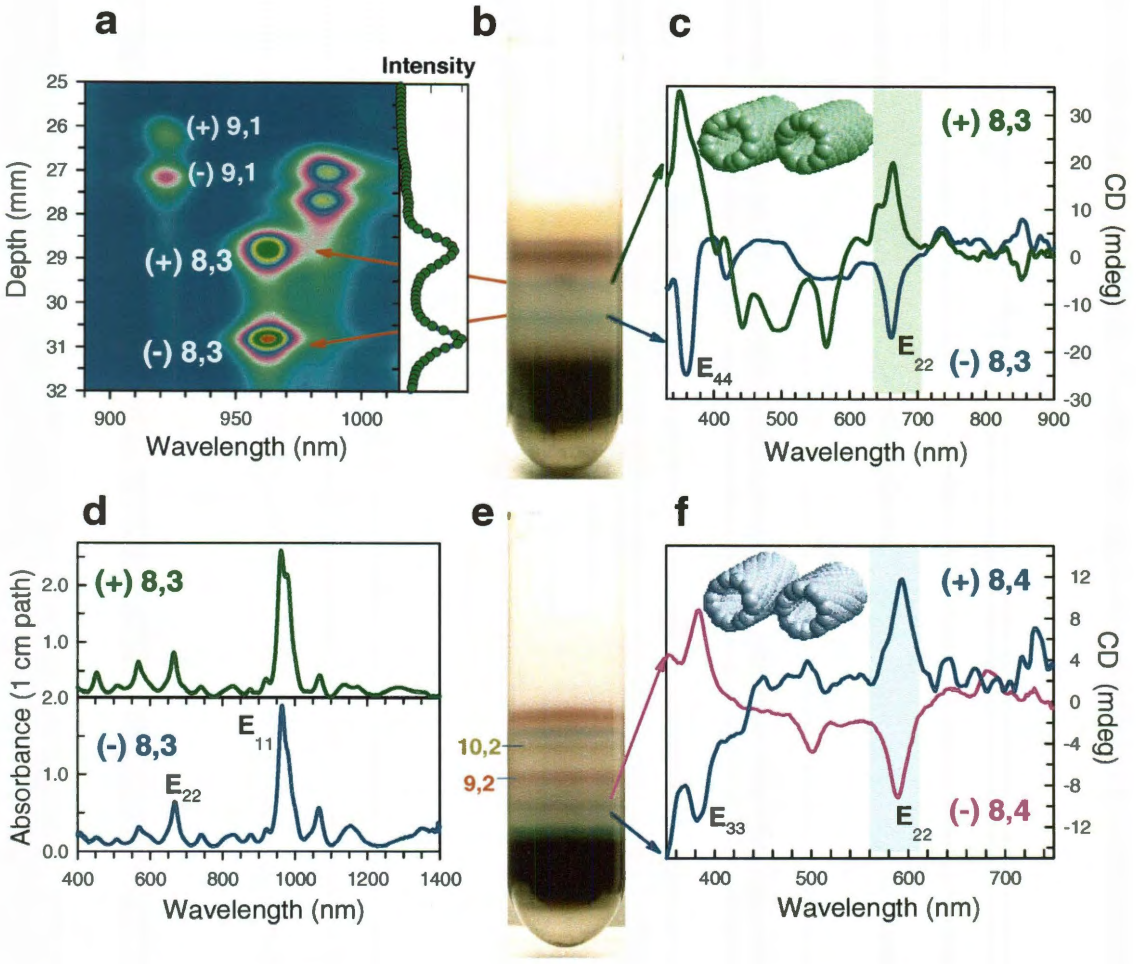

Figure 2.31 NDGU separation of optically active enantiomers of (8,3) and (8,4). **(a)** Vertical fluorescence spectral map (excited at 687 nm) showing spatially resolved (8,3) and (9,1) enantiomers. **(b)** Photo of the corresponding centrifuge tube with distinct (8,3) enantiomer bands (green). **(c)** CD spectra of the separated (8,3) enantiomer fractions. Peaks corresponding to E_{22} and E_{44} transitions are labeled. The reference sample contained an aqueous solution with similar surfactant and iodixanol contents. Models of the two (8,3) enantiomeric structures are shown as an inset. **(d)** Unscaled optical absorbance spectra (1 cm optical path) of the two (8,3) enantiomer-enriched fractions. **(e)** Photo of a centrifuge tube with partially resolved (8,4) enantiomer bands. **(f)** CD spectra of the separated (8,4) enantiomer-enriched fractions. Peaks corresponding to E_{22} and E_{33} transitions are labeled. Models of the two (8,4) enantiomeric structures are shown as an inset.

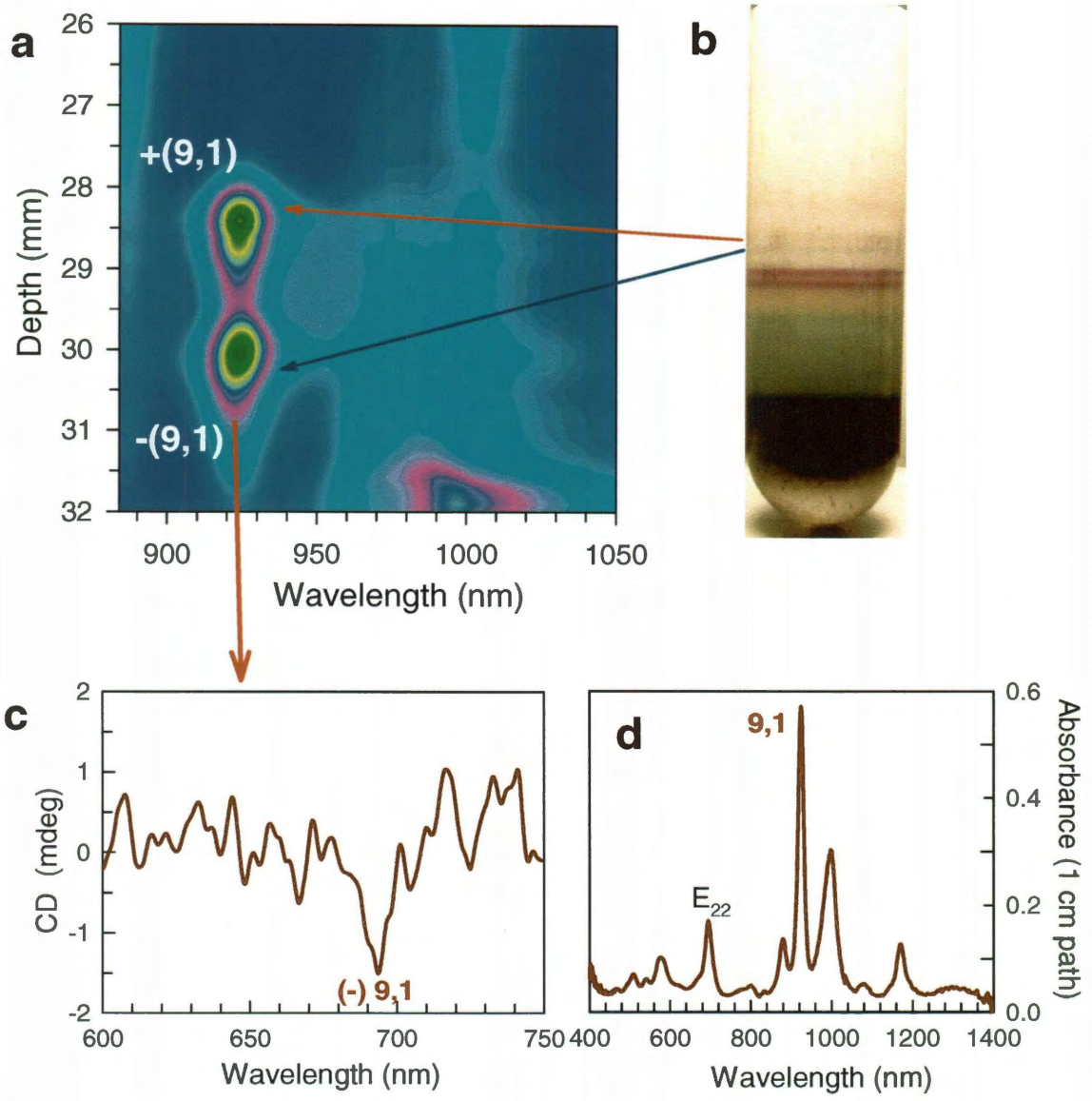

Figure 2.32 Resolved (9,1) enantiomers. **(a)** Vertical fluorescence spectral map (excited at 687 nm) of a segment of a NDGU-processed centrifuge tube, showing layers with resolved (9,1) enantiomers. **(b)** Photo of the DGU tube mapped in frame a, with the two light green-grey bands enriched in (9,1) enantiomers marked. **(c-d)** Circular dichroism (CD) and absorption spectra of the lower (-) (9,1) fraction. A weak but distinct E_{22} transition of (9,1) is seen in the CD spectrum, which was measured against an aqueous reference solution with matched surfactant and iodixanol contents.

2.6.2. Sorting of (8,3), (9,1), and (8,4) enantiomers

Comparable enantiomeric separation was also achieved for (8,3) and (9,1) SWCNTs using a slightly adjusted nonlinear density gradient profile. This separation is illustrated by well resolved bands in the fluorescence map and tube image (Figs. 2.31a and 2.31b). CD spectra of the separated (8,3) fractions display strong, opposite-signed peaks at 667 and 355 nm (Fig. 2.31c), identified as the E_{22} and E_{44} transitions in this surfactant. Absorption spectra of these fractions reveal minor contamination from (6,5), particularly for the upper (+)(8,3) fraction. The negative-going 567 nm CD peak of this fraction indicates that the cross-contamination is from the enantiomerically enriched lower (-) band of (6,5). Enantiomers of (8,4) were not as cleanly separated by our NDGU method, but it was still possible to obtain fractions with significant enrichment. Fig. 2.31e shows a photo of a DGU tube from which the fractions marked by red and blue arrows were extracted. The opposing CD peaks at 592 nm (E_{22}) and 384 nm (E_{33}) confirm enantiomeric enrichment of (8,4) (Fig. 2.31f).

2.6.3. Sorting of (7,3), and (6,4) enantiomers

Further minor modifications of the DGU protocol allowed enantiomeric separation of additional species. Figure 2.33 shows the tube image, fluorescence spectral map, CD spectra, and absorption spectra of (7,3) and (6,4) fractions. Enantiomeric separation of (7,3) and (6,4) was performed using the DGU parameters listed in the last column of Table 2.3. Figures 2.33a and b show the fluorescence spectral map and tube image obtained after such a DGU run. As was found for (6,5) enantiomers, the two separated (7,3) fractions give slightly different absorption spectra (Fig. 2.33c). The (7,3) E_{11} peak for the upper, (+), fraction is slightly narrower and red-shifted by 3 nm in

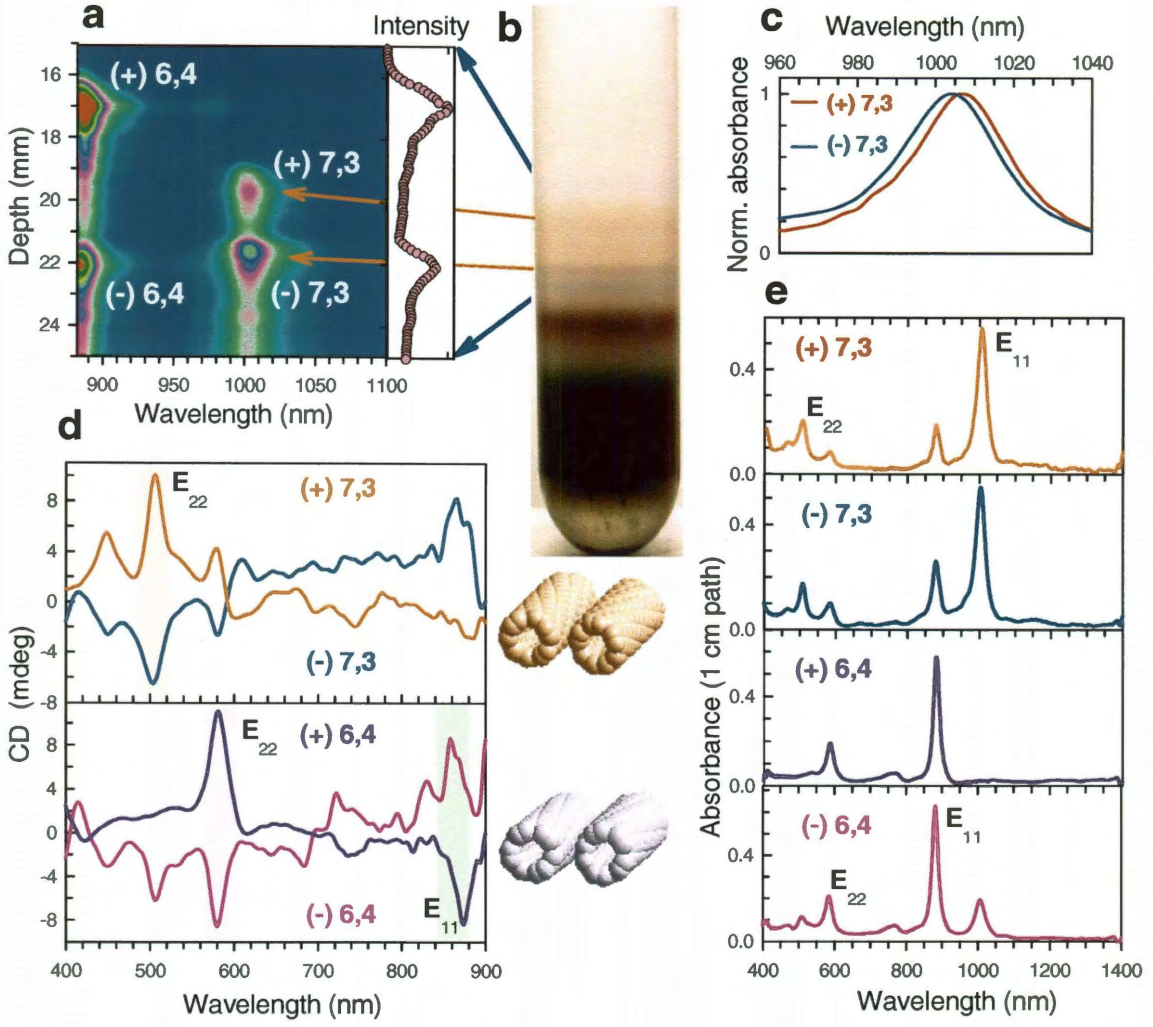

Figure 2.33 NDGU separation of optically active enantiomers of (6,4) and (7,3). **(a)** Vertical fluorescence spectral map (excited at 783 nm) showing spatially resolved (6,4) and (7,3) enantiomers. **(b)** Photo of the corresponding centrifuge tube. **(c)** Normalized near-IR absorbance spectra of the two (7,3) separated fractions showing a red shift of the upper one. **(d)** CD spectra of the pairs of separated (7,3) and (6,4) enantiomeric fractions. Peaks corresponding to all E_{22} transitions and E_{11} transitions of (6,4) are labeled. The reference sample contained an aqueous solution with similar surfactant and iodixanol contents. Models of the two pairs of enantiomeric structures are shown between frames **d** and **e**. **(e)** Unscaled optical absorbance spectra (1 cm optical path) of the two pairs of enantiomeric fractions.

absorption and 6 nm in emission. CD spectra of the separated fractions reveal peaks of opposite signs at the E_{22} peak of (7,3) near 505 nm (Fig. 2.33d, upper frame). The E_{33} CD transitions were inaccessible in this case because of overlap with strong surfactant absorptions. The same NDGU run provided two enantiomeric fractions of (6,4) SWCNTs at the locations shown in the fluorescence map (Fig. 2.33a).

The E_{11} transition of (6,4) lies at short enough wavelength that both E_{22} and E_{11} peaks are clearly seen in the CD spectra of these fractions (Fig 2.33d, lower frame). The upper (6,4) fraction gives a positive CD signal at its 582 nm E_{22} peak, while the lower fraction gives a negative signal. The signs of these signals are reversed for the 875 nm E_{11} transitions. The fluorescence map of Fig. 2.33a shows significant spatial overlap between (6,4) and (7,3) concentrations in the DGU tube (especially for the lower spots), suggesting the likelihood of cross-contamination in these separated fractions. This is confirmed by the presence of secondary peaks in their absorption spectra (Fig. 2.33e), except for (+)(6,4), which is spatially most isolated. The CD data in Fig. 2.33d also show some cross-contamination between (6,4) and (7,3) species in all fractions except (+)(6,4). Interestingly, there appears to be less mixing between enantiomers than between (*n*,*m*) species in these fractions.

2.6.4. Sorting of SWCNT enantiomers using SC as a single surfactant

We also achieved partial enantiomeric sorting of (7,5) nanotubes suspended in SC alone. In this case, for the splitting of SWCNT bands as demonstrated in Fig. 2.34, the starting HiPco material was dispersed in 1% (w/v) SC instead, and the SC concentration in density gradient layers was kept at 0.6% (w/v). After layering of iodixanol solution the capped centrifuge tube was then held at an angle of ~10 degrees from horizontal for 1 h

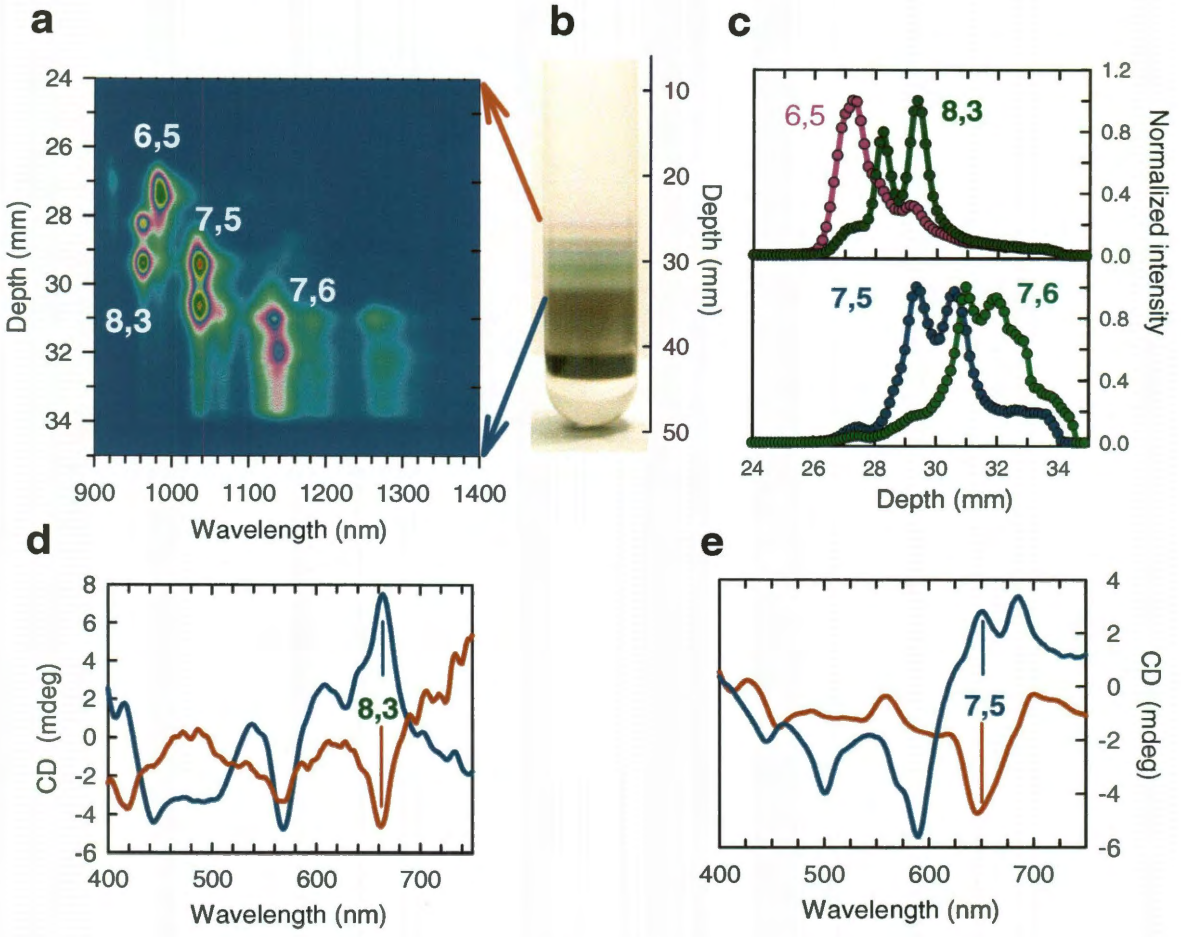

Figure 2.34 Single-surfactant separation of SWCNT enantiomers. **(a)** Vertical fluorescence spectral map showing three pairs of enantiomers spatially resolved by NDGU. The HiPco sample was dispersed in 1% (instead of 2%) SC and the gradient medium contained 0.6 % SC. **(b)** Photo of the centrifuge tube mapped in frame **a**. **(c)** Normalized emission intensity as a function of depth in centrifuge tube for the (6,5), (8,3), (7,5), and (7,6) species. Double peaks in these plots arise from spatially separated enantiomers. **(d)** CD spectra of the fractionated (8,3) upper and lower bands, showing opposite rotations at the E_{22} transition of (8,3). The reference spectrum was taken with an aqueous solution with similar surfactant and iodixanol contents. **(e)** CD spectra of the fractionated (7,5) lower and upper bands.

to allow diffusional formation of a nonlinear gradient. The average optical density (at 984 nm) of starting material was adjusted to ~6.0 (1 cm optical path) and used for sorting of SWCNT enantiomers. A 900 μL sample consisting of HiPco SWCNTs, 1% (w/v) SC and 27.5% (w/v) iodixanol was created by mixing 413 μL of 60% (w/v) iodixanol with 0.6% SC and 487 μL of pre-dispersed SWCNTs in 1% (w/v) SC solution. The resultant mixture was slowly inserted into the density-matched region (~27.5% iodixanol content) of the pre-made complex density gradient. Centrifugation was then carried out in a MLS-50 rotor, at 50 krpm for 18 h at a temperature of 22 °C.

2.6.5. Structure dependent optical activity of nanotube enantiomers

Figure 2.35 demonstrates structure dependent optical activity of nanotube enantiomers for six different (*n,m*) species. Different magnitudes of optical activity for the left and right handed enantiomers of same (*n,m*) species probably reflect cross contamination during sample extraction. For example, the sample enriched with (+)(6,4)

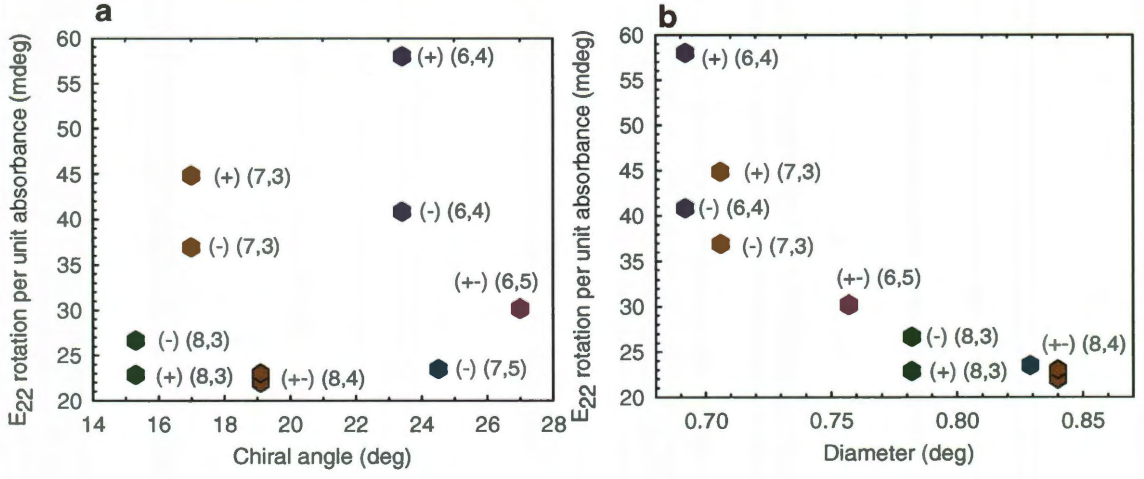

Figure 2.35 Dependence of normalized peak optical rotation of SWCNT enantiomers **(a)** on chiral angle, **(b)** on tube diameter.

exhibits higher CD rotation than (-)(6,4). It is also obvious from the plot that optical activity systematically decreases with increasing nanotube diameter.

2.7. Characterization of sorted SWCNT lengths

Atomic force microscopy (AFM) was utilized to analyze lengths of the fraction enriched in (7,6) SWCNTs (0.895 nm diameter). Figure 2.36 shows an AFM image of this fraction along with the length histogram. To remove iodixanol, the sample was first dialyzed against 0.1% SC (w/v) using a dialysis cassette (Slide-A-Lyzer, 3,500 MW, vol. 0.1-0.5 ml). 10 μL of dialyzed sample was further diluted to 100 μL with water and mildly bath-sonicated for 2 min. Then 10 μL of the diluted sample was immediately deposited on freshly cleaved mica surface, passively dried for five min, and finally dried with a stream of dry N_2. The AFM image was taken over a $(5\ \mu m)^2$ area with 512 samples/line resolution in tapping mode using a Digital Instruments NanoScope IIIA. SWCNT lengths were measured manually from the AFM image and compiled into the histogram shown in Fig. 2.36. Objects shorter than 80 nm were ignored.

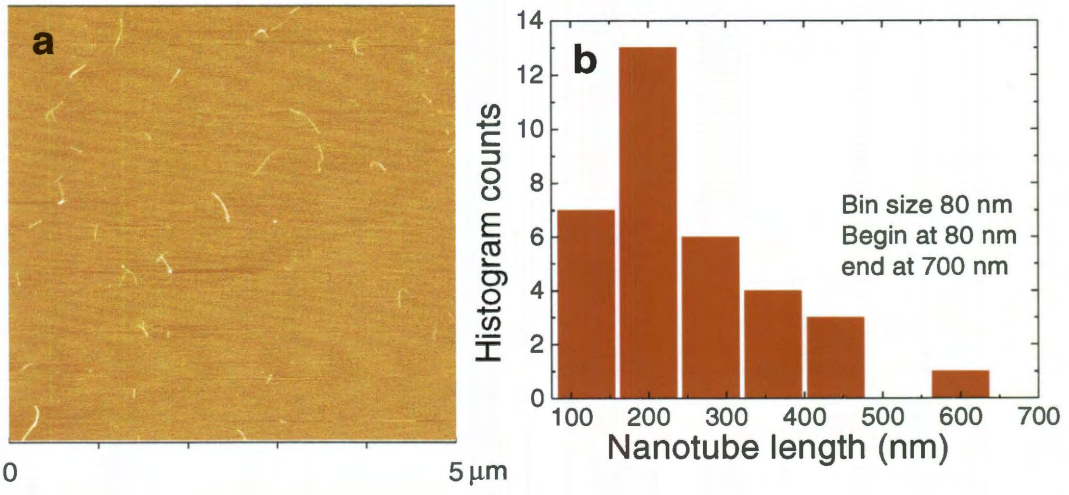

Figure 2.36 AFM image and corresponding length histogram of extracted SWCNTs in a (7,6)- enriched fraction purified by NDGU.

2.8. Discussion

2.8.1. Performance considerations

2.8.1.1. (*n*,*m*) separations

Despite the wide structural variety of raw HiPco nanotubes, NDGU sorting provides fractions substantially enriched in at least ten distinct semiconducting (*n*,*m*) species through a one-step process. The key advance is the use of tailored density gradient profiles with very shallow gradients that allow species with slightly different densities to be spatially separated for effective fractionation. The main impurities in (*n*,*m*)-enriched fractions are those SWCNT species with similar diameters and overlapping spatial distributions. The very high fluorescence efficiencies observed for DGU-sorted fractions imply that the processed nanotubes have a high level of structural perfection, because emission from the highly mobile SWCNT excitons is strongly quenched by trace concentrations of defects or derivatization sites.[49]

Using SC as the sole surfactant, optimal DGU sorting is obtained when the SC concentration is 2% during the initial dispersion step and ~0.7% in the density gradient medium. We found that SC concentrations above 1.0% in the density gradient medium degraded the (*n*,*m*) resolution. Lower surfactant concentrations may lead to more homogeneous micellar SWCNT coatings having better defined densities. As illustrated in Fig. 2.18, (*n*,*m*)-enriched fractions obtained through single-pass NDGU have dramatically reduced absorption backgrounds compared to unsorted SWCNT sample. They therefore enable spectroscopic studies that are not feasible with unrefined samples.

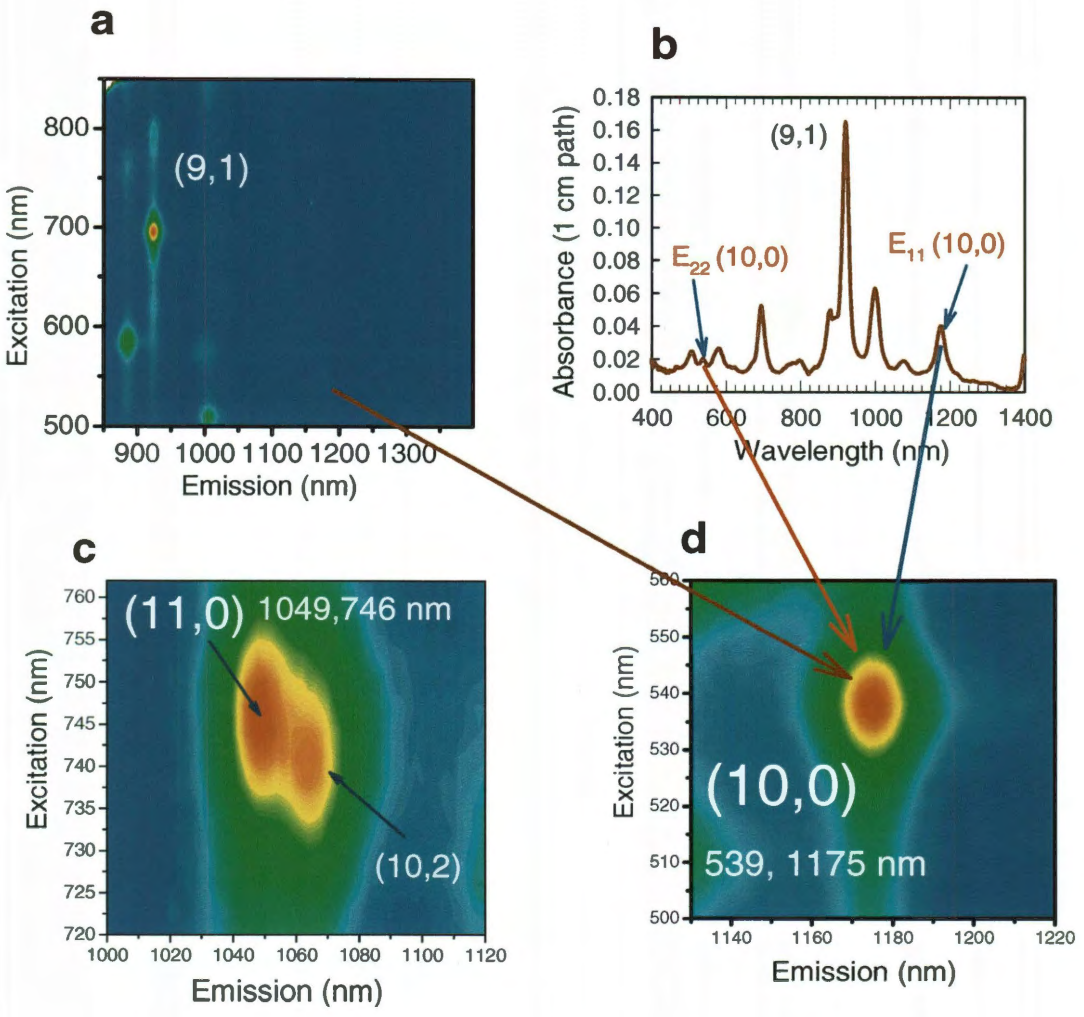

Figure 2.37 Novel spectroscopic signatures of two zigzag semiconducting SWCNTs [(10,0) and (11,0)] uncovered by sorting HiPco SWCNTs. **(a)** PL excitation-emission map of the (9,1)-enriched fraction, which also contains some (10,0) SWCNTs. **(b)** Absorption spectra of the (9,1)-enriched fraction. E_{11} and E_{22} transitions of (10,0) are clearly visible, as marked. **(c)** Expanded PL excitation-emission map of the fraction containing (11,0). **(d)** Expanded PL excitation-emission map of the (9,1) enriched fraction showing the well-resolved peak from (10,0) SWCNTs in SC suspension.

For example, the absorption spectrum of our (9,1)-enriched fraction (Fig 2.37b) contains clear secondary peaks at 1175 and 539 nm. Using the empirical spectral model developed previously,[10] we assign these to the E_{11} and E_{22} transitions of (10,0), a species that has

remained nearly undetectable because of low abundance relative to other species with nearby optical transitions. Figure 2.37 also shows the PLE map for (10,0) and spectral data for (11,0), another previously obscure zigzag species. The (10,0) and (11,0) SWCNTs hold special interest as the only observed semiconducting species with achiral, axially symmetric structures.

2.8.1.2. Enantiomeric separations

The other DGU advancement demonstrated here is one-step enantiomeric sorting of HiPco samples. Our method combines the new nonlinear density gradient approach with the previously reported combination of SC and SDS co-surfactants. We obtained highly enantiomerically enriched fractions of seven pairs of (*n*,*m*) species: (6,5), (8,3), (8,4), (6,4), (7,3), (7,5) and (9,1). Spatial separations between enantiomer layers range from ~1 to 5 mm. Except for (8,4) (for which the isomers were not clearly resolved) and (7,5), we found that the lower density, upper enantiomer gives positive-going CD signals at the E_{22} transition. Optical spectra of the upper enantiomers are red-shifted relative to the lower enantiomers. The lower effective densities and spectral red shifts both reflect systematic helicity-dependent differences in the nanotube coatings, with a higher SDS content around the higher density enantiomer. The SC surfactant, which has a biological source, is optically active and evidently has a higher affinity for a particular enantiomer of a given (*n*,*m*) species. A similar preferential chiral affinity of SC has been used to separate enantiomers of an organic analyte in micellar electrokinetic capillary chromatography.[50] In the presence of achiral SDS co-surfactant, the ratio of SC to SDS on the nanotube will differ between the nanotube enantiomers. This surfactant

competition gives the enantiomers distinct dielectric environments and effective densities, leading to the observed spectral shifts and spatially resolved DGU bands.

Although the clearest DGU sorting of SWCNT enantiomers has required mixed surfactants, some partial enantiomeric separations can be obtained using only SC (Fig. 2.34). This implies that enantiomers may be partially separated in many DGU runs designed only to sort by (*n*,*m*). We suggest that such unintended enantiomeric separation is a major mechanism that broadens layers and limits (*n*,*m*) spatial resolution in DGU with chiral surfactants.

Our spectra confirm earlier observations that E_{ii} CD peaks alternate in sign from E_{11} to E_{22} to E_{33}, etc. for a given (*n*,*m*) species.[51] We note that the subscript *i* indexes the electronic angular momentum of a SWCNT sub-band, and for some species the energies of higher E_{ii} transitions do not increase monotonically with *i*. For example, our (8,3) CD spectrum in Fig. 2.31c shows that the strong 355 nm peak has the same sign as the E_{22} peak and is therefore properly assigned as E_{44} rather than E_{33}. This "cross-over" behavior in the energy ordering of (8,3) E_{33} and E_{44} transitions was deduced previously from a combined resonance Raman and photoluminescence study,[52] and a similar cross-over was found for (6,4) by Green et al. from their CD spectroscopy of DGU-enriched enantiomeric fractions.[48] Our CD spectra also contain several additional peaks, many of type E_{ij} (with $j = i \pm 1$) arising from optical transitions polarized perpendicular to the nanotube axis.[53]

Using IUPAC nomenclature, nanotubes with right-handed helicity are designated "P" and those with left-handed helicity "M". To deduce the helicity of enantiomerically enriched SWCNT fractions prepared by complexation with chiral diporphyrin

compounds of known structure, Peng *et al.* used molecular mechanics modeling to estimate relative affinities of the diporphyrins with P and M (6,5) nanotubes.[51,54,55] Based on a calculated affinity difference of 0.22 kcal/mol, they identified the (6,5) enantiomer that shows a positive E_{22} CD signal as the M structure. In view of the challenges in computing sub-kilocalorie differences in molecular interaction energies, we suggest that more direct experimental determinations will be needed to confirm absolute helicities of separated SWCNT enantiomers.

2.9. Conclusions for chapter 2

We have significantly enhanced the performance of DGU by introducing the use of carefully prepared nonlinear density gradients. Furthermore, experimental conditions have been optimized with the aid of a device that quickly measures fluorescence maps to reveal the spatial locations and profiles of (*n*,*m*) fractions inside undisturbed centrifuge tubes. Although previous DGU studies focused on sorting samples containing relatively few species, our approach is successful with polydisperse samples grown by the HiPco method. Such samples can be highly enriched in at least ten different (*n*,*m*) species. In addition, the combined use of co-surfactants and nonlinear gradients permits the separation of seven (*n*,*m*) enantiomeric pairs. All of these separations are achieved with a single-step of NDGU processing.

CHAPTER 3

OXYGEN DOPING MODIFIES NEAR-IR BAND GAPS IN FLUORESCENT SWCNTs

3.1. Introduction

A variety of optical and electronic applications would benefit from controlled modification of SWCNT band gaps in bulk samples, individual nanotubes, and even segments within nanotubes. Covalent sidewall reactions have been used to bond nanotubes to chemical groups having a range of selected electronic properties.[56,57] However, to date such reactions have randomly eroded the highly ordered nanotube π-electron structure. The additional covalent bonds remove electrons from the π-system, broadening and suppressing the signature near-IR fluorescence peaks of semiconducting SWCNTs.[58] Here we describe a different type of chemically modified oxygen treated SWCNT that is more analogous to dopant-tuned semiconductor materials. These stable and easily prepared oxygen-doped nanotubes are near-IR fluorophores that display distinct, structure-specific optical properties systematically shifted from those of the pristine parent. They are more readily detected than pristine nanotubes.

3.2. Experimental details

3.2.1. Preparation of pristine SWCNT samples

We produce these modified SWCNTs by exposing aqueous suspensions of pristine SWCNTs to low doses of ozone and then photolyzing the resulting product.[59] Our studies rely on samples highly enriched in individual semiconducting (*n*,*m*) species through NDGU.[43] We utilized SWCNTs produced in the Rice University HiPco reactor (batch HPR 188.4 and 161.2), except for limited experiments with a CoMoCAT sample

(SWeNT, Norman, OK). Approximately 5 mg of raw nanotubes were added to a vial containing 10 mL of aqueous 2% (w/v) sodium cholate (SC). The vial was bath-sonicated for 1 h (Sharpertek Stamina XP) and then tip-sonicated for 30 min (Misonix Microson XL) at a power level of 7 W. The resulting aqueous dispersion was centrifuged at 13,300 x g for 1 h (Biofuge-13, Baxter Scientific) to pellet out large nanotube aggregates and residual iron catalyst. The supernatant was then diluted to give an absorbance of ~7 per cm at 984 nm. This suspension was used as the starting material for single-step NDGU through the method described in the previous chapter.

Fractions enriched in specific (*n,m*) semiconducting species with diameters between 0.69 and 0.89 nm were extracted from the NDGU-processed centrifuge tube using a 100 μL syringe (HPLC grade, gas-tight fixed needle, Hamilton Inc.) attached to a vertically mounted translation stage. Portions of 25 μL were withdrawn and then diluted to 100 μL with surfactant solution for optical measurements. The density gradient medium, iodixanol, was removed by repeated centrifugal filtration (Nanosep, pore size 10 k MW). Sorted samples were filtered at 5000 rpm (~2,000 ×g) for 10 min in the benchtop centrifuge (Baxter Scientific, Biofuge-13) and then re-dispersed into aqueous solutions of sodium tridecylbenzenesulfonate (STBS, 0.2% (w/v)). This surfactant was found to allow more facile SWCNT ozonation than other common ionic surfactants used at higher concentrations. In some cases, centrifugal filtration procedure was repeated for two to three times to remove excess SC and iodixanol from the fractionated samples.

3.2.2. Ozonation of (n,m)-sorted SWCNT suspensions

To perform oxygen doping, we added trace amounts of ozonated water to the (*n,m*)-sorted SWCNT suspensions using the following steps. An Ozone Services model

GE 60-FM 500 generator was used to produce a 31 mL/min gas flow containing ~90 μg/mL of ozone in dry oxygen. This stream was bubbled for 5 min through a 5 mL sample of de-ionized water in a 18 mL glass vial. The resulting O_3 concentration was monitored by measuring optical absorbance of the treated water at 262 nm, using a Cary 3000 spectrophotometer (see Table 3.1 for detailed protocols). For oxygen doping of (6,5) SWCNTs, 30 μL of ozonated water was slowly added with stirring to 100 μL of a highly enriched (6,5) suspension dispersed in 0.2% STBS. The product suspension was then photoconverted by several hours of irradiation by a common fluorescent desk lamp or a light emitting diode. A 475 nm long-pass filter was normally used to block violet and ultraviolet light during irradiation. Changes in sample composition were monitored by near-IR fluorescence spectroscopy using a model NS1 NanoSpectralyzer (Applied NanoFluorescence, LLC). We found that lamp irradiation for 16 h gave a stable conversion level. Table 3.1 lists experimental parameters for treatment of 100 μL samples of other (*n*,*m*) species.

We found that for efficient oxygen treatment, ozonated water needs to be added to a SWCNT sample immediately after collection of ozone since O_3 decays faster in water than in air. It is essential to the keep surfactant concentration near 0.2% (w/v) during ozone addition. Also, the density gradient medium (iodixanol) needs to be removed completely, by repeated centrifugal filtration. Otherwise added O_3 can be consumed by the excess surfactant or iodixanol before functionalizing SWCNTs. After treatment and photo-conversion, the surfactant concentration should be raised to 1.0% to obtain a stable SWCNT suspension.

Alternatively, oxidation of SWCNTs can be achieved by direct addition of gaseous O_3 (in dry oxygen) to aqueous nanotube suspensions. Careful bubbling of O_3 using a 3 mL syringe/plunger setup filled with O_3 gives the desired nanotube sidewall derivatization. In this case, about 100 μL of O_3 in dry O_2 (50 μg/mL) is bubbled through 250 μL of aqueous SWCNT suspension with an optical density of ~0.2 at E_{11} peak. However, too much ozonation can significantly decrease bulk sample fluorescence due to excessive functionalization. For efficient doping with significant photoconversion of an (*n,m*)-sorted concentrated SWCNT sample, multiple ozonation steps (by direct addition of gaseous O_3 to sample) followed by multiple light exposures are necessary. Before exposing a treated sample to light, it is advisable to check for a slight increase in the Raman D/G ratio from ozonation in order to confirm that the added O_3 reacted with the nanotubes rather than only with surfactant.

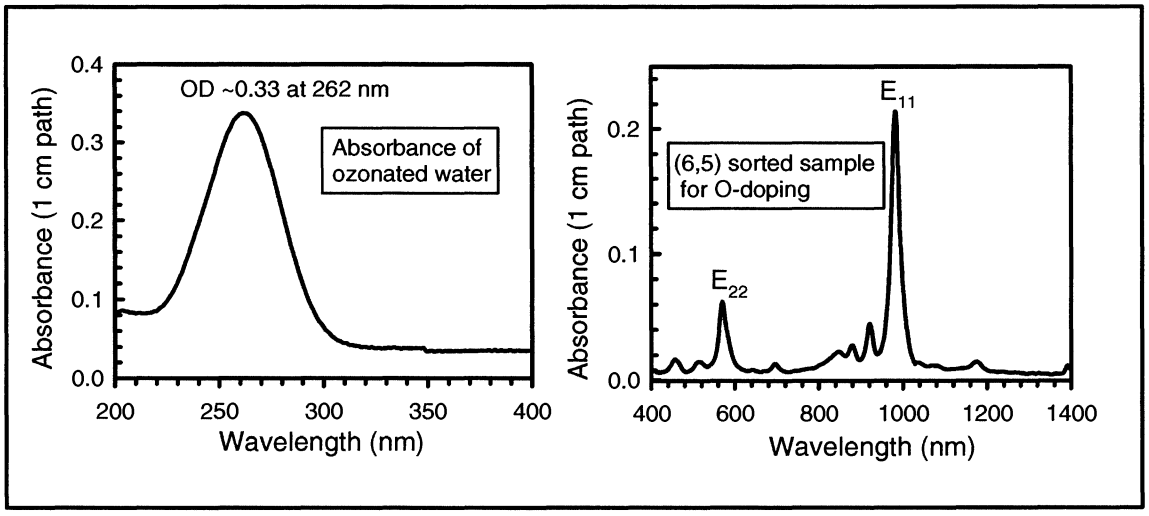

Figure 3.1 Standard optical density (1 cm optical path) of the ozonated water and surfactant suspended (6,5)-enriched nanotube suspensions used for oxygen doping.

(*n*,*m*)	A of sample at E_{11} peak (1 cm path)	volume of ozonated water added (μL)	A of ozonated water at 262 nm	no. of O_3 additions	light irradiation time (h)	light source (average LED power ~3 W)	Main band to side band % conversion
6,4	0.15	15-25	0.2-0.25	1	2-5	desk lamp / 598 nm LED	85 - 93
7,3	0.15	20-30	0.2-0.3	1	2-5	desk lamp / 464 nm LED	85 - 95
6,5	0.2	30-40	0.3-0.4	1	10-16	desk lamp / 594 nm LED	80 - 90
8,3	0.2	30-40	0.3-0.4	1	10-16	desk lamp / 640 nm LED	80 - 85
9,2	0.2	20-30	0.2-0.3	1	48-72	desk lamp	15 - 20
7,5	0.5	30-50	0.3-0.4	2	48-72	desk lamp / 640 nm LED	50 - 60
8,4	0.2	40-50	0.2-0.3	2	48-72	desk lamp	30 - 40
10,2	0.2	20-40	0.2-0.3	1	48-72	desk lamp	15 - 20
7,6	0.5	50-60	0.3-0.4	2	48-72	desk lamp / 640 nm LED	55 - 60

Table 3.1 Experimental parameters used for SWCNT oxygen-doping

3.2.3. Optical characterization of bulk SWCNT samples

3.2.3.1. Optical absorption spectra

Optical absorption spectra were measured in a model NS1 NanoSpectralyzer from 400 to 1400 nm relative to a matched reference containing surfactant solution at the same concentrations. Optical path lengths were 1.0 cm and the spectral resolution was 1 nm in the visible and 4 nm in the near-IR. Absorption spectra are displayed without background subtraction or vertical offset.

3.2.3.2. Fluorescence spectra of pristine and treated samples

Fluorescence characterization of SWCNT samples was normally performed with fixed wavelength laser excitation in the model NS1 NanoSpectralyzer. For full excitation-emission scans, we used a Spex Fluorolog 3-211 spectrofluorometer equipped with a liquid nitrogen cooled single-channel InGaAs detector. In general, the excitation

wavelength was varied from 500 to 800 nm in 5 nm steps while the emission wavelength was varied from 850 to 1399 nm in 3 nm steps. The excitation spectral slit width was 10 nm and the emission slit width was 6 nm. Measured intensities were corrected for excitation lamp power and emission system sensitivity. One RG-830 (3 mm thick) filter was used to block scattered excitation light in the emission channel.

3.3. Photophysical properties of bulk O-doped SWCNTs

3.3.1. Optical characterization of O-doped SWCNTs

The simpler optical spectra of (*n,m*) sorted SWCNT samples allow monitoring of the conversion reaction by fluorescence spectroscopy. Immediately after mild ozone exposure, the characteristic near-IR E_{11} fluorescence band shows small red-shifts (~0.2%) and appreciable broadening (~5%). Subsequent exposure to light induces a new emission feature, termed E_{11}*, that is red-shifted from E_{11}. Spectra measured during this transformation are shown for a (6,5)-enriched sample (Fig. 3.2a). During photo-transformation by light from a fluorescent desk lamp, 980 nm E_{11} emission diminishes as the 1120 nm E_{11}* feature increases (Figs. 3.2a and b). However, except for some broadening, the absorption spectrum remains essentially unchanged by this conversion (Fig. 3.2c). The transformed nanotubes show no appreciable absorption at their new emission peak, unlike pristine SWCNTs. We estimate that the photoconversion efficiency is very low, requiring 10^7 to 10^9 absorbed photons per micrometer of SWCNT length. An excitation-emission contour plot demonstrates that near-IR emission from both the original and the transformed (6,5) sample is induced by absorption at the same E_{22} transition (Fig. 3.2d). The shifted emission from our converted SWCNTs differs in wavelength from the weak intrinsic satellite features observed in pristine samples.[60-62]

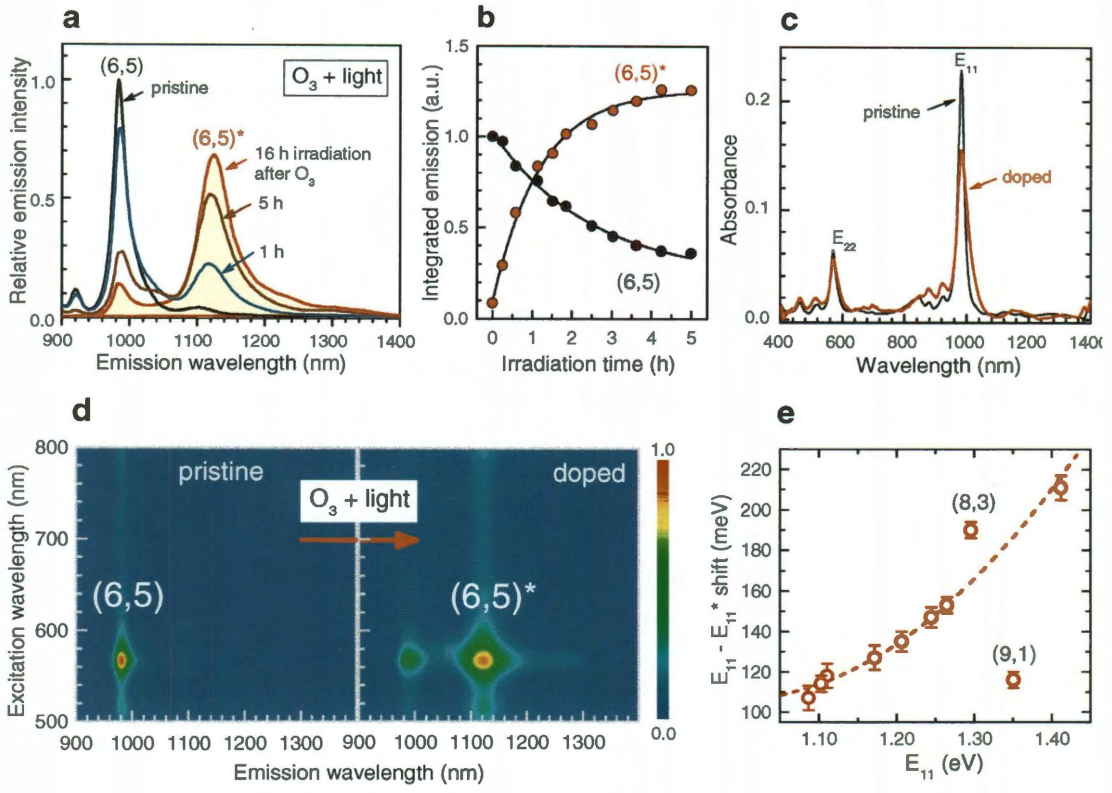

Figure 3.2 Spectral changes in a (6,5)-enriched SWCNT dispersion exposed to ozone and light. (**a**) Emission spectra measured with 785 nm excitation after a single treatment with ozone and 1 to 16 h of white light irradiation. (**b**) Spectrally integrated emission under the (6,5) main band (black) and side band (red) vs. irradiation time with a desk lamp. (**c**) Absorption spectra (1 cm path length) of the SWCNT sample before (black) and after (red) treatment with ozone and light. **(d)** Photoluminescence excitation-emission contour plots from the (6,5)-enriched sample before and after treatment. The (6,5)* emission feature shows the same excitation peak wavelength as the (6,5) feature. (**e**) Measured photon energy differences between the unshifted and shifted fluorescence peaks of ten different bulk (*n*,*m*) species as a function of unshifted emission energy. Points show experimental data and the dashed line is a quadratic function drawn to guide the eye. Two points far from the line are labeled with their (*n*,*m*) values.

In addition to the prominent shifted emission band, a weak secondary shifted feature can also be seen (discussed later). Very low ozone doses followed by photoconversion are required to prepare such modified SWCNTs. They are qualitatively different from those prepared through more extensive nanotube ozonation,[63-69] which quenches SWCNT near-IR fluorescence.[70] Among several ionic surfactants used to suspend samples during ozonation treatment, we found that sodium tridecylbenzenesulfonate (STBS) gave the most reproducible results, presumably because it could be used at lower concentrations that compete less for reaction with ozone. Moreover, resonance Raman spectra revealed that the ozone/photolysis transformation was accompanied by the appearance of a sharp D-band near 1310 cm^{-1} (Figs. 3.3 and 3.4) signifying covalent functionalization of the nanotube sidewall.

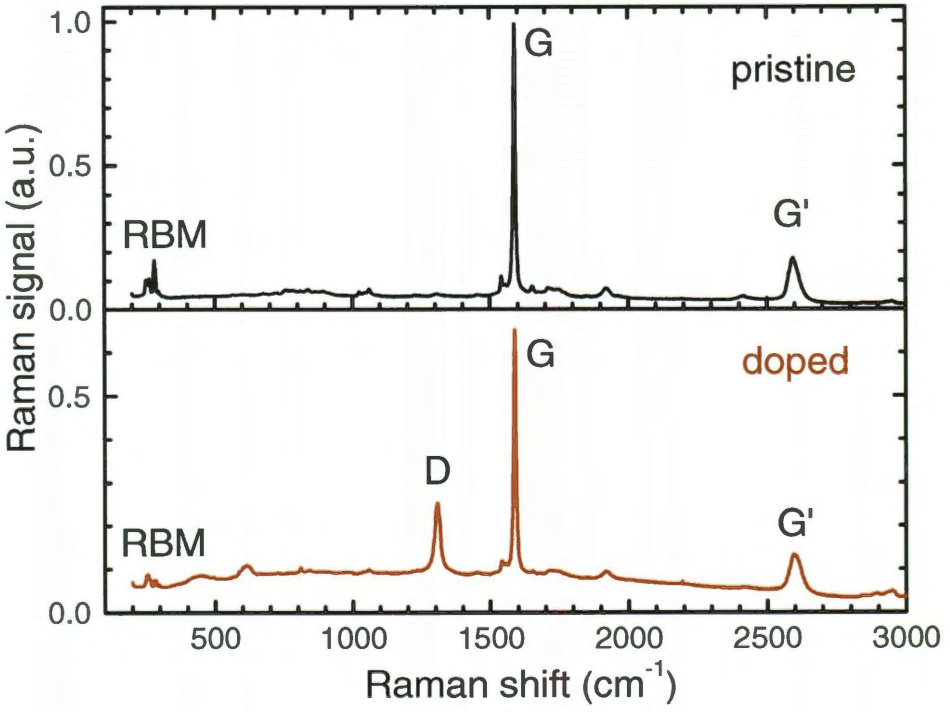

Figure 3.3 Raman spectra (633 nm excitation) of a (7,6)-enriched sample before doping (top frame) and after two doping treatments (bottom frame).

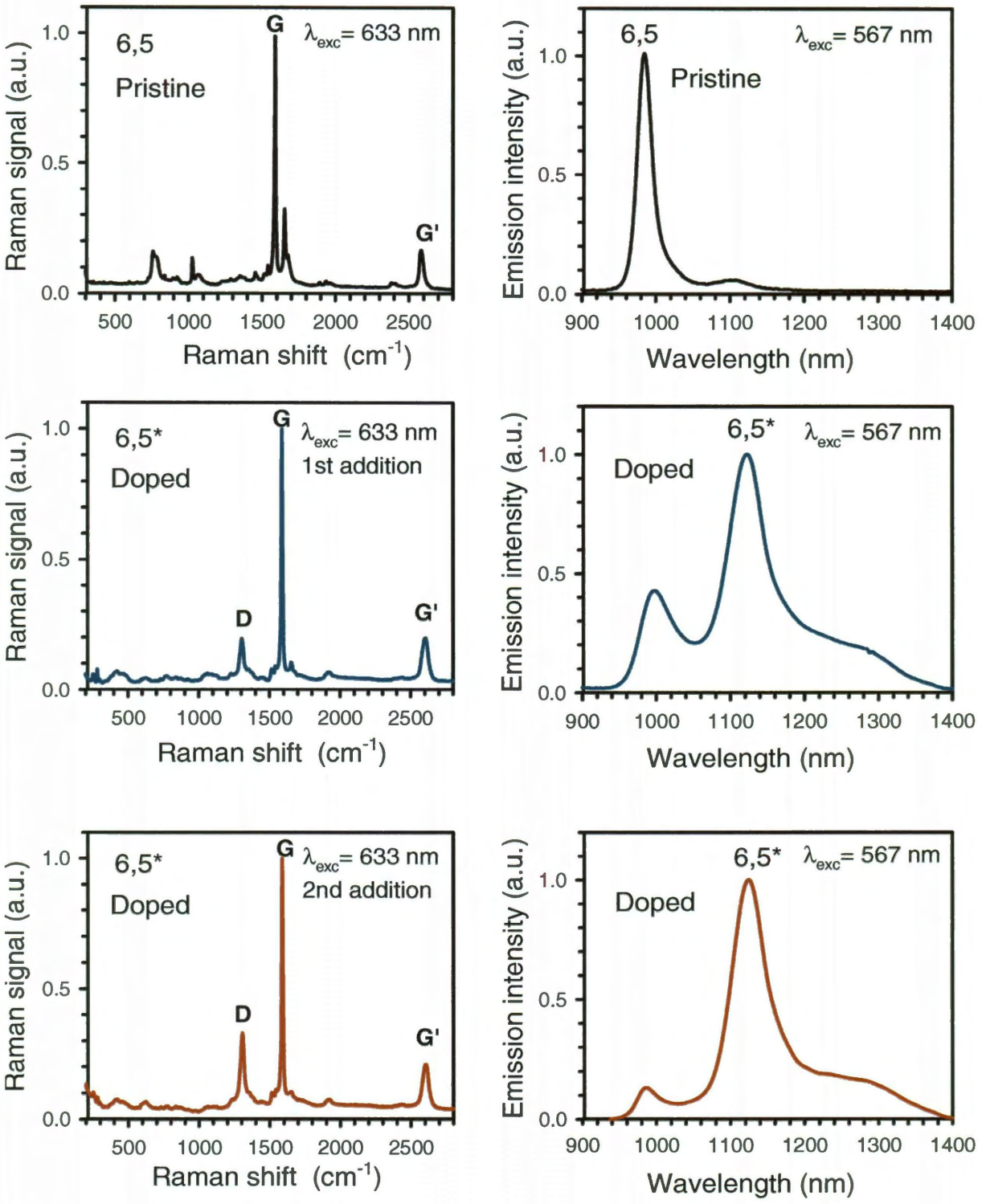

Figure 3.4 Raman and fluorescence spectra of a (6,5)-enriched sample after one and two oxygen doping treatments. Significant D band intensity is evident.

The transformation reaction also occurred, although less efficiently, when weaker oxidants H_2O_2 or K_2CrO_4 were substituted for ozone (Fig. 3.5). We conclude that the transformed nanotubes incorporate covalently bonded oxygen. Similar but unintended oxidation may have led to the defect-induced emission reported from some individual SWCNTs exposed to intense pulsed laser light.[71]

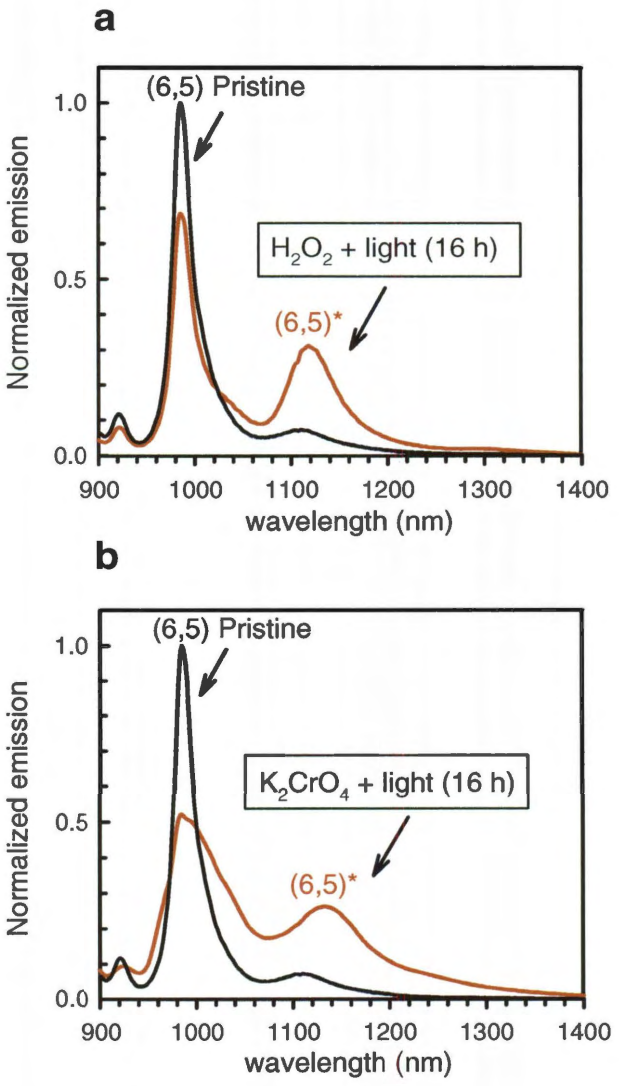

Figure 3.5 Fluorescence spectra showing oxygen doping of bulk (6,5) SWCNTs with alternate oxidizing reagents. **(a)** 30 µL of 30% hydrogen peroxide (H_2O_2, and **(b)** 30 µL of 0.1 M potassium chromate solution were added to 100 µL of (6,5)-enriched nanotube suspension and exposed to white light for 16 h.

3.3.2. O-doping of other semiconducting SWCNTs

Other semiconducting (*n,m*) species also underwent oxygen-doping. For example, bulk samples enriched in (6,4), (7,3), (8,3) showed reduced E_{11} emission and the growth of a new red-shifted E_{11}* emission band as they were treated with ozone and visible light (Fig. 3.6). However, in larger diameter species, such as (7,5), (8,4) and (7,6), spectral transformations were less efficient. We measured spectral positions and widths of E_{11}* peaks from 10 different oxygen-doped (*n,m*) species in STBS for comparison with their pristine forms (Table 3.2). The spectral red shifts between E_{11} and E_{11}* ranged from 106 to 214 meV and showed a strong positive correlation with E_{11} (Fig. 3.2e). These doping-induced shifts represent optical band gap decreases of 10 to 15% from the pristine values.

(n,m)	Pristine E_{11} peak (nm)	Treated E_{11} peak (nm)	Treated E_{11}* peak (nm)	Treated E_{11} - E_{11}* shift (meV)	Pristine E_{11} width (meV)	Treated E_{11} width (meV)	Treated E_{11}* width (meV)
(6,4)	878	889	1050	214	35	45	77
(7,3)	996	1012	1150	147	34	39	75
(9,1)	918	924	1012	117	26	43	73
(6,5)	980	983	1120	154	28	43	50
(8,3)	957	960	1125	189	26	31	48
(9,2)	1141	1147	1272	106	25	28	62
(7,5)	1027	1033	1155	127	23	41	56
(8,4)	1116	1125	1258	117	24	42	72
(10,2)	1058	1070	1190	117	22	24	56
(7,6)	1124	1135	1266	113	28	45	80

Note: Precise E_{11}* peak positions depend on the extent of doping.

Table 3.2 Comparative spectral characteristics of pristine and oxygen-doped SWCNTs.

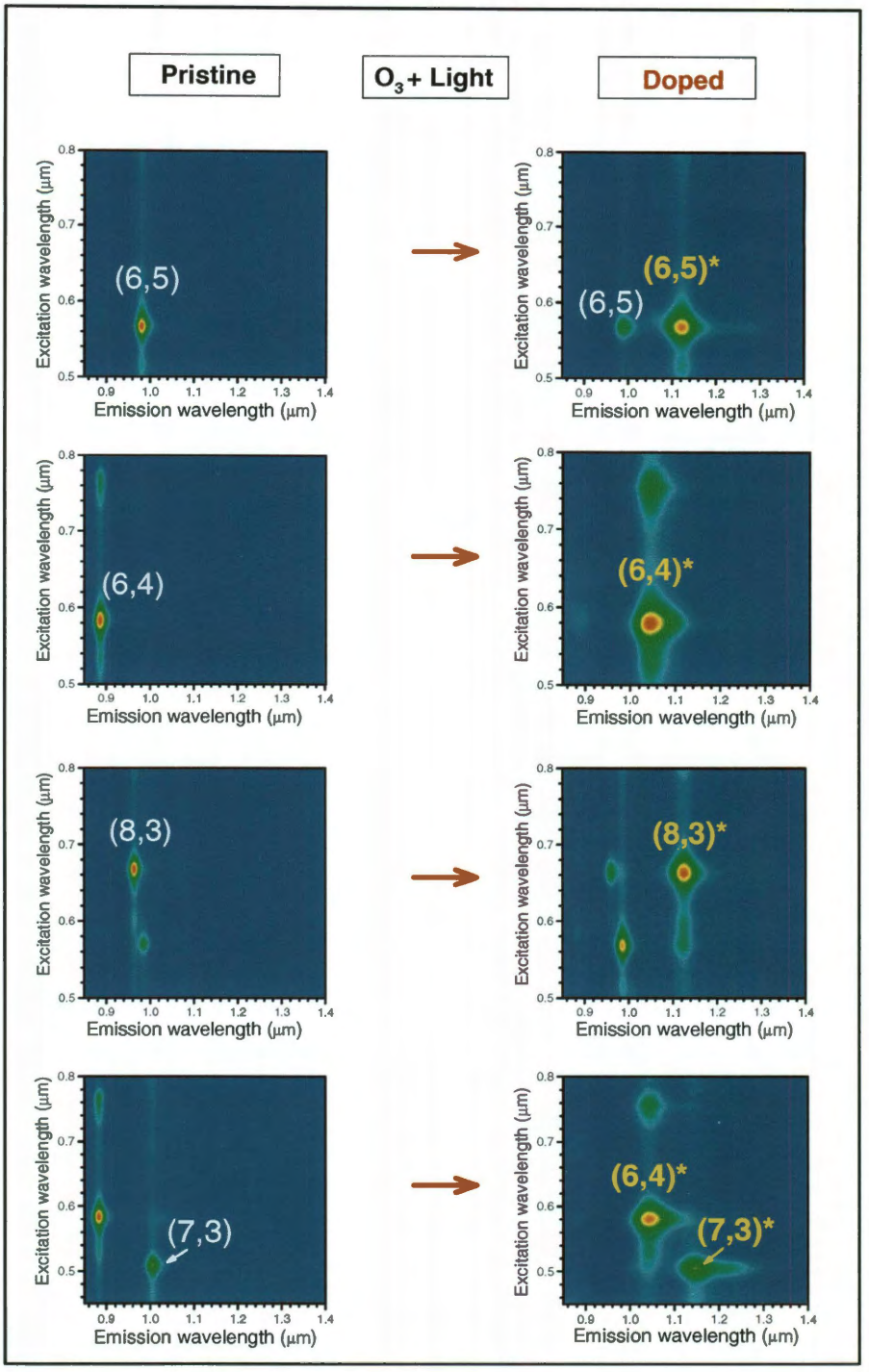

Figure 3.6 Fluorescence excitation-emission maps of bulk (*n,m*)-enriched pristine and oxygen-doped SWCNT species. Significant conversion was observed. New low energy bands are marked with a (*). Samples were dispersed in aqueous STBS.

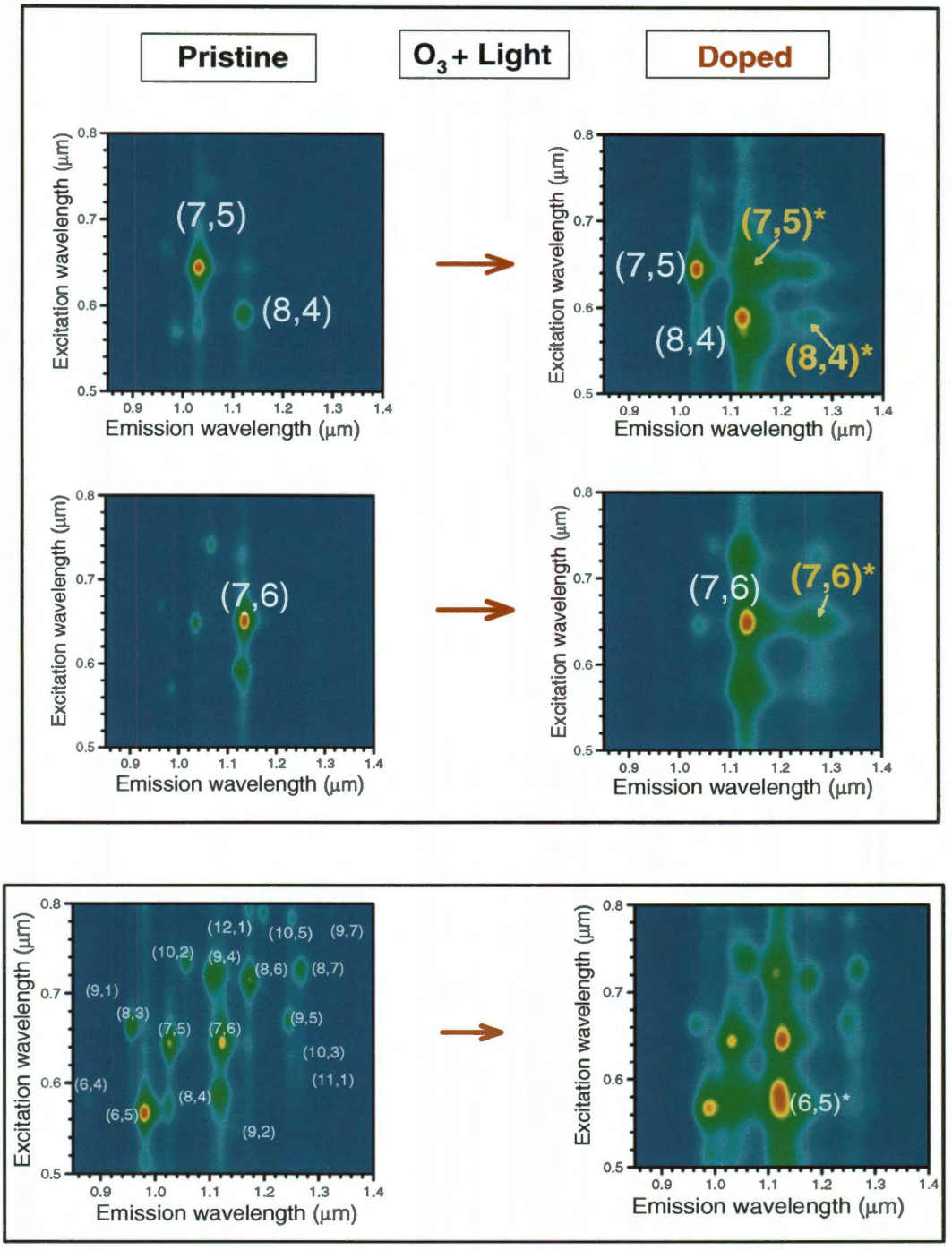

Figure 3.7 Upper panel, additional fluorescence excitation-emission maps of bulk (*n,m*)-enriched pristine and oxygen-doped SWCNT species. Lower panel, effect of oxygen doping treatment on unsorted HiPco SWCNTs

3.3.3. Fluorescence emission from O-doped SWCNTs with E_{11} excitation

The spectral separation of intense near-IR absorption and emission is absent in pristine SWCNTs as they overlap (Fig. 3.8a). In contrast, (E_{11}) near-IR absorption and emission peaks are well separated in O-doped SWCNTs (Fig. 3.8b). This feature allows greatly improved optical imaging and detection of the doped nanotubes.

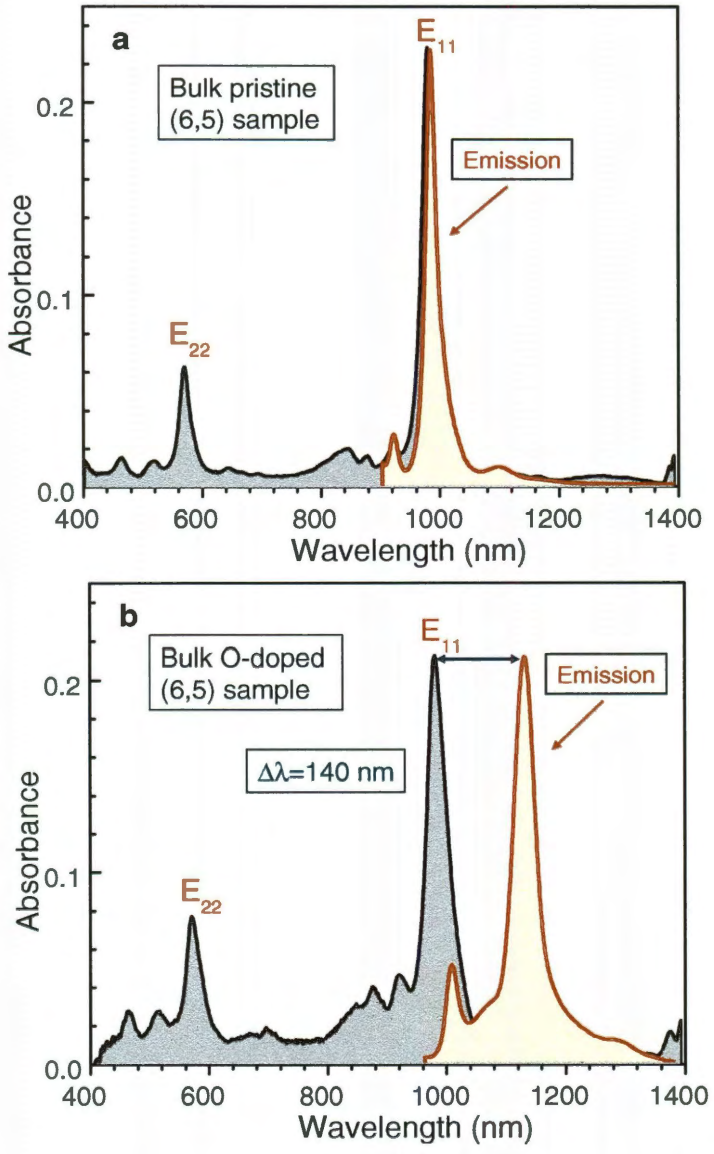

Figure 3.8 Absorption and emission spectra of **(a)** pristine bulk (6,5)-enriched sample and **(b)** O-doped (6,5) sample in aqueous suspension. E_{11} absorption and emission peaks are separated by 140 nm in O-doped SWCNTs.

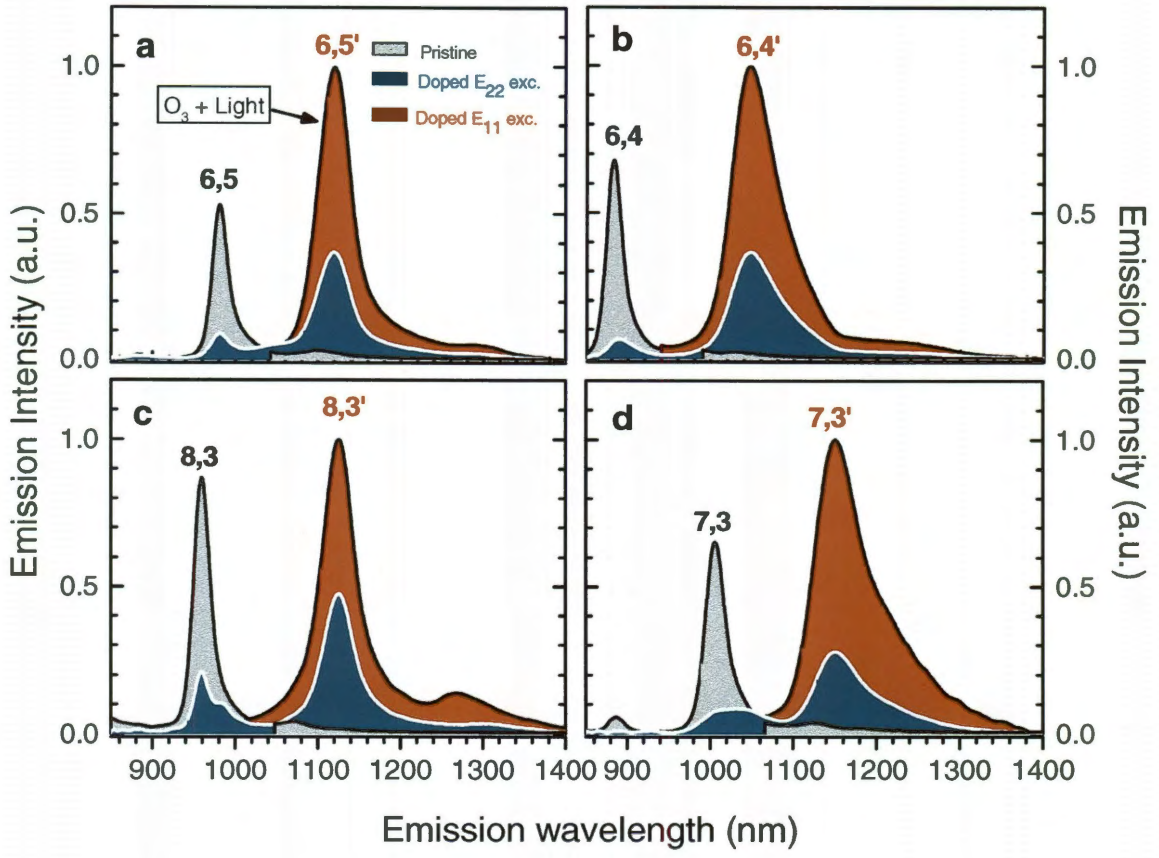

Figure 3.9 **(a)** Emission spectra of bulk (6,5)-enriched samples. The gray and blue peaks show emission with E_{22} excitation from pristine and O-doped samples, respectively; the red peak shows emission with the same power E_{11} excitation from the same doped sample. **(b)-(d)** Emission spectra of bulk (6,4), (8,3), (7,3)-enriched samples respectively, with color codes as in **(a)**.

Three factors contribute. First, excitation light can be tuned to a sample's E_{11} peak, which has greater absorptivity than the E_{22} peak that must be excited in a pristine- sample. Second, emission efficiency is also improved, as spectrally integrated E_{11}* emission exceeds E_{11} emission of the pristine SWCNT under equivalent excitation conditions. Third, E_{11}* emission is not reabsorbed by the O-doped sample due to separated E_{11}

absorption and emission. These differences are illustrated by three spectra recorded from the same (*n,m*)-enriched sample excited at corresponding E_{22} peak before doping, at E_{22} peak after doping, and at E_{11} peak after doping (Fig. 3.9). The second factor is that excitation with longer-wavelength, near-IR light generates far less background emission from biological or environmental specimens (discussed later in detail). Additionally, we measured fluorescence excitation spectra of O-doped SWCNTs for emission at shifted E_{11}* peaks. Figure 3.10 demonstrates a set of four excitation spectra with clearly visible E_{33}, E_{22}, and E_{11} transitions respectively.

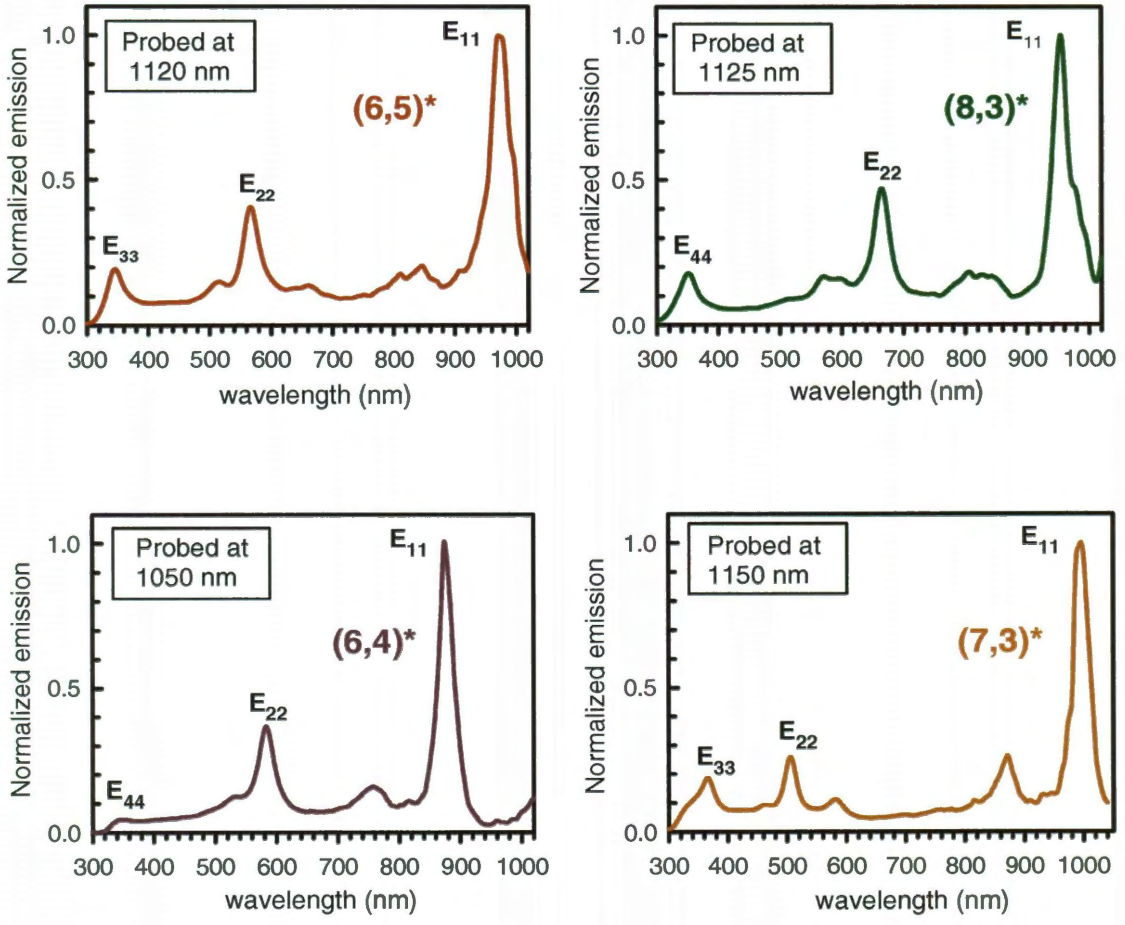

Figure 3.10 Fluorescence excitation spectra of oxygen-doped and heavily converted SWCNT species, for emission at the E_{11}* (shifted) peaks.

3.4. Single nanotube near-IR imaging of O-doped SWCNTs

3.4.1. Sample preparation

Treated SWCNTs dispersed in 0.2% aqueous STBS were diluted ~100-fold with aqueous surfactant solution. Then 5% agarose gels prepared with 1% STBS solution were melted slowly at 60 ^{o}C in a water bath, mixed thoroughly with the diluted SWCNT sample, deposited on a glass or quartz microscope slide, covered with a 22 x 22 mm cover slip, and allowed to solidify by cooling.

3.4.2. Near-IR fluorescence microscope

The basic apparatus used for microscopic imaging and spectroscopy of near-IR fluorescence has been described previously.[72] Slides with immobilized SWCNT samples were mounted onto an inverted microscope (Nikon TE-2000U) equipped with a 60x objective (NA = 1.4, Nikon). In this setup a single pixel on the InGaAs imager represented approximately 500 nm. In some cases, a 40x objective was utilized instead. Samples were continuously excited from above by a focused diode laser beam. A 785 nm laser was used to excite (6,4), (7,3), (6,5), (10,2), and (8,4) nanotubes, and a 658 nm laser was used to excite (8,3), (9,1), (7,5), and (7,6) nanotubes. Single nanotube emission spectra were acquired by averaging 10 to 20 acquisitions of 10 s each. For photostability measurements of an individual O-doped (6,4) nanotube irradiated with 775 nm light (Fig. 3.11c), a Ti:sapphire laser (Del Mar Photonics, Inc) was used. Near-IR fluorescence emission was passed through long-pass dielectric filters (Thorlabs LP850, LP900, LP950, LP1050, or LP1125) and imaged by a liquid nitrogen-cooled 16-bit InGaAs 2D array (OMA-V 2D, Princeton Instruments). In our study, typical nanotube signals were several thousand counts/pixel. A second microscope port was fiber optically coupled to a near-IR

spectrograph with a 512-channel InGaAs detector for recording single nanotube emission spectra.

3.4.3. Photophysical heterogeneity in O-doped SWCNTs

Spectroscopic measurements on individual nanotubes revealed photophysical heterogeneity in the doped samples. The results are illustrated with fluorescence spectra acquired from three individual nanotubes in a (6,5)-enriched bulk sample (Fig. 3.11a). One nanotube was pristine and the other two had been oxygen-doped. One of the two doped nanotubes showed an intense shifted emission band and nearly complete depletion of the normal band; the other emitted both shifted and normal bands with similar peak intensities.

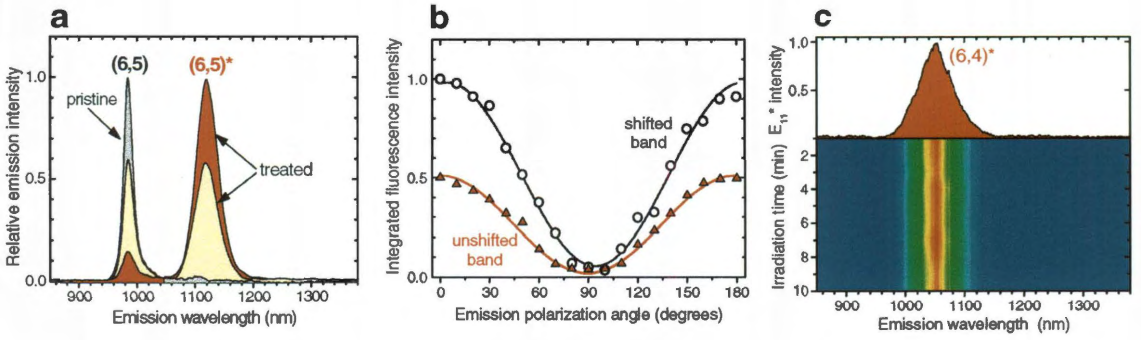

Figure 3.11 Spectral characterization of individual oxygen-doped SWCNTs. **(a)** Fluorescence emission spectra of three individual (6,5) nanotubes. The gray trace is from a pristine SWCNT; the red and yellow traces are from different treated nanotubes in the same bulk sample. **(b)** Spectrally integrated intensities from the nanotube giving the yellow trace in **(a)**, as a function of emission polarization angle. **(c)** Emission spectrum (top) and contour plot of successive emission spectra (bottom) from a single treated (6,4) SWCNT continuously irradiated by a 775 nm laser at an intensity of 150 W/cm^2. Spectra were acquired each minute.

These observations demonstrate that the extent of oxygen doping varies among nanotubes within the same bulk sample. Moreover, the bimodal emission traces imply

that individual nanotubes can contain both pristine and doped regions with independent fluorescence spectra. We have compared the polarization of E_{11} and E_{11}* emission from an individual SWCNT whose spectrum is shown in Fig. 3.10a. The integrated intensities of the two bands measured through a linear polarizer both follow a $\cos^2$ pattern with matching phase angles (Fig. 3.11b). This result demonstrates that E_{11}* emission arises from a transition dipole oriented parallel to that of the normal E_{11} emission, which is known to lie along the nanotube axis.

3.4.4. Photostability of O-doped (6,4) and (6,5)

Oxygen-doped SWCNTs showed good stability. Transformed bulk samples have been stored under ambient conditions for several months with no change in spectral properties. Additionally, to check photostability of doped species, we measured E_{11}* emission spectrum of an individual doped (6,4) nanotube at 1 min intervals while irradiating it with 775 nm light at 150 W/cm^2. The emission remained constant in peak position and shape, but showed a slight (~3%) decrease in intensity over the 10 min irradiation period (Fig. 3.11c).

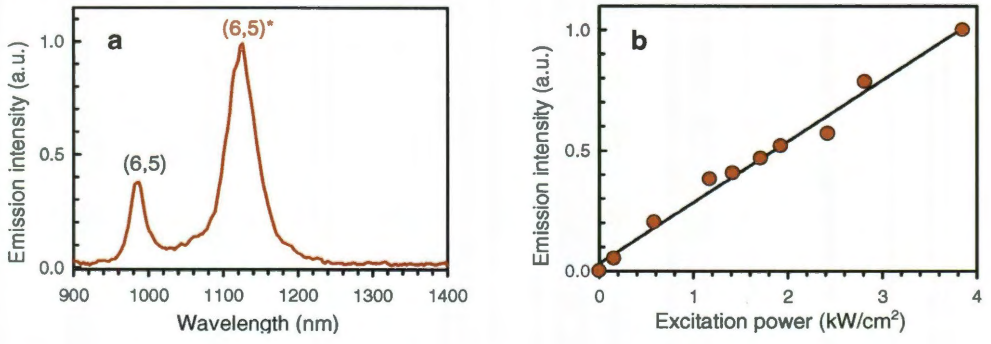

Figure 3.12 **(a)** Single nanotube near-IR emission from a heavily converted O-doped (6,5) SWCNT. The spectrum was measured by averaging 20 acquisitions of 10 s each, with 785 nm excitation. **(b)** Total emission intensity plotted as a function of excitation power.

Single O-doped (6,5) SWCNT also demonstrated remarkably stable emissive features while excited at different irradiation power (Fig. 3.12b). The E_{11}* emission intensity remains proportional to excitation intensity at levels up to several kW/cm^2.

3.4.5. Single-tube spectra of O-doped (7,6) and (10,2), and (9,1)

Additional evidence of O-doping is demonstrated in Fig. 3.13. Here, individual SWCNTs were taken from bulk (*n,m*)-enriched and oxygen treated samples and immobilized on glass slides using the protocol described earlier.

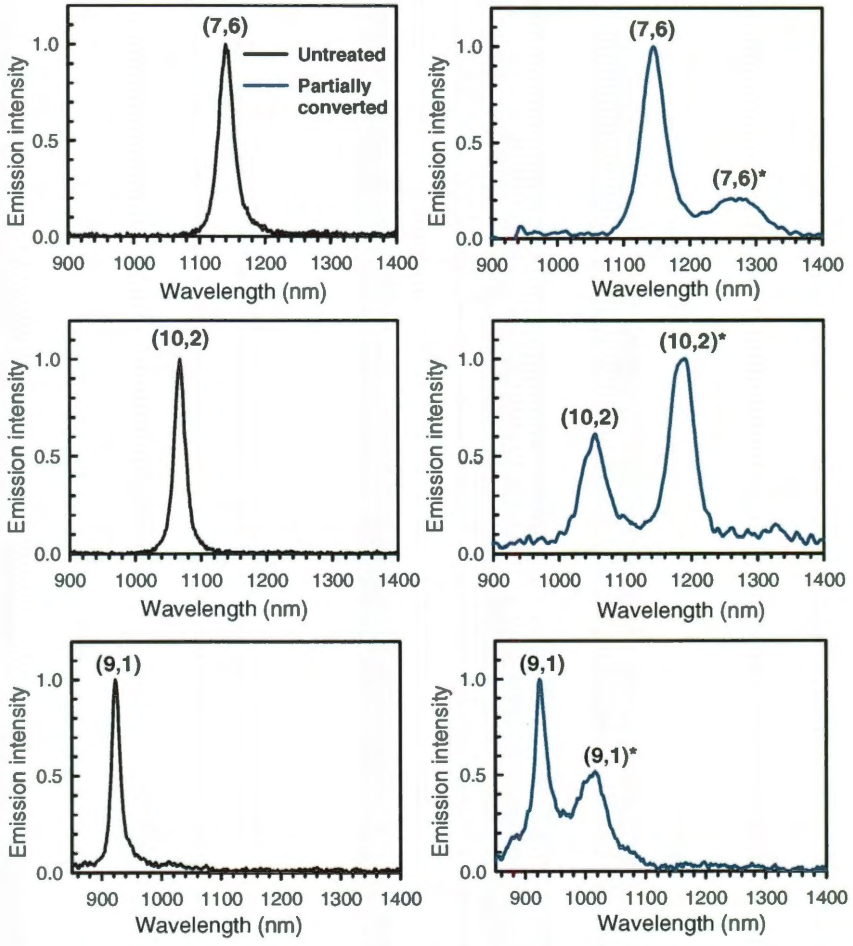

Figure 3.13 Single-nanotube fluorescence spectra from (7,6), (10,2) and (9,1) SWCNTs before and after oxygen doping treatment. Excitation wavelengths were 659 nm for (7,6) and 785 nm for (10,2) and (9,1).

3.5. Study and imaging of doped SWCNTs in human uterine adenocarcinoma cells

Specimens of 2000 human uterine adenocarcinoma cells were seeded into 40 μL wells of an 8-well chambered cover slip (Invitrogen #C24779) containing media plus 10% FBS. These were placed in a humidified 37 °C incubator with 5% CO_2. The cells were allowed to attach and grow for 24 h. Then the media was removed and 40 μL of a 1:100 dilution of oxygen-doped nanotubes in Pluronic F127, a nonionic biocompatible surfactant, (or a Pluronic-only control) was added to each well for an 18 h incubation. The SWCNT mass added per well was approximately 2.5 pg. After incubation, the cells were washed 3 times with 40 μL portions of PBS, fixed for 10 min at room temperature in 3% paraformaldehyde in PBS, washed once more in PBS, and immersed in 50% glycerol under a 22 x 50 mm cover slip that was sealed with nail polish. Images of (6,5) samples shown in Fig. 3.14 were obtained using direct E_{11} excitation with a 980 nm diode laser or direct E_{22} excitation with a 574 nm cw dye laser.

We demonstrated enhanced SWCNT detectivity by near-IR fluorescence microscopy of the human uterine adenocarcinoma cells cultured as described above. For comparison, 100 ms fluorescence images were recorded of the same specimen using E_{22} excitation (as is required for pristine samples) and E_{11} excitation of matched intensity. Optical filters blocked wavelengths below 1050 nm in the imaging path. We display the resulting images (false-colored, Fig. 3.14a,b) along with intensity profile plots along the horizontal lines drawn through the image frames (Fig. 3.14c,d). Most individual spots represent single nanotubes. The profile plots show that E_{11} excitation provides more than three times the emission intensity with 1/6 the background level, as compared to E_{22} excitation. This improved contrast by a factor of ~20.

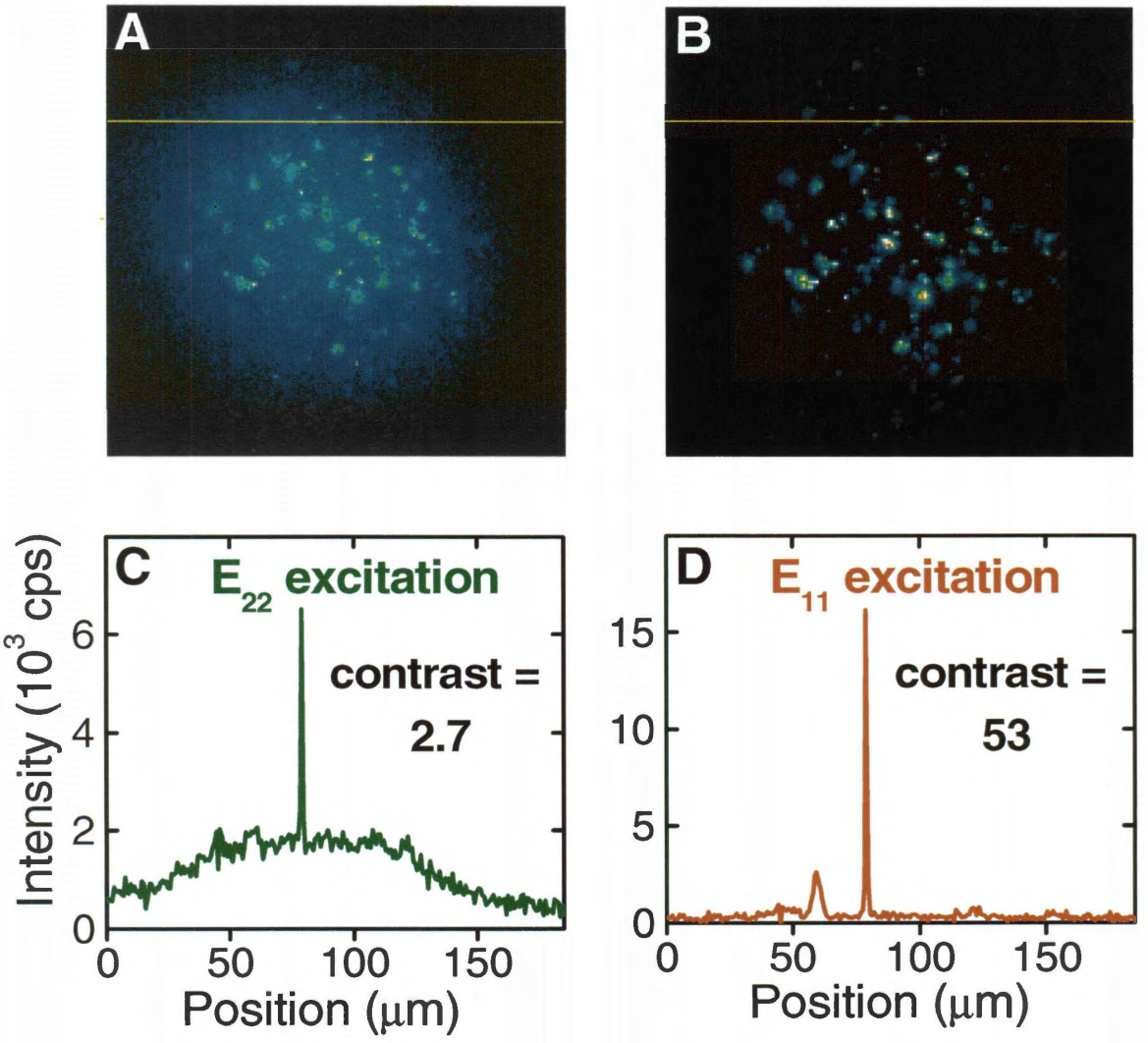

Figure 3.14 Comparative near-IR fluorescence micrographs (100 ms exposures) of a cultured human uterine adenocarcinoma cell specimen containing oxygen-doped (6,5) SWCNTs. Excitation was at the E_{22} transition **(a)** and the E_{11} transition **(b)**, under matched conditions. (C and D) Intensity profiles and peak-to-background contrast ratios along the yellow horizontal lines in the images.

3.6. Proposed quantum chemical model for the modified fluorescence emission from O-doped SWCNTs

We propose a photophysical model based on our quantum chemical calculation in which oxygen doping of a SWCNT at low doses creates sparse perturbed regions that have locally reduced band gaps.

3.6.1. Quantum chemical calculations

The PM3 semi-empirical method, implemented in HyperChem v7.5, was used by Dr. Sergei Bachilo to calculate energies of SWCNT fragments, a few nanometers in length and of several (*n,m*) structures, covalently bound to ozone or oxygen atoms. The nanotube fragments were terminated by hydrogen on their ends in these calculations. Geometries were optimized and the optimized energies were compared between systems containing the same set of atoms but different structures, such as the nanotube ozonide vs. the separated nanotube and ozone molecule. We term an adduct "*perpendicular*" if the line connecting the carbon atoms bound to oxygen is most nearly perpendicular to the nanotube axis; it is termed "*parallel*" if the line is most nearly parallel to the tube axis. We used quantum chemical modeling to predict the most stable product of O_3 reaction with SWCNTs and the resulting wave function perturbations over 2 to 3 nm long nanotube segments that represent the axial size of an exciton.[73,74] Such segments include ~200 carbon atoms, making them very challenging subjects for *ab initio* studies. We therefore applied a semi-empirical model (PM3), instead. In agreement with previous reports,[75-78] our computations point to formation of an ozonide adduct in which O_3 covalently bridges two adjacent carbon atoms (Fig. 3.15, left). Exothermicities vary from 20 to 40 kcal/mol, depending on SWCNT species and orientation of the O_3 addend.

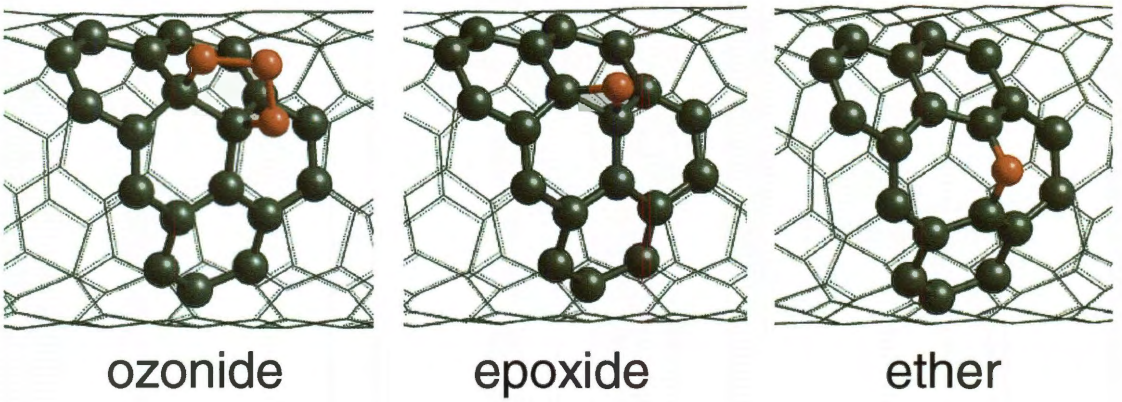

Figure 3.15 PM3-computed structures of the most stable ozonide (left), epoxide (center), and ether (right) adducts of a segment of (6,5) SWCNT.

The most stable adducts predicted for smaller diameter nanotubes tend to have O_3 groups oriented nearly parallel to the tube axis. In a process analogous to that experimentally observed in fullerene ozonides,[79-81] subsequent loss of O_2 from the ozonide leaves an epoxide with an oxygen atom bridging the same adjacent sp^3 carbon atoms (Fig. 3.15, center). However, our calculations show this epoxide adduct to be less stable (by more than 20 kcal/mol for a (6,5) nanotube) than an isomer in which the oxygen atom links two sp^2 carbon atoms nearly perpendicular to the nanotube axis through C-O-C ether bonds (Fig. 3.15, right). We propose that the light-induced step in our treatment is irreversible photoisomerization of the epoxide adduct into this much more stable ether structure. Similar results for the relative stabilities of SWCNT oxide isomers were recently reported by Johnson and co-workers from DFT *ab initio* calculations.[76]

3.6.2. Details of Computational Results

Ozonation: Ozone chemisorption was found to release 20 to 30 kcal/mol of energy (Fig. 3.16). The exothermicity is higher for small diameter nanotubes (such as (5,4)) and lower for larger diameter ones (such as (8,7)). The energy release for an

ozonide attached to carbons oriented more nearly perpendicular to the nanotube axes is smaller by a few kcal/mol.

Oxide 1. Conversion of the "*parallel*" ozonide into "*parallel*" epoxide plus ground state O_2 does not give a large energy release. Depending on nanotube diameter, the energy of the oxide plus oxygen molecule was a few kcal/mol higher or lower than the ozonide energy. Due to some uncertainty in the energy of molecular oxygen calculated using the PM3 method, the relative energies of the ozonide vs. the epoxide plus free oxygen may be in error by up to several kcal/mol. In the "*parallel*" attachment geometry, the only stable oxide isomer is found to be the epoxide.

Oxide 2. In the structure optimization for perpendicular attachment, an "*open*" oxide (ether structure) is found to be the only stable isomer. This ether is lower in energy than the "*parallel*" epoxide by ~25 kcal/mol. The stability difference is even larger for the smallest diameter nanotube considered, (5,4).

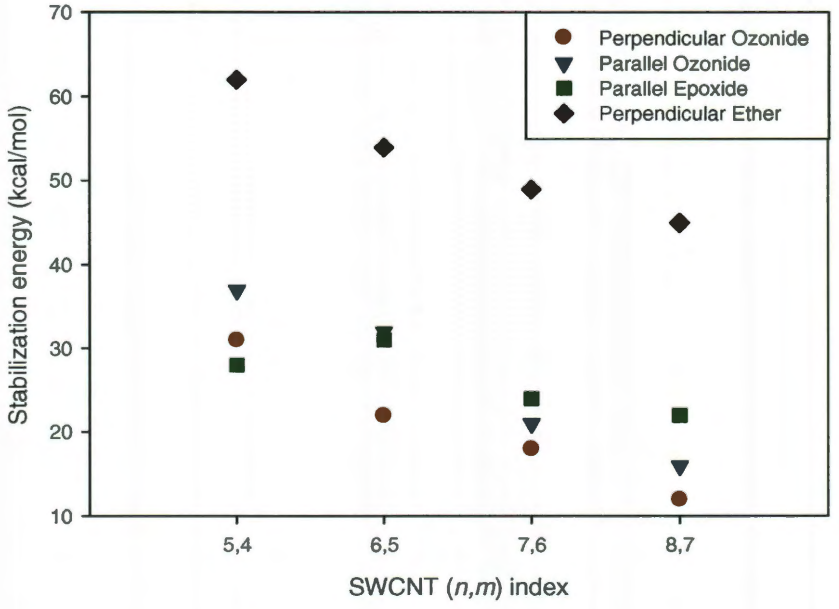

Figure 3.16 Stabilization energies of the different structures as compared to separated nanotube and molecular species.

The two oxide isomers cause quite different perturbations to the nanotube π-electron system. In the epoxide adduct, both carbon atoms bonded to the oxygen are converted to sp^3 hybridization, and five C-C bonds are significantly lengthened and angularly distorted. By contrast, in the ether adduct, sp^2 carbon hybridization is maintained, only one C-C bond lengthens (the broken one under the ether bridge), and angular distortions are smaller. The electronic and spectroscopic characters of the ether adduct should be much more similar to the pristine SWCNT than the epoxide adduct. An analogous result was demonstrated in earlier experimental studies of C_{60} and C_{70} treated with ozone.[79,80,82] After the initially formed fullerene ozonides lost O_2 to form oxides, those with ether bridges and sp^2 carbon hybridization could be distinguished from fullerene epoxides because they resembled the pristine parent fullerene in electronic absorption spectroscopy. Optical excitation of several C_{70} oxides converted them into other isomers through shifts of the oxygen atom on the cage surface.[80] We propose that the light-induced process observed in our treated SWCNTs is a related photoisomerization.

A comparison of computed wave functions for doped and pristine SWCNTs helps to interpret the observed optical properties. The highest occupied and lowest unoccupied molecular orbitals (HOMO and LUMO) for a perfect, infinitely long semiconducting SWCNT are both doubly degenerate. To model the optical perturbations caused by sparse doping, we considered short SWCNT segments having lengths comparable to exciton sizes (a few nanometers). For such segments, the degenerate HOMO and LUMO orbitals of chiral nanotubes showed a small end-effect splitting of order 0.01 meV (Fig. 3.18).

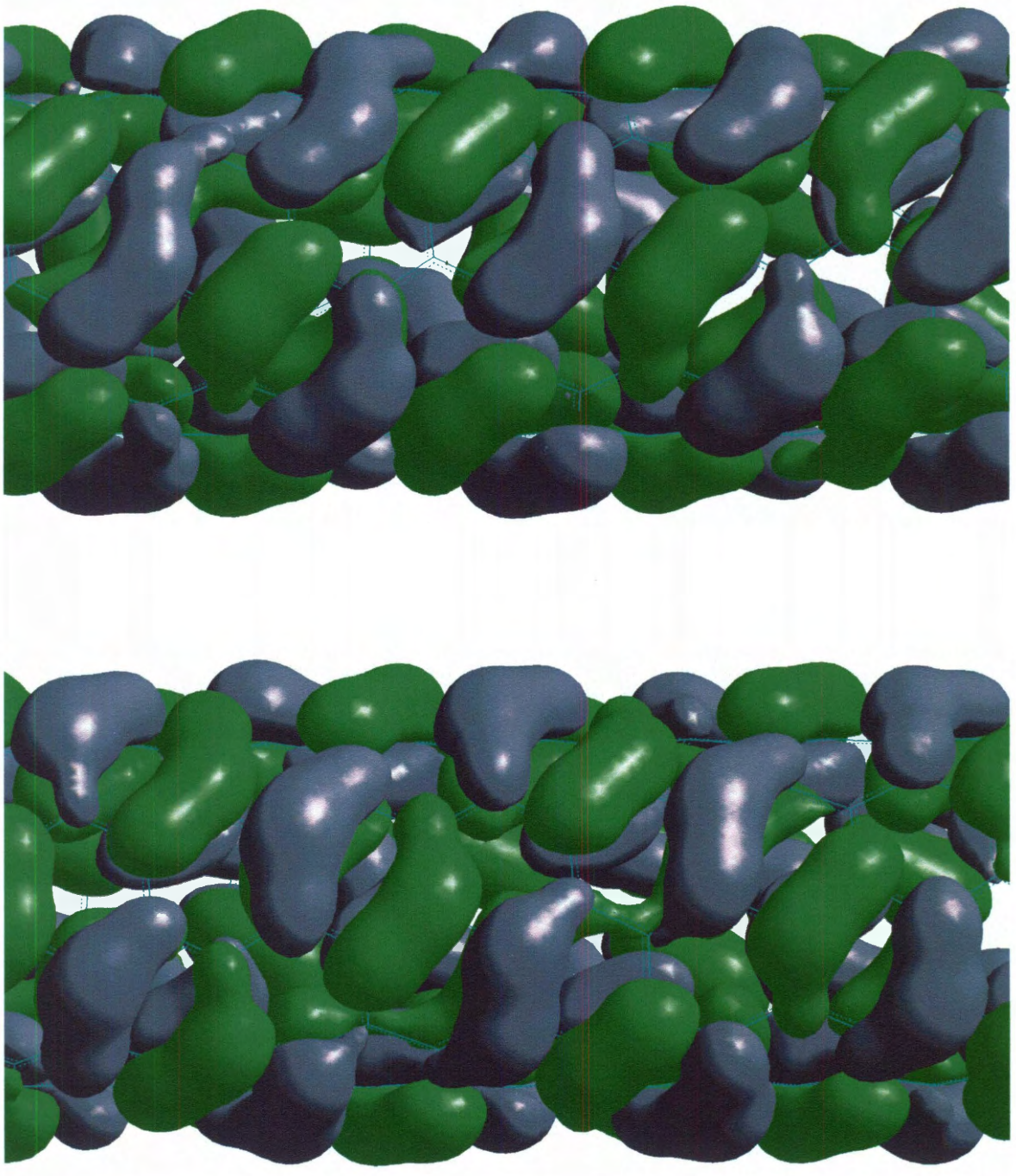

Figure 3.17 The highest occupied molecular orbitals (HOMO) for a (5,4) nanotube. In an infinite (very long) tube, these two orbitals have the same energy.

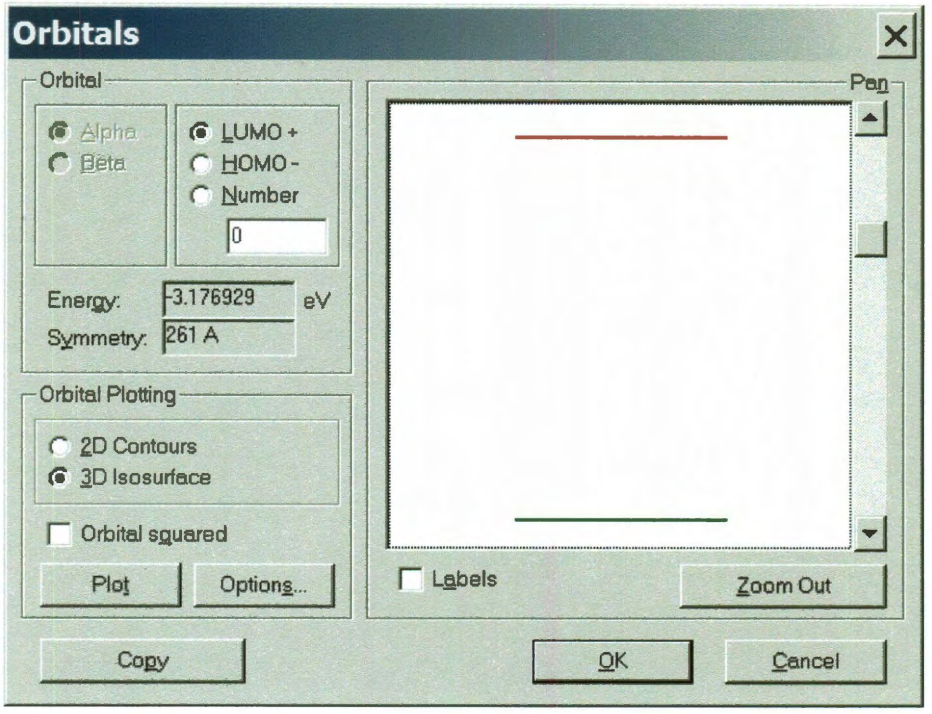

Figure 3.18 Typical energy diagram for HOMO and LUMO orbitals for a nanotube as represented by HyperChem software. A minor splitting (~ 0.01eV) is visible in both HOMO and LUMO due to a finite length of the asymmetric nanotube (5,4) used in the calculation.

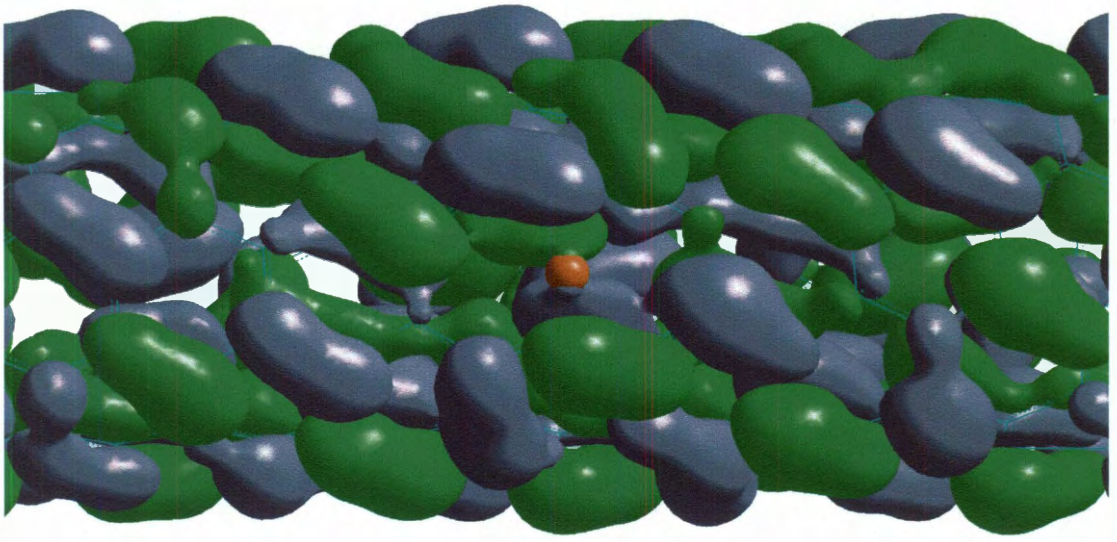

Figure 3.19 HOMO in the oxide (ether structure) of SWCNT. This is the lower orbital appearing after splitting of pristine nanotube HOMO. The shown position of oxygen is in an amplitude minimum of the orbital (between parts of different sign, near a node).

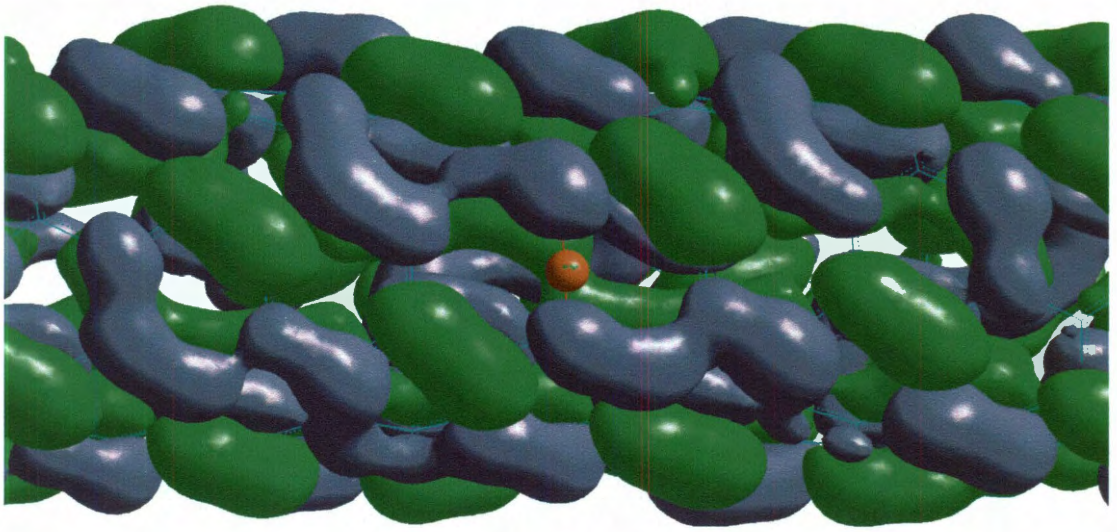

Figure 3.20 The second, higher-lying MO in the oxide (ether structure) of SWCNT. This orbital and the one in Fig.3.19 result from splitting of the pristine nanotube HOMO; their energies are shown in Fig. 3.21.

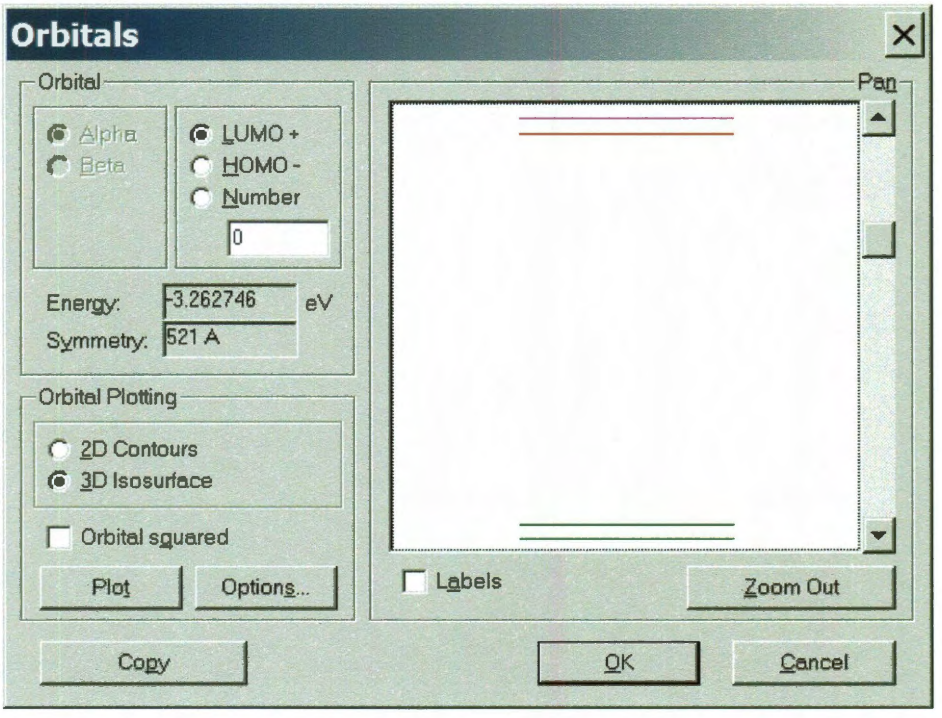

Figure 3.21 Typical orbital level diagram for a nanotube with an oxygen in the sidewall (ether structure). The splitting of both HOMO and LUMO are very pronounced, about 0.17 eV for a (5,4) nanotube. As seen here, the energy of the new HOMO can be lower than the energy of the orbital before splitting.

By contrast, an ether group oriented across the tube axis induces a far larger perturbation of 100 to 200 meV (Figs. 3.19-3.21). This splits the ground and excited state (termed as eh_{11} in Fig. 3.22) energies in the vicinity of the doping site to give four distinct levels. Dipole selection rules allow optical transitions between the upper excited state sub-level and the lower ground state sub-level, and also between the lower excited and upper ground sub-levels.

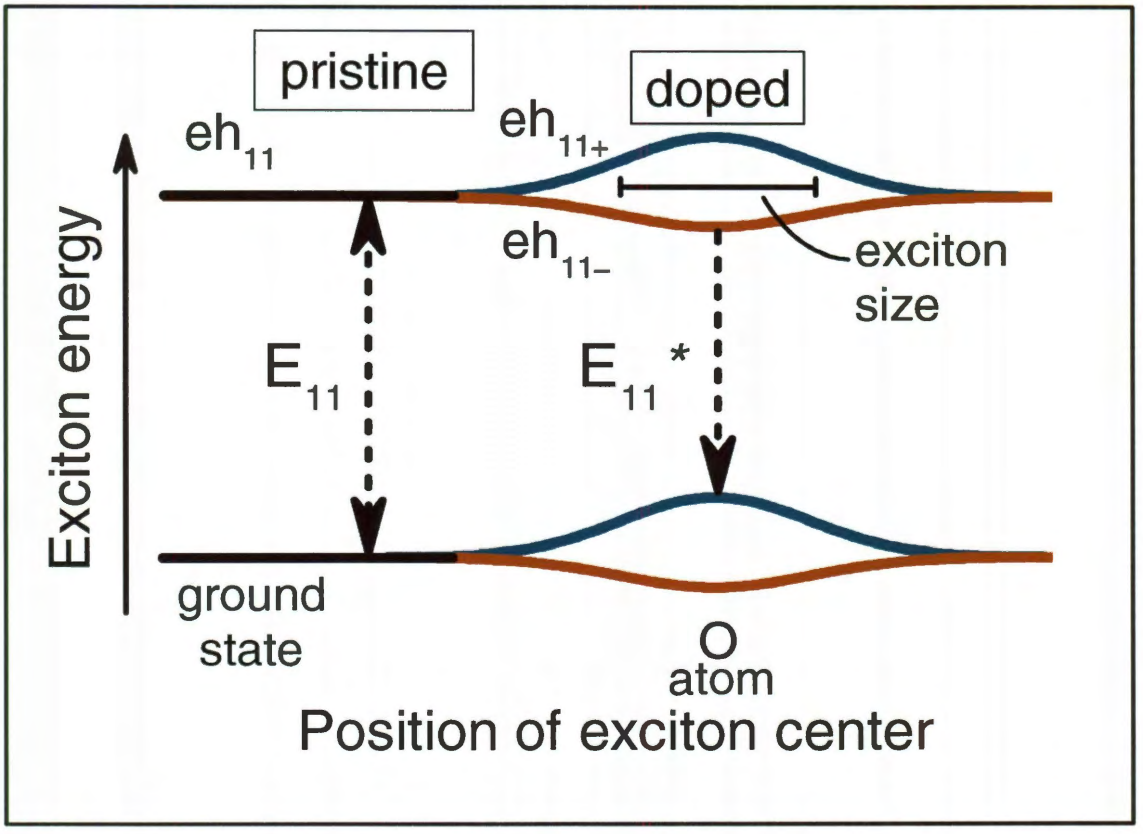

Figure 3.22 Qualitative energy level sketch showing oxygen-induced perturbations to the ground and lowest "bright" exciton states as a function of axial distance from the dopant atom. Dashed arrows indicate relevant allowed optical transitions.

The latter transition represents the red-shifted fluorescence (E_{11}*) observed from oxygen-doped SWCNTs. Our calculations also predict that the allowed transition dipoles

remain parallel to the nanotube axis, in agreement with polarization measurements (Fig. 3.11b). Absorption spectroscopy of our lightly doped nanotubes revealed neither of the distinctly shifted, allowed transitions between split levels because the strong electronic perturbation from oxygen doping is local and affects only a small fraction of the carbon atoms. However, we observed broadening of E_{11} and E_{22} absorptions, probably from a distribution of small exciton energy shifts extending to longer distances from doping sites. After light absorption, some of the excitons from undoped regions diffuse to doped centers, become trapped by the reduced potential, and emit in the red-shifted (E_{11}*) transition involving the lower LUMO and upper HOMO components. Trapping will be reversible if the well is not deep compared to the thermal energy, k_BT, and the ratio of E_{11}* to E_{11} emission intensities will decrease as temperature increases. Because the great majority of carbon atoms are remote from the doping sites, the overall absorption spectrum remains nearly unchanged and shows no appreciable component at the E_{11}* emission wavelength. However, excitons generated by light absorption in undoped regions are mobile, as in pristine nanotubes,[49,83,84] and may diffuse during their lifetimes to doped sites where they are stabilized by the locally reduced band gap. Radiative recombination of these trapped excitons gives the E_{11}* emission characteristic of the doped nanotubes. A single treated nanotube may show both E_{11} and E_{11}* emission because excitons can radiate while they are in pristine or doped locations. Higher doping levels increase the E_{11}* to E_{11} intensity ratio by raising the probability of trapping before emission. Assuming irreversible trapping and mean exciton ranges somewhat below pristine values, we estimate that SWCNTs with intensity ratios near one contain approximately one oxygen atom per few thousand carbon atoms.

3.6.3. Estimation of dopant density from temperature dependent fluorescence

Temperature-dependent fluorescence emission from bulk O-doped (6,5) and (8,3)-enriched SWCNT suspensions (Fig. 3.23, inset) was measured with a model NS1 NanoSpectralyzer using 785 and 659 nm excitation. The jacketed sample cell was temperature-controlled between 20 and 50 °C using a circulating water bath (Julabo MD Basis). A digital thermometer (Oven Industries, model 5C7-195) measured temperatures directly at the sample.

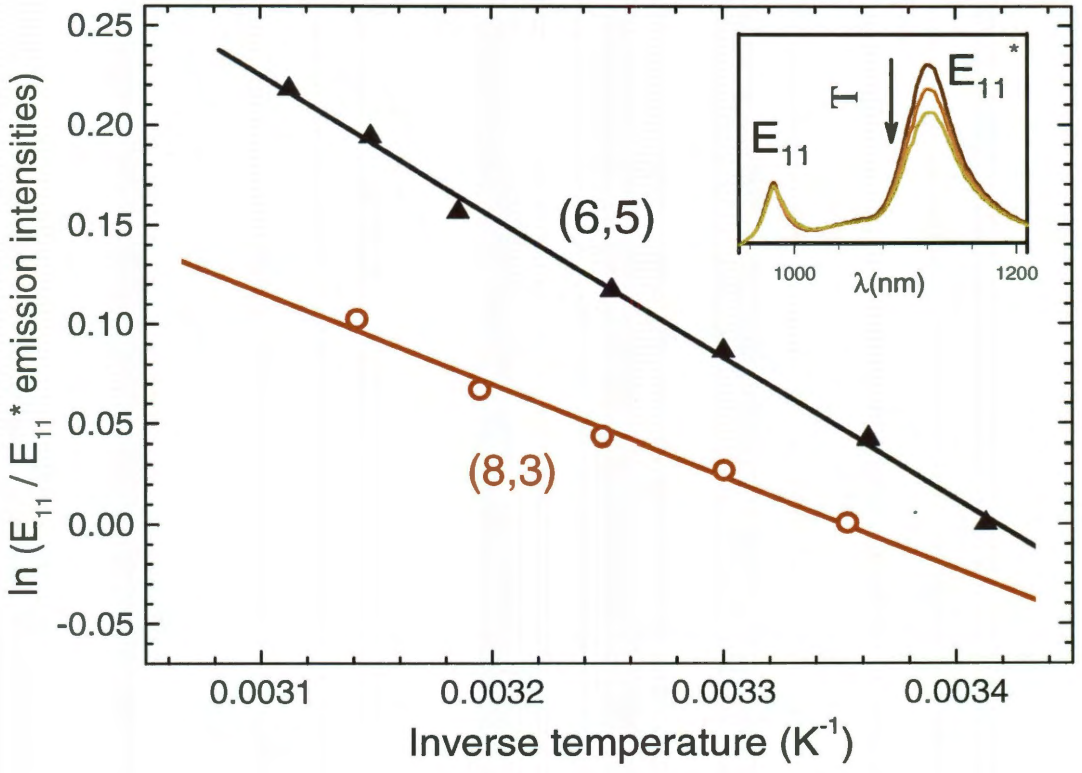

Figure 3.23 van't Hoff plot of relative ratios of unshifted to shifted integrated fluorescence from oxygen-doped bulk SWCNT samples. Well depths deduced from the slopes are 61 meV for (6,5) and 41 meV for (8,3). Inset shows spectral data for (6,5).

An estimation of dopant density was obtained by presuming thermal equilibrium of exciton populations between doped and pristine regions of nanotubes. Assuming equal radiative rates for excitons in the two regions, the ratio of pristine to shifted integrated emission intensities equals the ratio of equilibrated exciton populations in the two regions. This in turn is the Boltzmann factor $\exp(-\varepsilon/kT)$, where ε is the exciton well depth at the dopant site, times the ratio of available lengths along the nanotube that can accommodate static pristine and doped excitons. In the case of (6,5) SWCNTs, for which the well depth was measured as 61 meV (708 K), an emission intensity ratio of 1 at room temperature implies approximately 11 times more nanotube length available for pristine emission than for shifted emission. With an estimated static exciton size of 2.5 nm, this implies ~27.5 nm between dopant sites, or a dopant fraction of ~1 oxygen atom per 2400 carbon atoms (assuming 88 carbon atoms are available per nm of a tube). An equivalent estimate was obtained from the y-intercept of the experimental van't Hoff plot (2.45 for (6,5) and 1.57 for (8,3)), which represents the intensity ratio in the high temperature limit, and therefore the relative nanotube lengths corresponding to the two types of emission.

3.6.4. Further discussion of experimental results

A careful examination of the photoluminescence excitation-emission contour plot for O-doped (6,5)-enriched bulk sample revealed anther weak and broad, secondary shifted emission peak (defined by (*n,m*)** in Fig. 3.24), red-shifted by ~1100 cm^{-1} (~135 meV) from the main unshifted peak. This additional emission feature is more evident in heavily photoconverted O-doped smaller diameter species, such as (6,4), and becomes more pronounced and broader when further dose of ozone added to the doped sample. Most probably these secondary bands originate from the nanotubes with heavily O-

doped, chemically altered sections instead of sparsely doped well separated regions. However, we found less evidence of these secondary emission peaks while measuring near-IR emission spectra from individual O-doped SWCNTs. We suggest that further studies are required to elucidate the source and nature of these additional spectral features.

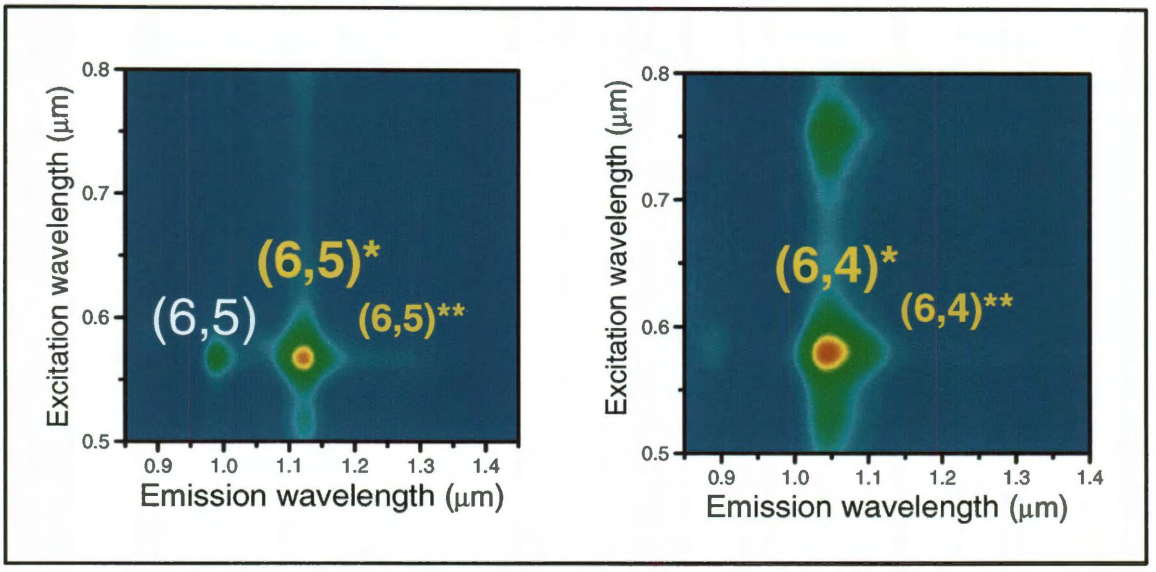

Figure 3.24 Photoluminescence excitation-emission contour plots for O-doped (6,5)- and (6,4)-enriched samples showing weak secondary shifted emission peaks labeled by (E_{11}^{**}).

3.7. Conclusions for chapter 3

Oxygen-doping of SWCNTs is a simple chemical treatment that spectrally separates near-IR emission from absorption bands. The altered electronic properties obtained through controlled O-doping suggest the potential for developing a family of SWCNT lasers that emit at the E_{11}^* transition after pumping by E_{11} or E_{22} direct excitation, by energy transfer, or by charge injection. One can also envision selective O-

doping of regions within individual SWCNTs to fabricate hybrid nanostructures with tailored optical and electronic properties. We believe that oxygen-doped SWCNTs hold substantial interest for basic research and applications development.

CHAPTER 4

CONCLUSIONS

4.1. Summary of current research work

As described in chapter 2, using a tailored NDGU approach we have significantly enhanced the performance of DGU for structurally sorting of mixed SWCNT samples. Experimental conditions were optimized with the aid of a device that quickly measured fluorescence maps to reveal the spatial locations and profiles of (*n*,*m*) fractions inside undisturbed centrifuge tubes. Although previous DGU studies have focused on sorting raw SWCNT samples that contain small numbers of species, our approach is successful with highly polydisperse samples grown by the HiPco method. We can sort HiPco samples to obtain fractions highly enriched in at least ten different (*n*,*m*) species. In addition, the combined use of co-surfactants and nonlinear gradients permits the enantiomeric separation of seven different (*n*,*m*) species. All of these separations have been achieved with only a single step of DGU processing.

Using sorted samples produced in this way, we discovered and characterized a new class of chemically modified SWCNTs. For the first time, chemical processing has created doped semiconducting nanotubes with well-defined modified optical properties. As demonstrated for ten different SWCNT (*n*,*m*) structures,[59] chemically altered nanotubes display slightly lower optical band gap energies with correspondingly longer photoluminescence wavelengths. The transformation is achieved using very limited oxidation of SWCNTs with ozone followed by a photochemical conversion step. Treated samples show distinct, structure-specific near-infrared fluorescence at wavelengths 10 to 15% longer than the pristine semiconducting SWCNTs. Our quantum mechanical model

suggests that dopant sites harvest light energy absorbed in undoped nanotube regions by trapping mobile excitons. The O-doped SWCNTs are much easier to detect and image than pristine SWCNTs because they give stronger near-IR emission and do not absorb at the shifted emission wavelength. Our novel modification of SWCNT properties could lead to new optical and electronic applications, as it provides a way to change band gaps in whole nanotubes or in selected sections.

4.2. Suggestions for future work

Future research should explore some of the exciting research opportunities regarding the preparation, properties, and applications of O-doped SWCNTs. As described below, these include more efficient sample preparation, uniform doping of wide range of (*n,m*) species, exploring additional photophysical properties, and building advanced optical setups for biological applications.

4.2.1. Optimization of sample preparation

The oxygen doping of SWCNTs is performed on bulk samples highly enriched in individual semiconducting (*n,m*) species. However, in most cases, O_3 oxidation of bulk (*n,m*) sorted samples leads to inhomogeneous O-doping extents of SWCNTs within the sample. We plan to develop a modified NDGU protocol which will efficiently sort treated nanotubes according to their extent of doping. This may be achieved by customizing density gradients or by altering nanotube coating surfactants used for the NDGU runs.

4.2.2. Further photophysical study of O-doped SWCNTs

It is important to improve our understanding of O-doped SWCNT photophysical properties via fluorescence (single-tube and bulk), absorption, and Raman spectroscopy.

Additionally, a comparison between the bulk fluorescence efficiencies of pristine and O-doped SWCNTs is a point of research interest. It is necessary to measure the absolute fluorimetric brightness of individual O-doped tubes at their red-shifted emission compared to pristine species using the protocol developed by Tsyboulski and coworkers.[85]

The lineshapes and spectral widths of red shifted fluorescence emission of O-doped SWCNTs differ significantly from those of pristine tubes. It is of interest to measure whether the emission widths are homogeneous or inhomogeneous and how they vary with the dopant concentrations. An example of photophysical heterogeneity in the doped samples is evident in Fig. 3.11, where single-tube fluorescence from O-doped tubes shows varying extents of spectral conversion. Furthermore, single-tube fluorescence microscopy show that doped tubes with the same (*n*,*m*) identity have emission with somewhat different peak wavelengths. We need to explore the treatment factors that influence this spectral variation in doped species.

4.2.3. Biomedical applications

In chapter 3, we demonstrated enhanced detectivity of nanotubes by near-IR fluorescence microscopy of cultured human uterine adenocarcinoma cells incubated in growth medium containing O-doped SWCNTs (Fig. 3.14). Here, O-doped tubes were excited at their characteristic E_{11} transition. We achieved a factor of 20 improvement in image contrast, with the ability to clearly image individual nanotubes in cells in 100 ms. To further enhance the detection of these O-SWCNT in biological systems, It is worthwhile to develop a refined optical setup using direct E_{11} excitation of several doped species. This will requires better near-IR lasers and long-pass optical filters. Besides,

better imaging capability allows us to investigate very sensitively the uptake of O-doped SWCNTs by cultured cells and correlate uptake with cytotoxicity. Another important near-term application will be to use O-doped nanotubes to tag and sensitively track cancer stem cells in vitro. This project can be pursued in collaboration with Texas Medical Center researchers.

REFERENCES

1. Iijima, S. Helical Microtubules of Graphitic Carbon. *Nature* **1991,** *354*, 56-58.

2. Baughman, R. H.; Zakhidov, A. A.; de Heer, W. A. Carbon Nanotubes - the Route Toward Applications. *Science* **2002,** *297*, 787-792.

3. Reich, S.; Thomsen, C.; Maultzsch, J. *Carbon Nanotubes: Basic Concepts and Physical Properties;* Wiley-VCH: Weinheim, 2004.

4. Hamada, N.; Sawada, S.; Oshiyama, A. New One-Dimensional Conductors: Graphitic Microtubules. *Phys. Rev. Lett.* **1992,** *68*, 1579-1581.

5. Saito, R.; Dresselhaus, G.; Dresselhaus, M. S. *Physical Properties of Carbon Nanotubes;* Imperial College Press: London, 1998.

6. Terrones, M.; Hsu, W. K.; Kroto, H. W.; Walton, D. R. M. Nanotubes: A Revolution in Materials Science and Electronics. *Fullerenes and Related Structures* **1999,** *199*, 189-234.

7. Weisman, R. B. Fluorimetric Characterization of Single-Walled Carbon Nanotubes. *Anal. Bioanal. Chem.* **2010,** *396*, 1015-1023.

8. Odom, T. W.; Huang, J. L.; Kim, P.; Lieber, C. M. Atomic Structure and Electronic Properties of Single-Walled Carbon Nanotubes. *Nature* **1998,** *391*, 62-64.

9. Odom, T. W.; Huang, J.-L.; Kim, P.; Lieber, C. M. Structure and Electronic Properties of Carbon Nanotubes. *J. Phys. Chem. B* **2000,** *104*, 2794-2809.

10. Weisman, R. B.; Bachilo, S. M. Dependence of Optical Transition Energies on Structure for Single-Walled Carbon Nanotubes in Aqueous Suspension: an Empirical Kataura Plot. *Nano Lett.* **2003,** *3*, 1235-1238.

11. O'Connell, M. J.; Bachilo, S. M.; Huffman, C. B.; Moore, V.; Strano, M. S.; Haroz, E.; Rialon, K.; Boul, P. J.; Noon, W. H.; Kittrell, C. et al. Band-Gap Fluorescence From Individual Single-Walled Carbon Nanotubes. *Science* **2002,** *297*, 593-596.

12. Nikolaev, P.; Bronikowski, M. J.; Bradley, R. K.; Rohmund, F.; Colbert, D. T.; Smith, K. A.; Smalley, R. E. Gas-Phase Catalytic Growth of Single-Walled Carbon Nanotubes From Carbon Monoxide. *Chem. Phys. Lett.* **1999,** *313*, 91-97.

13. Bachilo, S. M.; Strano, M. S.; Kittrell, C.; Hauge, R. H.; Smalley, R. E.; Weisman, R. B. Structure-Assigned Optical Spectra of Single-Walled Carbon Nanotubes. *Science* **2002,** *298*, 2361-2366.

14. Javey, A.; Guo, J.; Wang, Q.; Lundstrom, M.; Dai, H. J. Ballistic Carbon Nanotube Field-Effect Transistors. *Nature* **2003,** *424*, 654-657.

15. Barone, P. W.; Baik, S.; Heller, D. A.; Strano, M. S. Near-Infrared Optical Sensors Based on Single-Walled Carbon Nanotubes. *Nat. Mater.* **2005,** *4*, 86-92.

16. Wu, Z. C.; Chen, Z. H.; Du, X.; Logan, J. M.; Sippel, J.; Nikolou, M.; Kamaras, K.; Reynolds, J. R.; Tanner, D. B.; Hebard, A. F. et al. Transparent, Conductive Carbon Nanotube Films. *Science* **2004,** *305*, 1273-1276.

17. Green, A. A.; Hersam, M. C. Colored Semitransparent Conductive Coatings Consisting of Monodisperse Metallic Single-Walled Carbon Nanotubes. *Nano Lett.* **2008,** *8*, 1417-1422.

18. Krupke, R.; Hennrich, F.; von Lohneysen, H.; Kappes, M. M. Separation of Metallic From Semiconducting Single-Walled Carbon Nanotubes. *Science* **2003,** *301*, 344-347.

19. Zheng, M.; Jagota, A.; Strano, M. S.; Santos, A. P.; Barone, P. W.; Chou, S. G.; Diner, B. A.; Dresselhaus, M. S.; McIean, R. S.; Onoa, G. B. et al. Structure-Based Carbon Nanotube Sorting by Sequence-Dependent DNA Assembly. *Science* **2003,** *302*, 1545-1548.

20. Zheng, M.; Semke, E. D. Enrichment of Single Chirality Carbon Nanotubes. *J. Am. Chem. Soc.* **2007,** *129*, 6084-6085.

21. Tu, X.; Manohar, A.; Jagota, A.; Zheng, M. DNA Sequence Motifs for Structure-Specific Recognition and Separation of Carbon Nanotubes. *Nature* **2009,** *460*, 250-253.

22. Davies, I.; Graham, J. M. The Use of Self-Generated Gradients of Iodixanol for the Purification of Macromolecules and Macromolecular Complexes. *FASEB J* **1997,** *11*, A908.

23. Graham, J. M. *Biological Centrifugation;* BIOS Scientific, UK: 2001.

24. Heller, D. A.; Mayrhofer, R. M.; Baik, S.; Grinkova, Y. V.; Usrey, M. L.; Strano, M. S. Concomitant Length and Diameter Separation of Single-Walled Carbon Nanotubes. *J. Am. Chem. Soc.* **2004,** *126*, 14567-14573.

25. Doorn, S. K.; Fields, R. E.; Hu, H.; Hamon, M. A.; Haddon, R. C.; Selegue, J. P.; Majidi, V. High Resolution Capillary Electrophoresis of Carbon Nanotubes. *J. Am. Chem. Soc.* **2002,** *124*, 3169-3174.

26. Doorn, S. K.; Strano, M. S.; O'Connell, M. J.; Haroz, E. H.; Rialon, K. L.; Hauge, R. H.; Smalley, R. E. Capillary Electrophoresis Separations of Bundled and Individual Carbon Nanotubes. *J. Phys. Chem. B* **2003,** *107*, 6063-6069.

27. Krupke, R.; Hennrich, F.; Kappes, M. M.; L+¦hneysen, H. V. Surface Conductance Induced Dielectrophoresis of Semiconducting Single-Walled Carbon Nanotubes. *Nano Lett.* **2004,** *4*, 1395-1399.

28. Hennrich, F.; Krupke, R.; Kappes, M. M.; Lo¦êhneysen, H. V. Frequency Dependence of the Dielectrophoretic Separation of Single-Walled Carbon Nanotubes. *J. Nanosci. Nanotechnol.* **2005,** *5*, 1166-1171.

29. Zheng, M.; Jagota, A.; Semke, E. D.; Diner, B. A.; McClean, R. S.; Lustig, S. R.; Richardson, R. E.; Tassi, N. G. DNA-Assisted Dispersion and Separation of Carbon Nanotubes. *Nat. Mater.* **2003,** *2*, 338-342.

30. Strano, M. S.; Zheng, M.; Jagota, A.; Onoa, G. B.; Heller, D. A.; Barone, P. W.; Usrey, M. L. Understanding the Nature of the DNA-Assisted Separation of Single-Walled Carbon Nanotubes Using Fluorescence and Raman Spectroscopy. *Nano Lett.* **2004,** *4*, 543-550.

31. Tanaka, T.; Urabe, Y.; Nishide, D.; Kataura, H. Continuous Separation of Metallic and Semiconducting Carbon Nanotubes Using Agarose Gel. *Applied Physics Express* **2009,** *2*.

32. Moshammer, K.; Hennrich, F.; Kappes, M. M. Selective Suspension in Aqueous Sodium Dodecyl Sulfate According to Electronic Structure Type Allows Simple Separation of Metallic From Semiconducting Single-Walled Carbon Nanotubes. *Nano Research* **2009,** *2*, 599-606.

33. Liu, H.; Tanaka, T.; Feng, Y.; Kataura, H. Diameter-Selective Desorption of Semiconducting Single-Wall Carbon Nanotubes From Agarose Gel. *Physica Status Solidi (B) Basic Research* **2010,** *247*, 2649-2652.

34. Liu, H.; Nishide, D.; Tanaka, T.; Kataura, H. Large-Scale Single-Chirality Separation of Single-Wall Carbon Nanotubes by Simple Gel Chromatography. *Nature Communications* **2011,** *2*.

35. Arnold, M. S.; Stupp, S. I.; Hersam, M. C. Enrichment of Single-Walled Carbon Nanotubes by Diameter in Density Gradients. *Nano Lett.* **2005,** *5*, 713-718.

36. Arnold, M. S.; Green, A. A.; Hulvat, J. F.; Stupp, S. I.; Hersam, M. C. Sorting Carbon Nanotubes by Electronic Structure Using Density Differentiation. *Nature Nanotech.* **2006,** *1*, 60-65.

37. Kitiyanan, B.; Alvarez, W. E.; Harwell, J. H.; Resasco, D. E. Controlled Production of Single-Wall Carbon Nanotubes by Catalytic Decomposition of CO on Bimetallic CoMo Catalysts. *Chem. Phys. Lett.* **2000,** *317*, 497-503.

38. Ciuparu, D.; Chen, Y.; Lim, S.; Haller, G. L.; Pfefferle, L. D. Uniform-Diameter Single-Walled Carbon Nanotubes Catalytically Grown in Cobalt-Incorporated MCM-41. *J. Phys. Chem. B* **2004,** *108*, 503-507.

39. Bachilo, S. M.; Balzano, L.; Herrera, J. E.; Pompeo, F.; Resasco, D. E.; Weisman, R. B. Narrow (n,m)-Distribution of Single-Walled Carbon Nanotubes Grown Using a Solid Supported Catalyst. *J. Am. Chem. Soc.* **2003,** *125*, 11186-11187.

40. Kim, W.-J.; Nair, N.; Lee, C. Y.; Strano, M. S. Covalent Functionalization of Single-Walled Carbon Nanotubes Alters Their Densities Allowing Electronic and Other Types of Separation. *J. Phys. Chem. C* **2008,** *112*, 7326-7331.

41. Backes, C.; Hauke, F.; Schmidt, C. D.; Hirsch, A. Fractioning HiPco and CoMoCAT SWCNTs Via Density Gradient Ultracentrifugation by the Aid of a Novel Perylene Bisimide Derivative Surfactant. *Chem. Commun.* **2009,** *2009*, 2643-2645.

42. Kato, Y.; Niidome, Y.; Nakashima, N. Efficient Separation of (6,5) Single-Walled Carbon Nanotubes Using a "Nanometal Sinker". *Angew. Chem. , Int. Ed. Engl.* **2009,** *48*, 5435-5438.

43. Ghosh, S.; Bachilo, S. M.; Weisman, R. B. Advanced Sorting of Single-Walled Carbon Nanotubes by Nonlinear Density-Gradient Ultracentrifugation. *Nature Nanotech.* **2010,** *5*, 443-450.

44. Ford, T.; Graham, J.; Rickwood, D. Iodixanol—a Nonionic Isosmotic Centrifugation Medium for the Formation of Self-Generated Gradients. *Analitycal Biochemistry* **1994,** 360-366.

45. Arnold, M. S.; Suntivich, J.; Stupp, S. I.; Hersam, M. C. Hydrodynamic Characterization of Surfactant Encapsulated Carbon Nanotubes Using an Analytical Ultracentrifuge. *ACS Nano* **2008,** *2*, 2291-2300.

46. Rocha, J.-D. R.; Bachilo, S. M.; Ghosh, S.; Arepalli, S.; Weisman, R. B. Efficient Spectroflouorimetric Analysis of Single-Salled Carbon Nanotube Samples. *Anal. Chem.* **2010,** *to be submitted.*

47. Nair, N.; Kim, W. J.; Braatz, R. D.; Strano, M. S. Dynamics of Surfactant-Suspended Single-Walled Carbon Nanotubes in a Centrifugal Field. *Langmuir* **2008,** *24*, 1790-1795.

48. Green, A. A.; Duch, M. C.; Hersam, M. C. Isolation of Single-Walled Carbon Nanotube Enantiomers by Density Differentiation. *Nano Research* **2009,** *2*, 69-77.

49. Cognet, L.; Tsyboulski, D.; Rocha, J.-D. R.; Doyle, C. D.; Tour, J. M.; Weisman, R. B. Stepwise Quenching of Exciton Fluorescence in Carbon Nanotubes by Single-Molecule Reactions. *Science* **2007,** *316*, 1465-1468.

50. Hebling, C. M.; Thompson, L. E.; Eckenroad, K. W.; Manley, G. A.; Fry, R. A.; Mueller, K. T.; Strein, T. G.; Rovnyak, D. Sodium Cholate Aggregation and Chiral Recognition of the Probe Molecule (R,S)-1,1'-Binaphthyl-2,2'-Diylhydrogenphosphate (BNDHP) Observed by ^{1}H and ^{31}P Spectroscopy. *Langmuir* **2008,** *24*, 13866-13874.

51. Peng, X.; Komatsu, N.; Bhattacharya, S.; Shimawaki, T.; Aonuma, S.; Kimura, T.; Osuka, A. Optically Active Singlewalled Carbon Nanotubes. *Nature Nanotech.* **2007,** *2*, 361-365.

52. Haroz, E. H.; Bachilo, S. M.; Weisman, B.; Doorn, S. K. Curvature Effects on the E33 and E44 Exciton Transitions in Semiconducting Single-Walled Carbon Nanotubes. *Phys. Rev. B* **2008,** *77*, 125405-1-125405-9.

53. Samsonidze, G. G.; Gruneis, A.; Saito, R.; Jorio, A.; Souza Filho, A. G.; Dresselhaus, G.; Dresselhaus, M. S. Interband Optical Transitions in Left- and Right-Handed Single-Wall Carbon Nanotubes. *Phys. Rev. B* **2004,** *69*, 205402-1-205402-11.

54. Peng, X.; Komatsu, N.; Kimura, T.; Osuka, A. Improved Optical Enrichment of SWNTs Through Extraction With Chiral Nanotweezers of 2,6-Pyridylene-Bridged Diporphyrins. *J. Am. Chem. Soc.* **2007,** *129*, 15947-15953.

55. Peng, X.; Komatsu, N.; Kimura, T.; Osuka, A. Simultaneous Enrichments of Optical Purity and (*n,m*) Abundance of SWNTs Through Extraction With 3,6-Carbazolylene-Bridged Chiral Diporphyrin Nanotweezers. *ACS Nano* **2008,** *2*, 2045-2050.

56. Banerjee, S.; Hemraj-Benny, T.; Wong, S. S. Covalent Surface Chemistry of Single-Walled Carbon Nanotubes. *Adv. Mater.* **2005,** *17*, 17-29.

57. Hirsch, A.; Vostrowsky, O. Functionalization of Carbon Nanotubes. *Topics in Current Chemistry* **2005,** *245*, 193-237.

58. Qin, S.; Qin, D.; Ford, W. T.; Herrera, J. E.; Resasco, D. E.; Bachilo, S. M.; Weisman, R. B. Solubilization and Purification of Single-Wall Carbon Nanotubes in Water by in Situ Radical Polymerization of Sodium 4-Styrenesulfonate. *Macromolecules* **2004,** *37*, 3965-3967.

59. Ghosh, S.; Bachilo, S. M.; Simonette, R. A.; Beckingham, K. M.; Weisman, R. B. Oxygen Doping Modifies Near-Infrared Band Gaps in Fluorescent Single-Walled Carbon Nanotubes. *Science* **2010,** *330*, 1656-1659.

60. Kiowski, O.; Arnold, K.; Lebedkin, S.; Hennrich, F.; Kappes, M. M. Direct Observation of Deep Excitonic States in the Photoluminescence Spectra of Single-Walled Carbon Nanotubes. *Phys. Rev. Lett.* **2007,** *99*, 1-4.

61. Murakami, Y.; Lu, B.; Kazaoui, S.; Minami, N.; Okubo, T.; Maruyama, S. Photoluminescence Sidebands of Carbon Nanotubes Below the Bright Singlet Excitonic Levels. *Phys. Rev. B* **2009,** *79*, 195407-1-195407-5.

62. Torrens, O. N.; Zheng, M.; Kikkawa, J. M. Energy of K-Momentum Dark Excitons in Carbon Nanotubes by Optical Spectroscopy. *Phys. Rev. Lett.* **2008,** *101*, 157401-1-157401-4.

63. Mawhinney, D. B.; Naumenko, V.; Kuznetsova, A.; Yates, J. J. T.; Liu, J.; Smalley, R. E. Infrared Spectral Evidence for the Eching of Carbon Nanotubes: Ozone Oxidation at 298 K. *J. Am. Chem. Soc.* **2000,** *122*, 2383-2384.

64. Banerjee, S.; Wong, S. S. Rational Sidewall Functionalization and Purification of Single-Walled Carbon Nanotubes by Solution-Phase Ozonolysis. *J. Phys. Chem. B* **2002,** *106*, 12144-12151.

65. Cai, L. T.; Bahr, J. L.; Yao, Y. X.; Tour, J. M. Ozonation of Single-Walled Carbon Nanotubes and Their Assemblies on Rigid Self-Assembled Monolayers. *Chem. Mater.* **2002,** *14*, 4235-4241.

66. Chen, Z.; Ziegler, K. J.; Shaver, J.; Hauge, R. H.; Smalley, R. E. Cutting of Single-Walled Carbon Nanotubes by Ozonolysis. *J. Phys. Chem. B* **2006,** *110*, 11624-11627.

67. Ogrin, D.; Chattopadhyay, J.; Sadana, A. K.; Billups, W. E.; Barron, A. R. Epoxidation and Deoxygenation of Single-Walled Carbon Nanotubes: Quantification of Epoxide Defects. *J. Am. Chem. Soc.* **2006,** *128*, 11322-11323.

68. Simmons, J. M.; Nichols, B. M.; Baker, S. E.; Marcus, M. S.; Castellini, O. M.; Lee, C. S.; Hamers, R. J.; Eriksson, M. A. Effect of Ozone Oxidation on Single-Walled Carbon Nanotubes. *J. Phys. Chem. B* **2006,** *110*, 7113-7118.

69. Li, M.; Boggs, M.; Beebe, T. P.; Huang, C. P. Oxidation of Single-Walled Carbon Nanotubes in Dilute Aqueous Solutions by Ozone As Affected by Ultrasound. *Carbon* **2008,** *46*, 466-475.

70. Tsvaygboym, K. Ph.D. Thesis Rice University, 2007.

71. Harutyunyan, H.; Gokus, T.; Green, A. A.; Hersam, M. C.; Allegrini, M.; Hartschuh, A. Defect-Induced Photoluminescence From Dark Excitonic States in Individual Single-Walled Carbon Nanotubes. *Nano Lett.* **2009,** *9*, 2010-2014.

72. Tsyboulski, D. A.; Bachilo, S. M.; Weisman, R. B. Versatile Visualization of Individual Single-Walled Carbon Nanotubes With Near-Infrared Fluorescence Microscopy. *Nano Lett.* **2005,** *5*, 975-979.

73. Perebeinos, V.; Tersoff, J.; Avouris, Ph. Scaling of Excitons in Carbon Nanotubes. *Phys. Rev. Lett.* **2004,** *92*, 257402-1-257402-4.

74. Lüer, L.; Hoseinkhani, S.; Polli, D.; Crochet, J.; Hertel, T.; Lanzani, G. Size and Mobility of Excitons in (6,5) Carbon Nanotubes. *Nature Physics* **2009,** *5*, 54-58.

75. Picozzi, S.; Santucci, S.; Lozzi, L.; Valentini, L.; Delley, B. Ozone Adsorption on Carbon Nanotubes: The Role of Stone-Wales Defects. *J. Chem. Phys.* **2004,** *120*, 7147-7152.

76. Yim, W. L.; Karl Johnson, J. Ozone Oxidation of Single Walled Carbon Nanotubes From Density Functional Theory. *J. Phys. Chem. C* **2009,** *113*, 17636-17642.

77. Lu, X.; Zhang, L.; Xu, X.; Wang, N.; Zhang, Q. Can the Sidewalls of Single-Wall Carbon Nanotubes Be Ozonized? *J. Phys. Chem. B* **2002,** *106*, 2136-2139.

78. Akdim, B.; Kar, T.; Duan, X.; Pachter, R. Density Functional Theory Calculations of Ozone Adsorption on Sidewall Single-Wall Carbon Nanotubes With Stone-Wales Defects. *Chem. Phys. Lett.* **2007,** *445*, 281-287.

79. Heymann, D.; Bachilo, S. M.; Weisman, R. B.; Cataldo, F.; Fokkens, R. H.; Nibbering, N. M. M.; Vis, R. D.; Chibante, L. P. F. $C_{60}O_3$, a Fullerene Ozonide: Synthesis and Dissociation to $C_{60}O$ and O_2. *J. Am. Chem. Soc.* **2000,** *122*, 11473-11479.

80. Heymann, D.; Bachilo, S. M.; Weisman, R. B. Ozonides, Epoxides, and Oxidoannulenes of C_{70}. *J. Am. Chem. Soc.* **2002,** *124*, 6317-6323.

81. Heymann, D.; Weisman, R. B. Fullerene Oxides and Ozonides. *Comptes Rendu Chimie* **2006,** *9*, 1107-1116.

82. Weisman, R. B.; Heymann, D.; Bachilo, S. M. Synthesis and Characterization of the "Missing" Oxide of C_{60}: [5,6]-Open $C_{60}O$. *J. Am. Chem. Soc.* **2001,** *123*, 9720-9721.

83. Siitonen, A. J.; Tsyboulski, D. A.; Bachilo, S. M.; Weisman, R. B. Surfactant-Dependent Exciton Mobility in Single-Walled Carbon Nanotubes Studied by Single-Molecule Reactions. *Nano Lett.* **2010,** *10*, 1595-1599.

84. Siitonen, A. J.; Tsyboulski, D. A.; Bachilo, S. M.; Weisman, R. B. Dependence of Exciton Mobility on Structure in Single-Walled Carbon Nanotubes. *J. Phys. Chem. Lett.* **2010,** *1*, 2189-2192.

85. Tsyboulski, D.; Rocha, J.-D. R.; Bachilo, S. M.; Cognet, L.; Weisman, R. B. Structure-Dependent Fluorescence Efficiencies of Individual Single-Walled Carbon Nanotubes. *Nano Lett.* **2007,** *7*, 3080-3085.